



DIPLOMA THESIS

Extended Chip Card Resonance Frequency Measurement Method

Mladen Pesic, BSc
Matr. Nr. 0828021

supervised by

Associate Prof. Dipl.-Ing. Dr.techn. Holger Arthaber
and
Univ.Ass. Dipl.-Ing. Bernhard Pichler, BSc

Institute of Electrodynamics, Microwave and Circuit Engineering
Technische Universität Wien

Vienna, January 2018

Abstract

In recent years, RFID technology and its applications have substantially increased in importance, mainly due to expanding use of contactless chip cards in payment and government identification sectors. These cards rely on the principles of resonant circuits and inductive coupling, making resonance frequency an important parameter for their development and verification. The currently established method for measuring resonance frequency is performed on a vector network analyzer and it features certain disadvantages with respect to accuracy and objectivity of the measurement.

A new method for measuring resonance frequency is presented in this thesis. This method gives a more accurate definition of resonance frequency, removes any subjectivity, and makes the measurement integrable into standardized test setups. The method utilizes signal processing and system modeling to determine the maximum active power over a range of frequencies in the chip card. This is achieved by applying a transfer function obtained from the model and by using a so-called chirp signal as input to the system. The determined maximum of active power is mapped to the corresponding frequency in the chirp signal, which is defined as the new resonance frequency. Feasibility of the new method is confirmed by simulations, as well as by comparing measurement results with the currently established method. The results show that the new method offers significant advantages over the vector network analyzer method.

Kurzfassung

In den letzten Jahren haben die RFID Technologie und ihre Anwendungen wesentlich an Bedeutung gewonnen. Der Hauptgrund dafür ist die verbreitete Verwendung von kontaktlosen Chipkarten im Zahlungsverkehr und behördlich ausgestellten Ausweisen. Diese Karten beruhen auf den Prinzipien des Resonanzschwingkreises sowie der induktiven Kopplung. Dadurch stellt die Resonanzfrequenz einen der wichtigsten Parameter für die Entwicklung und Verifikation von kontaktlosen Chipkarten dar. Die derzeit etablierte Methode der Resonanzfrequenzmessung wird mit einem Netzwerkanalysator durchgeführt, was gewisse Nachteile im Sinne der Genauigkeit und Objektivität der Messung mit sich bringt.

Eine neue Methode zur Resonanzfrequenzmessung wird in dieser Arbeit vorgestellt. Diese Methode gibt eine genauere Definition der Resonanzfrequenz an, schließt die Subjektivität aus und erlaubt die Integration der Messung in die standardisierten Testeinrichtungen. Die Methode verwendet Signalverarbeitung und Systemmodellierung um die maximale Wirkleistung über einen Frequenzbereich in der Chipkarte zu bestimmen. Dazu wird eine Übertragungsfunktion aus dem Modell angewendet und ein sogenanntes Chirp-Signal an den Eingang des Systems angelegt. Das bestimmte Maximum der Wirkleistung wird der entsprechenden Frequenz im Chirp-Signal zugeordnet, was als die neue Resonanzfrequenz definiert ist. Die Durchführbarkeit der Methode wird sowohl mittels Simulationen als auch durch Vergleichsmessungen mit der derzeit etablierten Methode nachgewiesen. Die Ergebnisse zeigen, dass die neue Methode wesentliche Vorteile gegenüber der Netzwerkanalysatormethode bietet.

To my family: Tatjana, Zoran, and Ksenija

Acknowledgements

I would like to express my gratitude to Infineon Technologies Austria AG for offering me the opportunity to complete my diploma thesis in such a professional work environment. I am grateful to Thomas Grieshofer for introducing me to the wonderful world of RFID, and to Christian Lanschützer for letting me be a part of this amazing team. A very special gratitude goes out to Josef Gruber, who provided me with great help and advice throughout this journey, and to Stephan Rampetzreiter, who gave such valuable inputs and feedback. Finally, I am deeply grateful to Prof. Holger Arthaber for his highly professional support while supervising this thesis.

None of this would have been possible without the incredible sacrifice of my family that allowed me to come to Austria for my studies. My greatest thanks therefore go to my parents, Tatjana and Zoran, and to my sister Ksenija, for believing in me all this time and providing me with their love and support.

Contents

1	Introduction	1
1.1	Motivation	1
1.2	Structure of Thesis	2
2	RFID Basics	3
2.1	Main Components	3
2.1.1	Reader	3
2.1.2	Transponder	4
2.2	Classification of RFID Systems	5
2.2.1	Operation Type	6
2.2.2	Operating Frequency and Range	7
2.3	The RFID System in Focus	10
3	Theoretical Fundamentals	11
3.1	Magnetic Field and Inductive Coupling	11
3.1.1	Near and Far Field	12
3.1.2	Magnetic Field Strength H	12
3.1.3	Magnetic Flux and Magnetic Flux Density	13
3.1.4	Inductance L	14
3.1.5	Mutual Inductance M and Coupling Coefficient k	15
3.1.6	Faraday's Law and Lenz's Law	17
3.1.7	Inductively Coupled Coils	18
3.2	Energy Transfer and Resonance	19
3.2.1	Resonant Circuits	20
3.2.2	Quality Factor Q	22
4	System Description	25
4.1	Equivalent Circuits	25
4.1.1	Coupling Elements	25
4.1.2	PCD	27
4.1.3	PICC	28

4.1.4	Transformed Impedance \underline{Z}_T	30
4.2	Data Communication	32
4.2.1	Downlink	32
4.2.2	Uplink	33
4.3	ISO Test PCD Assembly	36
4.3.1	Structure	37
4.3.2	Circuit Model	39
4.3.3	Calculation of Magnetic Field Strength H	43
4.3.4	ISO Measurement Setup	46
5	The Vector Network Analyzer Measurement Method	48
5.1	Definition of Resonance Frequency	48
5.1.1	Phase Resonance	49
5.1.2	Maximum U_{IC}	51
5.1.3	Maximum $\Re\{Z_{VNA}\}$	52
5.1.4	Comparison of Different Definitions	55
5.2	Measuring the Resonance Frequency	56
5.3	Disadvantages of the VNA method	58
6	Theory of the Extended Measurement Method	60
6.1	Active Power in the PICC	60
6.2	Relative Active Power P_{REL}	64
6.3	Shaping of U_{PICC}	68
6.4	$U_{SC} \rightarrow I_{PICC}$ Transfer Function	76
6.5	Phase Angle φ	80
6.6	Determining Resonance Frequency from P_{REL}	81
7	Extended Method in a Simulation Environment	84
7.1	Simulation of the PICC	84
7.2	The System Model	88
7.2.1	Simulation of the Extended Method	90
7.2.2	Feasibility Study	101
8	Implementation of the Extended Method	103
8.1	Differences from the Model	103
8.2	Performed Measurements	105
8.2.1	Passive Components	107
8.2.2	Commercial ICs	109
8.3	Measurement Reproducibility	114
8.4	Measurement Accuracy	117

CONTENTS

9 Conclusion **118**

 9.1 Summary 118

 9.2 Advantages over VNA Method 119

 9.3 Outlook 120

References **121**

Abbreviations

AC	...	Alternating Current
ADS	...	Advanced Design System
ASK	...	Amplitude Shift Keying
AWG	...	Arbitrary Waveform Generator
CC	...	Calibration Coil
DC	...	Direct Current
EAS	...	Electronic Article Surveillance
FDX	...	Full Duplex
FFT	...	Fast Fourier Transform
FSK	...	Frequency Shift Keying
HDX	...	Half Duplex
HF	...	High Frequency
IC	...	Integrated Circuit
ID	...	Identification
IEC	...	International Electrotechnical Commission
ISO	...	International Organization for Standardization
LF	...	Low Frequency
PCD	...	Proximity Coupling Device
PICC	...	Proximity Integrated Circuit Card
PSD	...	Power Spectral Density
PSK	...	Phase Shift Keying
RF	...	Radio Frequency
RFID	...	Radio Frequency Identification
SEQ	...	Sequential
SC	...	Sense Coil
UHF	...	Ultra High Frequency
VNA	...	Vector Network Analyzer
ZP	...	Zero Padding

Chapter 1

Introduction

This introductory chapter is intended to familiarize the reader with contactless chip cards and their common applications, and to present the motivation behind the importance of defining and measuring the resonance frequency of these systems. In addition, information about how this thesis is organized is provided in this chapter.

1.1 Motivation

Radio Frequency Identification (RFID) is a communication technology that utilizes electric and magnetic fields in order to achieve *contactless* identification procedures. One of the most important applications of RFID is the *contactless chip card*, an integral component of everyday life found in bank cards used for payment, for example. Other important uses of chip cards are in identity verification (ePass, eID), ticketing (public transport), and access control (company cards).

This thesis focuses primarily on proximity coupling contactless chip cards that have a carrier transmission frequency of 13.56 MHz and rely on the principle of inductive coupling. This principle is based on the phenomenon of electromagnetic induction that allows both the energy transfer and the communication to be performed without any physical contact between the chip card and the reader. Also closely related to inductive coupling is the phenomenon of resonance and its occurrence in electric circuits, making resonance frequency an essential parameter in development, and especially in verification of contactless chip cards. That means that information about resonance frequency is often required, so that measuring or changing this frequency presents an important task.

There is no absolute resonance frequency defined in the case of contactless chip cards, because resonance frequency varies with respect to power which is being fed into the chip card. As a consequence, measuring this frequency increases in complexity, which is mainly due to the fact that there is no physical contact between a laminated chip card and a measuring device, demanding use of contactless measurement methods. The currently established method for measuring resonance frequency of chip cards is based on using a vector network analyzer and determining the maximum real part of the measured impedance. It shall be seen that this method has certain disadvantages, mainly due to an assumed definition of resonance frequency that is inherently flawed when the resonance frequency is defined otherwise. It also incorporates a deal of subjectivity when it comes to adjusting the aforementioned input power level to the chip card, which may lead to different results due to human error. Therefore, a new method for measuring resonance frequency shall be presented in this thesis, a method that improves the current method regarding the definition of resonance frequency, and that removes the possibility of human error when setting the input power level. The new method is based on the ISO test PCD assembly, which is a standardized apparatus used for many other tests in verification of contactless chip cards. This represents another advantage of the new method, which is that it allows measurement of resonance frequency to be integrated into the already existing measurement setups used for verification.

1.2 Structure of Thesis

This thesis is organized in nine chapters, where chapter 2 gives a basic overview of RFID communication technology and its systems, followed by chapter 4 that elaborates on the physical principles that make operation of RFID systems possible. Chapter 4 focuses only on the system system components at hand, which are the proximity coupling contactless chip card and the ISO test PCD assembly.

Having the system components properly introduced, the measurement method for resonance frequency that is currently the industry standard is described in chapter 5. Motivated by the pitfalls of the current method, a theoretical proposal for a new measurement method is given in chapter 6. Before implementing the new method, its feasibility is investigated in chapter 7 through simulations performed on a model that is constructed for the system. After feasibility is confirmed, results from actual measurements are featured in chapter 8 and the new method is discussed in terms of measurement reproducibility and accuracy. Finally, chapter 9 offers a conclusion of the entire thesis and gives a promising outlook for the future of the new measurement method.

Chapter 2

RFID Basics

An overview of the basic principles of RFID communication, along with its core components is presented in this chapter. Two main devices, the reader and the transponder, are briefly introduced, followed by a classification of various other RFID systems in terms of operating frequency, range, operation type, and other important parameters. At the end of the chapter, a summary is given for the main characteristics of the proximity coupling contactless chip card, which is the RFID system of interest in this thesis.

2.1 Main Components

Two integral components of all RFID systems are the interrogating device, usually regarded as the *reader* and the *transponder*. The main role of the reader is, as the name implies, to receive data from the transponder. A two-way communication, i.e. to send data, is not necessarily a feature of all readers, as some simple systems only require the reader to be able to identify a tag from the transponder. In the case of proximity coupling chip cards acting as transponders, a two-way communication is ensured, of course. In RFID systems, transponders are considered the main data-carrying devices, and they can be designed in a variety of shapes or forms, with different levels of complexity, all depending on the particular application. A typical RFID system is shown in fig. 2.1.

2.1.1 Reader

RFID readers can strongly vary in their features and implementations, but a typical reader consists of a radio frequency unit with a receiver and a transmitter, including some sort of coupling element with the transponder, and a control unit.

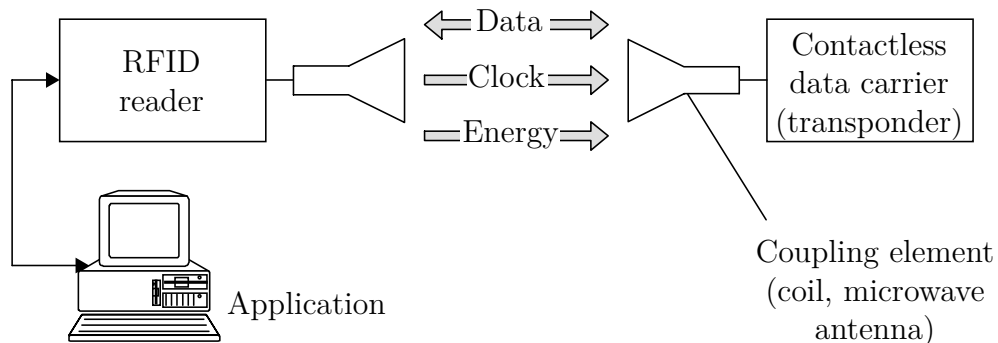


Figure 2.1: An RFID-System (adapted from [1])

Despite being designed for contactless operation, some readers incorporate wired, contact-based interfaces in order to communicate with other hosts such as PCs or robot control systems. In the case of passive transponders, the entire power supply for the transponder is provided by the reader. This is most commonly achieved by using magnetic (inductive) coupling technology, where both the data communication and the power supply are achieved using the same electromagnetic field. Role of the control unit is to oversee the communication with the transponder. However, in more sophisticated reader designs, this role is extended with more complex functionalities such as *anti-collision* protocols (when dealing with more than one transponder at once), *authentication* procedures, or *data encryption* algorithms.

2.1.2 Transponder

Considering the range of data processing features of transponder designs, on the *low-end* side of the spectrum are the simple 1-bit systems used, for example, in electronic article surveillance systems (EAS). These 1-bit systems can only distinguish between two types of situations: “transponder in the interrogation area” and “transponder not in the interrogation area”. From there, RFID transponder designs increase in complexity toward *mid-range* systems, which include writable data memory and are able to process simple reader commands by the use of a hard-wired state machine logic. Some of these systems also support the aforementioned *anti-collision*, *authentication*, and *data encryption* procedures. However, in order to provide the sophisticated cryptographic features for high security applications, the *high-end* systems found on the other side of the spectrum need to be used. Instead of a state-machine, they incorporate a microprocessor and a smart card operating system, sometimes with a separate cryptographic co-processor that ensures the high level of security required for government IDs and electronic passports.

2.2 Classification of RFID Systems

Another distinguishing feature of transponders is the origin of power supply, which can be either *active* or *passive*. The power supply of active transponders is an actual part of the system, in form of an energy source like a battery, whereas passive transponders require an external power supply, which is usually provided by the reader's electromagnetic field. Similar to the reader, the coupling element is an important part of the transponder as well, and it ensures that coupling with the reader can be achieved. Passive transponders utilize the same coupling element with a dual purpose: as power supply and also for data transfer. In this second regard, the coupling element takes over the role of the transmitter/receiver and is therefore often referred to as the *antenna*. Fig. 2.2 depicts two passive transponders along with their microchip units that provide memory and general control of the transponder system.

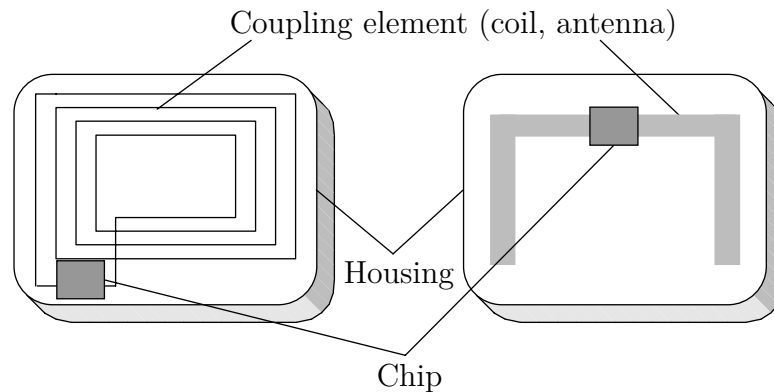


Figure 2.2: Basic layout of transponders: inductively coupled transponder with antenna coil (left), microwave transponder with dipole antenna (right) (adapted from [1])

Despite the vast variety of transponder designs in terms of their concept and miniaturization, this thesis shall focus on one particular design that is most common in the majority of proximity coupling chip card applications: the *ID-1 format*. It is the standard format of most credit cards and other types of cards, such as public transportation tickets or ID cards. A typical example of the ID-1 format can be seen in fig. 2.3.

2.2 Classification of RFID Systems

When it comes to RFID systems, one can choose from a variety of features on which the classifying criterion is based. Some of these, such as information processing range (low-end, mid-range, high-end), power supply (active or passive),

and construction format (ID-1) have already been mentioned. Some further differentiating characteristics, particularly in terms of operating frequency, coupling range, and operation type shall be discussed next.

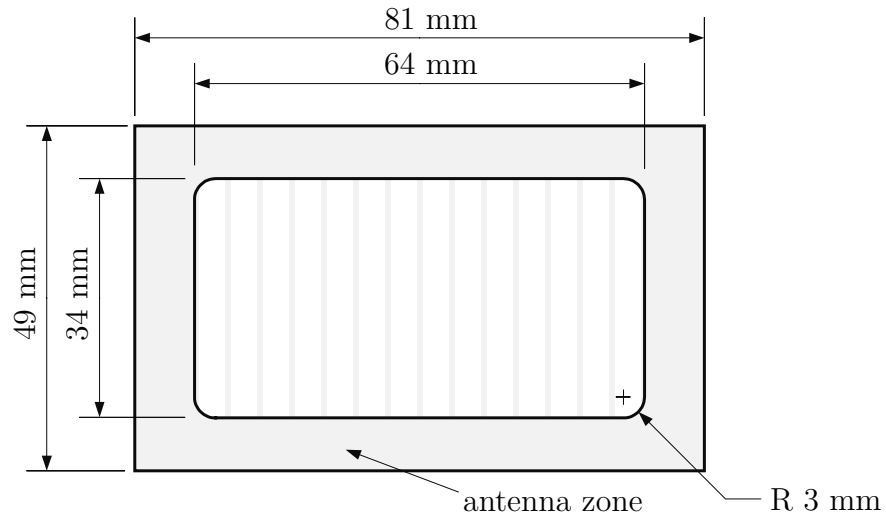


Figure 2.3: The ID-1 format (adapted from [2])

2.2.1 Operation Type

A typical RFID system can operate according to one of the following two procedures: *full-duplex* (FDX)/*half-duplex* (HDX) mode on the one hand, and *sequential* mode (SEQ) on the other hand. The fundamental difference between these contrasting operation modes has to do with the behavior of the reader's RF field while the transponder is sending its own data.

In FDX/HDX mode, the reader's electromagnetic field stays turned on during communication from transponder to reader. The downside of this mode is that the transponder signal is weak in comparison to the reader's field. This requires a solution by applying special transmission techniques so the transponder's signal can be extracted and received, despite the stronger field of the reader. Some of the techniques that are used today are load modulation with a sub-carrier or sub-harmonics of the reader's transmission frequency.

Sequential procedures, on the other hand, introduce gaps at regular time intervals by appropriately switching off the reader's field. The transponder identifies these gaps and uses the chance to send its own data during this time. An obvious negative consequence of SEQ mode is that turning off the reader's field destabilizes the power supply of passive transponders, so that energy storage elements such as auxiliary capacitors need to be added to the system.

Fig. 2.4 visualizes the conceptual differences between the three mentioned operation types.

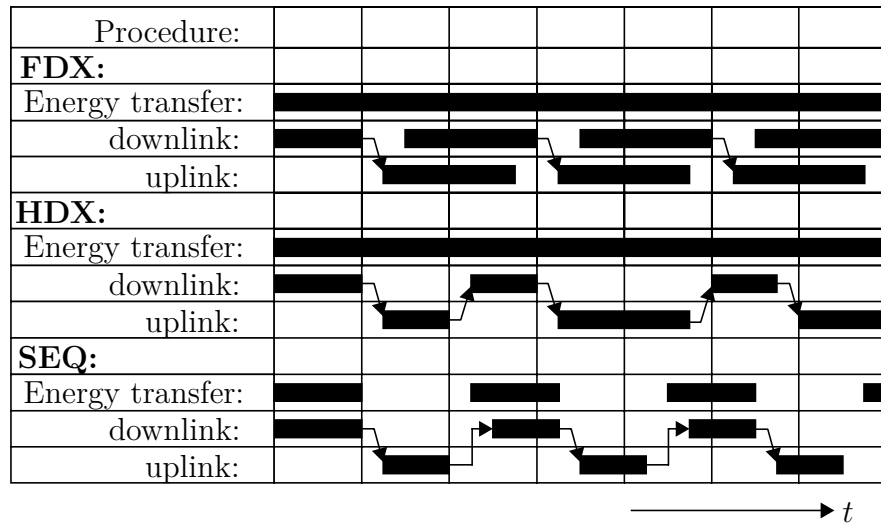


Figure 2.4: Representation of full-duplex, half-duplex, and sequential systems over time. Data transfer from the reader to the transponder is termed downlink, while data transfer from the transponder to the reader is termed uplink (adapted from [1])

2.2.2 Operating Frequency and Range

The frequency at which RFID systems operate is defined by the transmission frequency of the reader, which belongs to one of the frequency bands shown in table 2.1.

Table 2.1: Operating frequency bands of an RFID system

Band	Frequency	Unit
Low frequency (LF)	30...300	kHz
High frequency (HF)	3.....30	MHz
Microwave range	0.3 and above	GHz

An important parameter in RFID communication is the area inside of which the data exchange between reader and transponder is possible. This area is usually denoted as the *interrogation zone*, so that, by definition, the transponder is only active when located within this zone. For that reason, the range of RFID

2.2 Classification of RFID Systems

systems is an important parameter that strongly influences the other parameters, thus being a decisive factor on the choice of operating frequency and coupling mechanism for the particular system. In this context, one can distinguish between *close coupling*, *remote coupling*, and *long range* systems (tab. 2.2).

Table 2.2: Various coupling mechanisms of an RFID system, including their ranges

Coupling mechanism	Range
Close coupling	0...0.01 m
Remote coupling	0...1 m
Long range	above 1 m

2.2.2.1 Close Coupling

Close coupling systems tend to have a range up to 1 cm, and it is usually necessary for the transponder either to be inserted into the reader or to be placed on some sort of a special surface that is required for coupling. The actual coupling mechanism uses both electric and magnetic fields, albeit without their radiative properties. Therefore, the operating frequency can be arbitrarily chosen from DC up to 30 MHz. Another advantage of close coupling systems is the power supply, which presents no obstacle, due to the transponder being very close to the reader. These systems find their use in increased security applications without a long range requirement, such as bank payment that uses the typical ID-1 format contactless smart cards according to ISO 10536.

2.2.2.2 Remote Coupling

Remote coupling systems have a range up to 1 m and are almost exclusively based on inductive coupling, with an exception of a few systems that use capacitive (electric) coupling. Inductive coupling of passive transponders is not strong in terms of energy transfer, so special attention must be given to the aspect of power supply. The coupling elements used in these systems are coils, however they are usually referred to as antennas, because as mentioned before, data transfer is also provided through them. There are two sub-categories of remote coupling systems: *proximity coupling* and *vicinity coupling* systems. Their main differences with respect to range and the appropriate ISO standard are shown in fig. 2.5. As far as transmission frequencies are concerned, typical values are 135 kHz or 13.56 MHz, and 27.125 MHz in some special cases.

Considering how the main focus of this thesis are proximity coupling systems, the important nomenclature used for reader and transponder in case of contactless

chip cards shall be introduced here: *Proximity Coupling Device* (PCD) is the term used for the reader, whereas *Proximity Integrated Circuit Card* (PICC) is the term that describes the transponder.

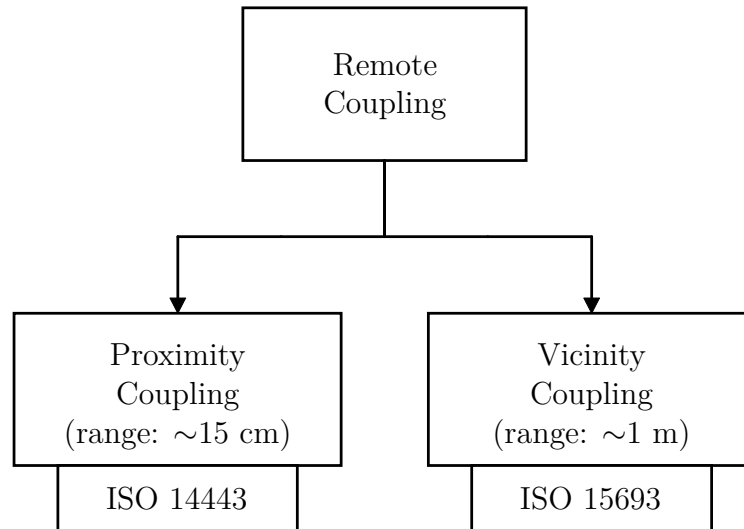


Figure 2.5: Types of remote coupling systems (adapted from [3])

2.2.2.3 Long Range Coupling

If the range of an RFID system is above 1 m, it is considered to be a long range system. These systems are based on actual propagation of electromagnetic waves and are therefore regarded as radio systems in the traditional sense. Frequencies are usually in the UHF (868 MHz and 915 MHz) or microwave (2.5 GHz and 5.8 GHz) range. Systems that communicate over a higher distance use a battery assisted power supply intended only for the transponder chip, but not for data communication, which is based on the principle of *modulated backscattering*: the transponder changes the reflection characteristics of its antenna, and thus decides how much power is reflected back to the reader, which is perceived as incoming data at the reader's end.

2.3 The RFID System in Focus

After listing some important features of various RFID systems and their operation principles, at this point it is necessary to mention the system that is the central focus throughout this thesis: the contactless chip card (fig. 2.6). It falls into the category of proximity coupling systems based on the ISO 14443 standard.



Figure 2.6: A contactless chip card (courtesy of Infineon Technologies Austria AG)

The most important characteristics of chip cards according to the classifying criteria from this chapter are shortly summarized here.

Operation type:	HDX
Power supply type:	passive
Operating frequency:	13.56 MHz
Range:	remote coupling (up to 10 cm)
Coupling principle:	inductive coupling
Data communication:	Uplink \Rightarrow load modulation Downlink \Rightarrow various modulation techniques
Standard:	ISO 14443

Chapter 3

Theoretical Fundamentals

This chapter introduces the fundamental theory behind the working principle of proximity coupling contactless chip cards. Starting from the basics of magnetic field theory, explanations are directed towards understanding its most important application: the inductive coupling. Focus of this chapter is then shifted to the concepts of energy transfer in passive transponders, introducing the phenomenon of resonance along with its two most important attributes: the resonance frequency and the quality factor.

3.1 Magnetic Field and Inductive Coupling

An unavoidable characteristic of any moving charge (i.e. current) is the fact that it generates a corresponding magnetic field as a consequence. In his famous law of induction, Faraday managed to show that the opposite effect is also true: bringing a conductor into a magnetic field results in a flow of current through the conductor. Furthermore, it is a known fact that two physically separate conductors are able to influence one another by means of their magnetic fields, an effect that is called *inductive coupling*. Most common example of this is the transformer: two coils, one primary and one secondary, are inductively coupled in order to transfer power from the primary to the secondary coil and thus change the voltage. In a similar fashion, proximity coupling RFID systems use inductive coupling between reader and transponder to transfer energy and exchange data. This section is intended to further elaborate on these principles.

3.1.1 Near and Far Field

A necessary condition for proximity coupling transponders is to neglect the effects of electromagnetic wave propagation. To do this, the transponder needs to stay within the non-radiative near field of the reader's antenna. Transition from near to far field depends on the distance from the antenna and is given, as a rule of thumb, by the following expression:

$$r_{NF} = \frac{\lambda}{2\pi}$$

For proximity coupling transponders operating at 13.56 MHz, the wavelength can be determined by the well-known relation between speed of light and frequency:

$$\lambda = \frac{c_0}{f} = \frac{3 \cdot 10^8 \text{ m/s}}{13.56 \cdot 10^6 \text{ Hz}} \cong 22.1 \text{ m} \quad (3.1)$$

The near field range thus amounts to:

$$r_{NF} \approx 3.52 \text{ m}$$

which is in this case well within the antenna's near field.

3.1.2 Magnetic Field Strength \mathbf{H}

The physical quantity that describes the magnitude and direction of a magnetic field is the *magnetic field strength* \mathbf{H} . Mathematically, \mathbf{H} is a vector field and its relation with the current is given by *Ampere's law*, which says that the closed loop integral of the field strength equals the sum of the currents flowing through the area \mathcal{A} surrounded by the loop $\partial\mathcal{A}$ (eq. 3.2). Fig. 3.1 on the left shows the circular magnetic field lines created by current flow through a straight conductor, whereas the figure on the right shows what the magnetic field lines look like when current flows through a coil.

$$\int_{\partial\mathcal{A}} \mathbf{H} \cdot d\mathbf{s} = \sum I_n \quad (3.2)$$

In the case of inductively coupled RFID systems, the antennas for magnetic field generation are realized as planar cylindrical coils. The field strength depends on several parameters, such as geometry of the coil or the location of the measuring point. If the x axis is placed along the coil's central axis, then the magnetic field strength H along the x axis can be expressed using eq. 3.3, where I is the current, R is the radius, and N is the number of windings. The distance from the origin in the coil's center is given by x .

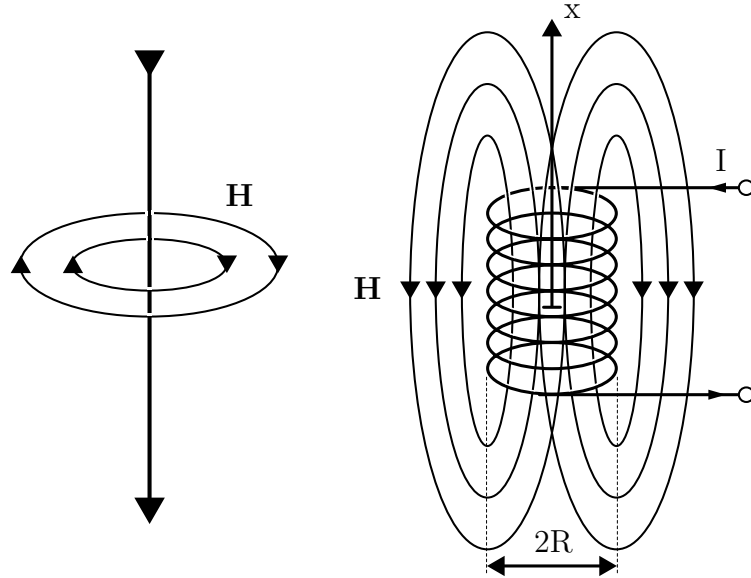


Figure 3.1: Magnetic field lines around current-carrying conductors: straight conductor (left) and cylindrical coil (right) (adapted from [1])

$$H = \frac{INR^2}{2\sqrt{(R^2 + x^2)^3}} \quad (3.3)$$

Analyzing eq. 3.3 by varying x and keeping R constant, and vice versa, it can be determined that the field strength tends to remain constant up to a certain distance x before it starts to quickly decay. Smaller coils tend to have a higher field strength at shorter distances compared to the larger coils. On the other hand, larger coils are able to maintain a constant H for greater distances before H starts to decay. In addition, there is also an optimal radius for each particular distance from the coil. These relationships need to be taken into consideration in order to achieve optimal antenna design.

3.1.3 Magnetic Flux and Magnetic Flux Density

Two further physical quantities that are fundamental for understanding magnetic fields are the *magnetic flux* Φ and the *magnetic flux density* \mathbf{B} . Magnetic flux passes through a certain area \mathcal{A} , whereas magnetic flux density refers to an area that is infinitely small (fig. 3.2). Eq. 3.4 describes the mathematical relation between Φ and \mathbf{B} .

$$\Phi = \int_{\mathcal{A}} \mathbf{B} \cdot d\mathbf{A} \quad (3.4)$$

3.1 Magnetic Field and Inductive Coupling

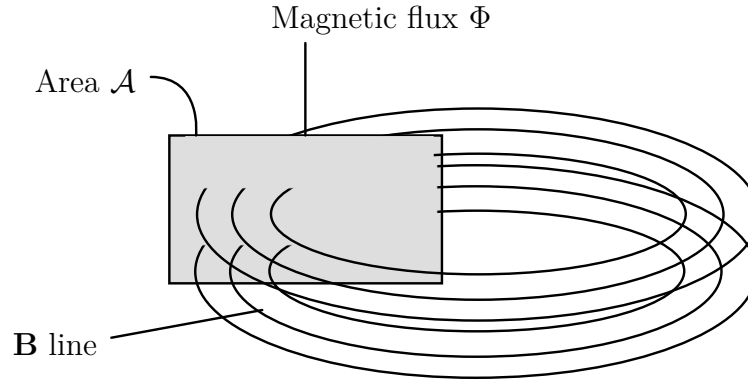


Figure 3.2: Relationship between magnetic flux Φ and flux density \mathbf{B} (adapted from [1])

Magnetic flux density \mathbf{B} and magnetic field strength \mathbf{H} are connected to one another through material relation given in eq. 3.5. Material properties, including statistical averaging of magnetic dipole moments after the material was magnetized by the magnetic field, are expressed through the magnetic permeability μ . The magnetic field constant μ_0 describes the permeability of a vacuum, while the relative permeability μ_r expresses the ratio of a certain material's permeability to that of a vacuum.

$$\mathbf{B} = \mu_0 \mu_r \mathbf{H} = \mu \mathbf{H} \quad (3.5)$$

μ_0 ... magnetic field constant ($\mu_0 = 4\pi \cdot 10^{-7} \text{ Vs/Am}$)
 μ_r ... relative permeability of the material (e.g. $\mu_{r,air} = 1$)

3.1.4 Inductance L

It has already been established that current flow through an electric conductor generates an encircling magnetic field. In the case of a cylindrical coil, the same current I flows through each of the loops and therefore generates the same magnetic flux Φ multiple times, one for each loop enclosing the area \mathcal{A} (fig. 3.1 on the right). The total magnetic flux Ψ of a cylindrical coil is thus dependent on the number of windings N (eq. 3.6).

$$\Psi = \sum_N \Phi_N = N\Phi = N \int_{\mathcal{A}} \mathbf{B} \cdot d\mathbf{A} = N \int_{\mathcal{A}} \mu \mathbf{H} \cdot d\mathbf{A} \quad (3.6)$$

The proportionality factor between current I and magnetic flux Φ is expressed by the *inductance* L , which is one of the most important physical quantities that

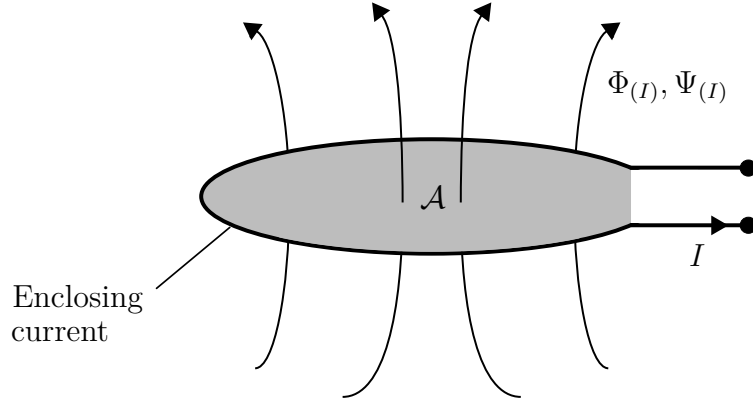


Figure 3.3: Definition of inductance L (adapted from [1])

describe the magnetic field (fig. 3.3). In the case of cylindrical coil conductor, inductance is determined based on the total flux Ψ (eq. 3.7).

$$L = \frac{\Psi}{I} = \frac{N\Phi}{I} = \frac{N\mu HA}{I} \quad (3.7)$$

Inductance contains information about material properties with respect to both the magnetic permeability and the geometry of the conductor through which magnetic flux is passing. Calculating inductance analytically presents a difficult task, which is the reason why approximations are mainly used in the calculations. For example, under the assumption that the diameter d of the cylindrical coil wire is very small in comparison with the coil's loop diameter D ($\frac{d}{D} < 0.001$), a simple approximation (eq. 3.8) can be used to calculate the inductance.

$$L = N^2\mu_0 \frac{D}{2} \ln\left(\frac{D}{d}\right) \quad (3.8)$$

3.1.5 Mutual Inductance M and Coupling Coefficient k

If a conductor, enclosing an area \mathcal{A}_1 and having a current I_1 flowing through it, happens to find itself in the vicinity of another conductor with an area \mathcal{A}_2 , then a certain portion of the magnetic flux Φ that flows through \mathcal{A}_1 is able to flow through \mathcal{A}_2 as well (fig. 3.4). This *partial* magnetic flux allows the second conductor to be coupled with the first conductor, which is the main principle of inductive coupling. The relationship of the partial flux (also called *coupling* flux), between the two conductors is expressed through the so-called *mutual inductance* M . If the first conductor is the current-carrying conductor, then M_{21} is defined as the ratio of the partial magnetic flux Φ_{21} enclosed by the second conductor and the current I_1 from the first conductor (eq. 3.9).

3.1 Magnetic Field and Inductive Coupling

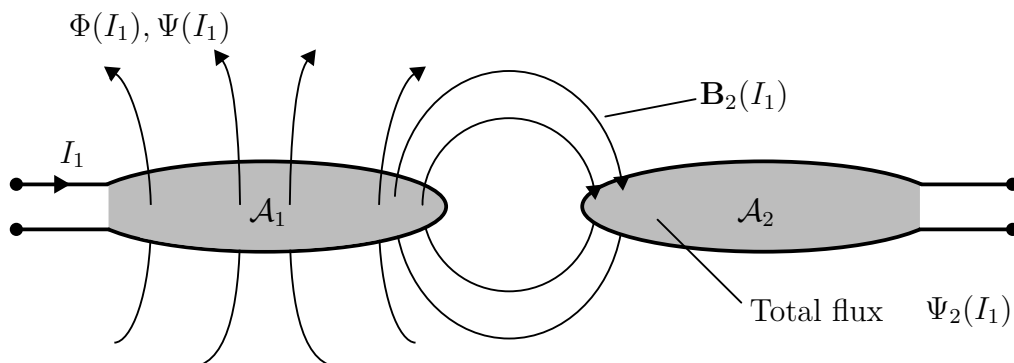


Figure 3.4: The definition of mutual inductance M_{21} by the coupling of two coils via a partial magnetic flux (adapted from [1])

$$M_{21} = \frac{\Phi_{21}(I_1)}{I_1} = \int_{\mathcal{A}_2} \frac{\mathbf{B}_2(I_1)}{I_1} \cdot d\mathbf{A}_2 \quad (3.9)$$

There are several parameters that influence the magnitude of the partial flux Φ_{21} , such as geometry, magnetic properties of the materials involved, and relative position of the conductors to one another. There is also a mutual inductance M_{12} , in which case the current I_2 is flowing through the second conductor, and the partial flux Φ_{12} is flowing through the first conductor. Due to reciprocity, M_{21} and M_{12} are equal:

$$M = M_{12} = M_{21} \quad (3.10)$$

In the case where the conductors are cylindrical coils, the corresponding partial flux Φ_{21} in eq. 3.9 needs to be replaced with the total flux Ψ_{21} that incorporates the number of windings N_2 in the second coil:

$$M_{21} = \frac{\Psi_{21}(I_1)}{I_1} = \frac{B_2(I_1)N_2A_2}{I_1} = \frac{\mu H(I_1)N_2A_2}{I_1} \quad (3.11)$$

In order to describe the coupling between two coils qualitatively, regardless of their geometrical properties and number of windings, a dimensionless quantity called the *coupling coefficient* k is introduced:

$$k = \frac{M}{\sqrt{L_1L_2}} \quad (3.12)$$

The value of k always ranges between 0 and 1, where $k = 0$ means total decoupling due to distance or magnetic shielding, whereas $k = 1$ stands for total

coupling where the same magnetic flux Φ passes through both coils, as is for example the case with the most important application of total coupling: the transformer.

3.1.6 Faraday's Law and Lenz's Law

Similarly to how every current-carrying conductor generates an accompanying magnetic field, Faraday managed to prove the opposite effect: that an electric field could be generated in an electric conductor by applying a magnetic field. This phenomenon, known as *electromagnetic induction*, states that by acting a time-varying magnetic field upon an electric conductor in a closed loop, an electromotive force (EMF) is produced within the loop. The EMF causes charge in the closed loop to separate, which leads to generation of voltage, which is said to be *induced* by the magnetic field (fig. 3.5). This voltage across a closed loop therefore allows current to flow.

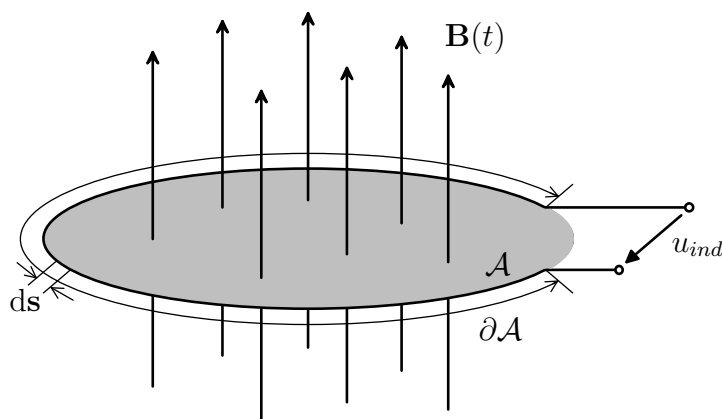


Figure 3.5: Electromagnetic induction (adapted from [1])

The *Faraday's law of induction* defines the induced voltage u_{ind} as the negative change rate of the magnetic flux that passes through the area \mathcal{A} enclosed by the conductor loop. The magnetic field produces the EMF which is expressed by the closed loop integral of the electric field strength \mathbf{E}_{ind} . Thereby ∂ represents the edge operator, in this case edge of an area being a closed loop. The mathematical formulation of Faraday's law is given in eq. 3.13.

$$u_{ind} = \int_{\partial \mathcal{A}} \mathbf{E}_{ind} \cdot d\mathbf{s} = -\frac{d\Phi(t)}{dt} \quad (3.13)$$

There are two different types of electromagnetic induction:

- *self-induction*: If the change of the magnetic flux originates within the same circuit where the voltage is induced, the effect is known as self-induction.

3.1 Magnetic Field and Inductive Coupling

- *mutual induction*: If the change of the magnetic flux originates in an adjacent circuit, different from the circuit where the voltage is induced, the effect is called mutual induction.

The importance of the negative sign in eq. 3.13 is expressed by *Lenz's law*, which describes the direction of the induced EMF, and therefore also the direction of the induced current. According to Lenz's law, the direction of the induced current shall be such that it shall generate a magnetic field that opposes the change in the magnetic field that produced the current in the first place. This can be seen as somewhat analogous to Newton's third law in classical mechanics.

3.1.7 Inductively Coupled Coils

A closer look shall now be taken at a simplified inductively coupled system used in proximity coupling RFID systems. As previously mentioned, coupling elements used in such systems are coils, also referred as antennas by the RFID community. Despite coming in various shapes and sizes, chip card antennas are mostly designed in the rectangular ID-1 format with three or four windings. However, a symbolic representation of two cylindrical coils (fig. 3.6 left), along with a corresponding equivalent circuit diagram (fig. 3.6 right) shall be used here. The reader and transponder antennas are represented by inductances L_1 and L_2 , respectively.

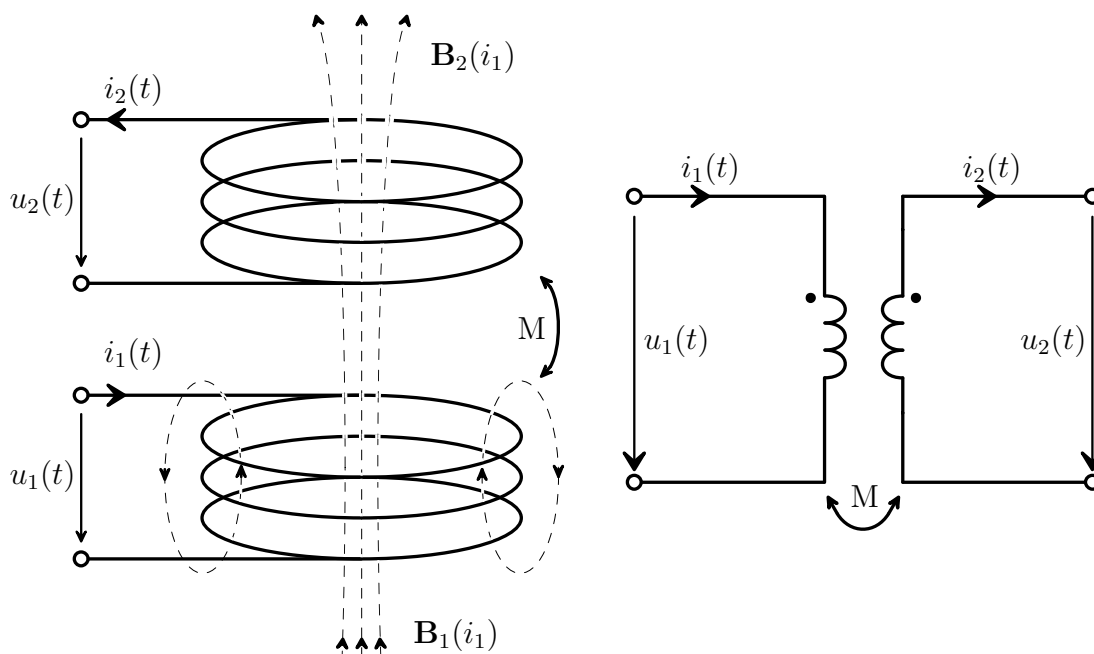


Figure 3.6: Inductively coupled coils (adapted from [1])

3.2 Energy Transfer and Resonance

The flow of current i_1 through the reader's antenna L_1 generates a time-varying magnetic field, expressed by the magnetic flux density $\mathbf{B}_1(i_1)$. This field causes a voltage $u_2(t)$ to be induced in the transponder's antenna L_2 , allowing a current $i_2(t)$ to flow through the transponder, which is considered to be a closed electric circuit itself. The current $i_2(t)$ generates its own magnetic flux after passing through the transponder antenna L_2 . According to Lenz's law, this flux tends to oppose the direction of the flux from which it originated, in this case $\mathbf{B}_1(i_1)$. Mathematically, this counteraction is denoted with a negative sign in the expression for the induced voltage $u_2(t)$ (eq. 3.14).

$$u_2 = \underbrace{M \frac{di_1}{dt}}_{\text{Mutual induction}} - \underbrace{L_2 \frac{di_2}{dt}}_{\text{Self-induction}} \quad (3.14)$$

The effect of Lenz's law can be seen at the reader's side as well. Via mutual induction, the magnetic field of the transponder weakens the reader's field, thereby also indirectly decreasing the current $i_1(t)$. Again, this is modeled with a negative sign in the expression for $u_1(t)$ (eq. 3.15).

$$u_1 = \underbrace{L_1 \frac{di_1}{dt}}_{\text{Self-induction}} - \underbrace{M \frac{di_2}{dt}}_{\text{Mutual induction}} \quad (3.15)$$

Considering how i_1 and i_2 are sinusoidal high frequency AC currents in reality, equations 3.14 and 3.15 can be rewritten using complex AC analysis:

$$\underline{U}_2 = j\omega M \underline{I}_1 - j\omega L_2 \underline{I}_2 \quad (3.16)$$

$$\underline{U}_1 = j\omega L_1 \underline{I}_1 - j\omega M \underline{I}_2 \quad (3.17)$$

$$\omega = 2\pi f \quad (3.18)$$

3.2 Energy Transfer and Resonance

Passive transponders used in proximity coupling RFID systems require the power supply to be provided by the magnetic field of the PCD by inducing a voltage in the PICC via mutual induction. In order to optimize the energy transfer when inductively coupling the PCD with the PICC, resonant circuits are used in both devices. Considering how resonance frequency is the main focus of this thesis, it is initially important to provide some fundamentals about the phenomenon of resonance itself, followed by introducing the physical quantities that describe it more closely. These are the resonance frequency f_{RES} , with its various definitions, and the quality factor Q .

3.2.1 Resonant Circuits

Any electric circuits that contains resistive, capacitive, and inductive components represents a harmonic oscillator that can be driven at a certain frequency to achieve *resonance*, a state where the circuit operates at much higher amplitudes of current and voltage. This frequency is called *resonance frequency* f_{RES} and it has more than one definition, depending on the so-called *resonance conditions*. The figure of merit is the equivalent network impedance $\underline{Z}(j\omega)$ of the circuit, as each of the resonance conditions is, in one way or the other, defined based on $\underline{Z}(j\omega)$:

Phase Resonance: $\Im\{\underline{Z}\} = 0 \rightarrow \omega_{\text{RES},ph}$

Absolute Value Resonance: $\frac{\partial|\underline{Z}|}{\partial\omega} = 0 \rightarrow \omega_{\text{RES},abs}$

Maximum Real Part Resonance: $\frac{\partial\Re\{\underline{Z}\}}{\partial\omega} = 0 \rightarrow \omega_{\text{RES},max}$

The most common resonance condition is the *phase resonance*, which states that voltage and current in an electrical network are in resonance when the voltage is in phase with the current [4]. In other words, phase resonance is achieved when the equivalent network impedance $\underline{Z}(j\omega)$ is purely resistive ($\Im\{\underline{Z}\} = 0$).

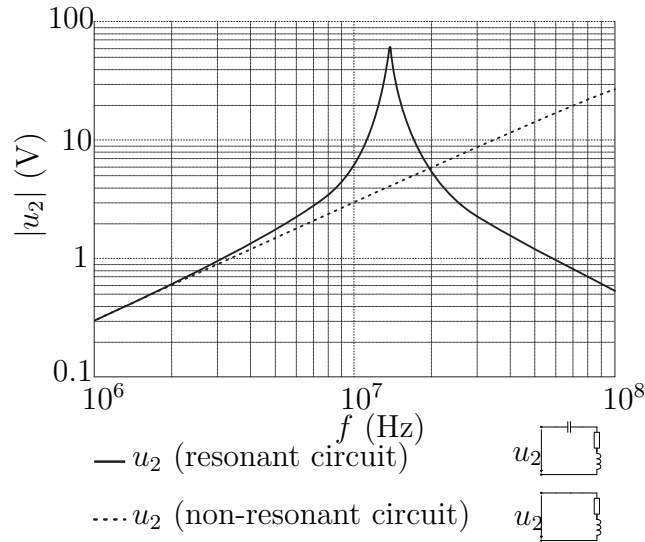


Figure 3.7: Voltage at a transponder coil as function of frequency, given a constant magnetic field strength \mathbf{H} (i.e. constant current i_1), $f_{\text{RES}} = 13.56$ MHz (adapted from [1])

3.2 Energy Transfer and Resonance

The *absolute value resonance* condition, as its name says, is set at the maximum value for the magnitude of \underline{Z} , whereas the *maximum real part resonance* focuses on maximizing only the real part of \underline{Z} . Some additional definitions of resonance shall be introduced later, after more insight is gained about the system that is in the focus of this thesis. For now, however, it is important to know that the term resonance is not absolute, but rather that it contains multiple definitions that are not mutually exclusive, and are dependent on the resonant circuit's desired function.

In the case of proximity coupling RFID systems, resonant circuits are employed in both PCD and PICC in order to optimize energy transfer. The resonance frequency of the circuit is adjusted to match the operating frequency of the system. The inductive coupling system from fig. 3.6 contains no capacitive elements, and is therefore not considered a resonant circuit. If a capacitor is included parallel to the coil in the transponder circuit, the effect of resonance can be seen in fig. 3.7, which shows the induced voltage u_2 over frequency in the cases with and without a capacitor as the resonance element. It can be clearly seen that the voltage rises significantly when circuit is operated at the resonance frequency.

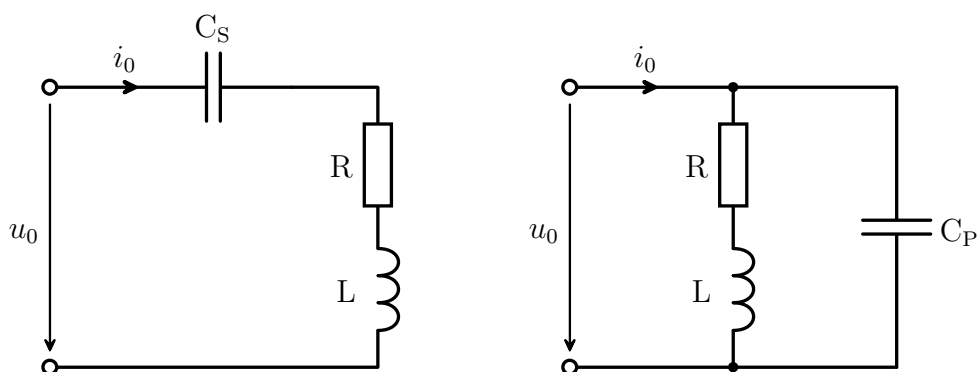


Figure 3.8: Damped resonant circuits: serial (left) and parallel (right) (adapted from [5])

An ideal LC circuit exists only in theory, whereas in reality each coil in an electric circuit is modeled as an ideal inductance L in series with a resistance R , to which losses are attributed. That means that such circuits are damped, so they need to be driven in order to run continuously. When it comes to simple equivalent circuits, two main types of resonance need to be distinguished: *serial* and *parallel* resonance. In the case of proximity coupling systems, the reader is mostly modeled as a damped serial resonant circuit, while the transponder is exclusively represented by a damped parallel resonant circuit (fig. 3.8).

With proximity coupling RFID systems, it can be assumed that the electrical

3.2 Energy Transfer and Resonance

parameter values (inductance and resistance) of reader and transponder antennas are constant, so that for the system to be set at a certain resonance frequency it is the capacitor that needs to be chosen accordingly. The needed capacitance can be determined from the resonance condition. However, there may be a need for the system to sometimes be operated at a different resonance frequency, which means that the capacitance is required to be variable. In such resonant circuits, varying the capacitance in order to set a specific resonance frequency is regarded as *tuning*.

In the serial resonant circuit (fig. 3.8 on the left), equivalent network impedance \underline{Z}_{ser} can be determined as:

$$\underline{Z}_{ser} = \frac{1}{j\omega C_S} + R + j\omega L = R + j\left(\omega L - \frac{1}{\omega C_S}\right) \quad (3.19)$$

The resonance frequency can be determined by evaluating one of the already mentioned resonance conditions. For example, setting the most common condition, the phase resonance, leads to the following expression for $\omega_{RES,ser}$:

$$\Im\{\underline{Z}_{ser}\} \stackrel{!}{=} 0 \Rightarrow \omega_{RES,ser} = \frac{1}{\sqrt{LC_S}} \quad (3.20)$$

Finally, replacing $\omega_{RES,ser}$ with $2\pi f_{RES,ser}$ results in the *Thomson's equation* for serial resonant circuits:

$$f_{RES,ser} = \frac{1}{2\pi\sqrt{LC_S}} \quad (3.21)$$

Thomson's equation can also be derived for the parallel resonant circuit (fig. 3.8 on the right), where it has a slightly different form:

$$f_{RES,par} = \frac{1}{2\pi} \sqrt{\frac{1}{LC_P} - \frac{R^2}{L^2}} \quad (3.22)$$

3.2.2 Quality Factor Q

Beside resonance frequency, another important term associated with resonance is the *quality factor* Q [4]. Its most general definition in relation with the resonance frequency ω_{RES} is given as:

$$Q = \omega_{RES} \frac{\text{energy stored in resonator}}{\text{energy dissipated per cycle}} \quad (3.23)$$

When it comes to resonant circuits, Q represents either voltage or current magnification that occurs at resonance frequency. Therefore, the quality factor

3.2 Energy Transfer and Resonance

is an important parameter that describes both the PCD and the PICC circuit in an RFID system.

For a typical serial LCR circuit, the quality factor $Q_{\text{RES},ser}$ at resonance is derived based on eq. 3.23 [4], while also including the Thomson's equation (eq. 3.20), resulting in:

$$Q_{\text{RES},ser} = \frac{\omega_{\text{RES}}L}{R} = \frac{1}{\omega_{\text{RES}}C_S R} = \frac{1}{R} \sqrt{\frac{L}{C_S}} \quad (3.24)$$

As opposed to serial circuits where the quality factor Q is a measure of voltage magnification, Q is determined by magnification of the current in parallel resonant circuits. It is defined as the ratio between the current circulating in the parallel branches of the circuit and the supply current [4]. However, derivation of $Q_{\text{RES},par}$ yields the same expression as with serial resonant circuits:

$$Q = \frac{\text{circulating current}}{\text{current at resonance}} \quad (3.25)$$

$$\Rightarrow Q_{\text{RES},par} = \frac{\omega_{\text{RES}}L}{R} \quad (3.26)$$

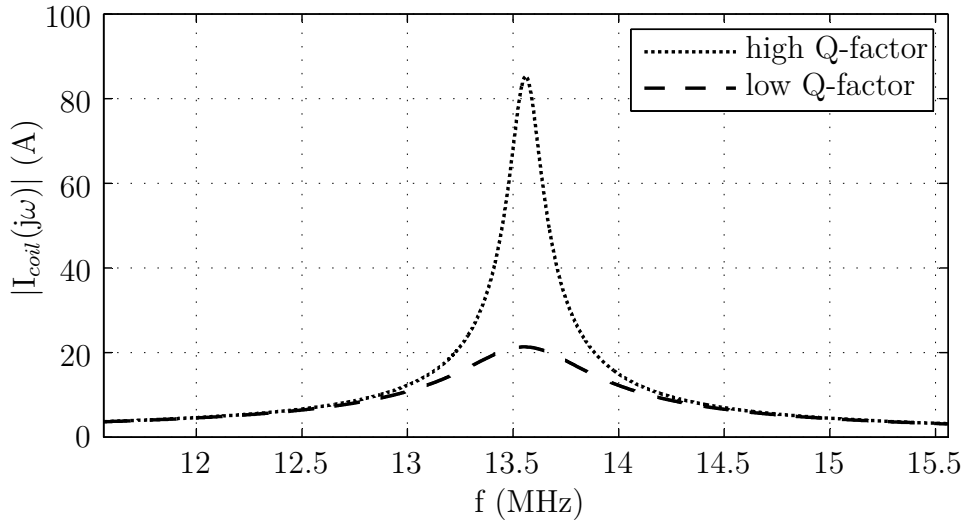


Figure 3.9: Current magnification of a parallel resonant circuit for different Q-factors (adapted from [5])

The influence of the quality factor can be seen in fig. 3.9, with an obvious change in current magnification for a parallel resonant circuit tuned to 13.56 MHz. Changing the coil's resistance between two different values results in a change of

3.2 Energy Transfer and Resonance

the quality factor, and hence in a different value of the current flowing through the coil.

However, aspiring towards higher values of Q does not come without paying some sort of price, which has to do with the *bandwidth* of the circuit. Bandwidth B is defined as the range of frequencies for which the circuit's power gain does not drop below half of the maximum value. For the amplitude gain, this corresponds to the difference between the two 3 dB points, representing $\frac{1}{\sqrt{2}}$ of the maximum value (fig. 3.10).

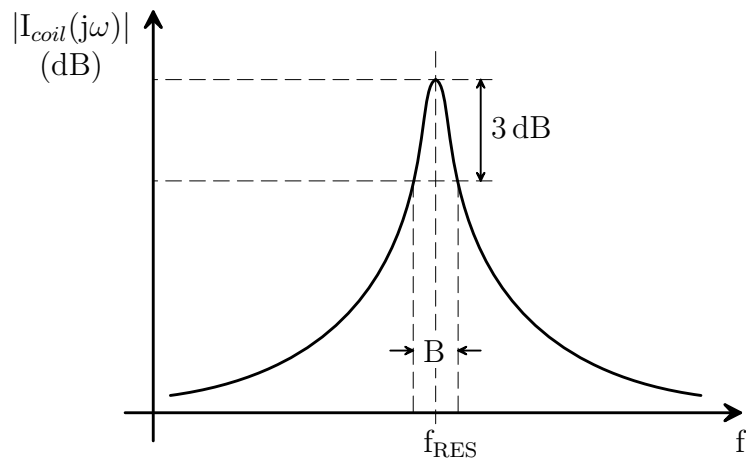


Figure 3.10: Bandwidth of a resonant circuit (adapted from [5])

Taking another look at fig. 3.9 shows that current magnification in the high Q case tends to fall off more abruptly when the frequency deviates from f_{RES} . Together with the half-power point (i.e. 3 dB) definition of bandwidth B , this means that quality factor and bandwidth stand in an inverse relation to one another:

$$Q_{RES} = \frac{f_{RES}}{B} \quad (3.27)$$

As a consequence, an appropriate compromise should be reached between Q and B . High Q results in high voltage and current magnification, but at the cost of slightly slower rise times. On the other hand, high bandwidth enables less attenuated side lobes and shorter rise times, at the cost of requiring more power to be fed into the system.

Chapter 4

System Description

Before delving into the methods for measuring the resonance frequency, a more detailed understanding of the proximity coupling RFID system is required. This chapter describes the PCD and the PICC from the circuit modeling standpoint, followed by introduction of an important modeling parameter: the transformed impedance \underline{Z}_T . Some insight in the data communication principle is also given, although mainly focusing on the circuit aspect of load modulation and its relation to \underline{Z}_T . The final section deals with the ISO test PCD assembly, a standardized system for research, development and verification of proximity coupling readers and transponders.

4.1 Equivalent Circuits

Building up on the theory and principles from the previous chapter, it is at this point reasonable to raise the level of abstraction and regard the system from the electrical perspective using the concept of equivalent electric circuits. This shall be done for both PCD and PICC, including variations in the level of detail of the circuit model. On the other hand, influence of the PICC on the magnetic field of the PCD can be modeled with a single parameter in the PCD equivalent circuit, called transformed impedance \underline{Z}_T . Derivation and importance of \underline{Z}_T shall also be discussed in this section.

4.1.1 Coupling Elements

As stated in the previous chapters, coils are the main coupling elements of proximity coupling RFID systems. An ideal coil is modeled as a pure inductance in an electric circuit. In practice, however, there is always some serial resistance R_L

and parasitic capacitance C_L that accompanies the inductance L . Therefore, a serial resistance and a parallel parasitic capacitance are included in the equivalent circuit of a non-ideal coil (fig. 4.1).

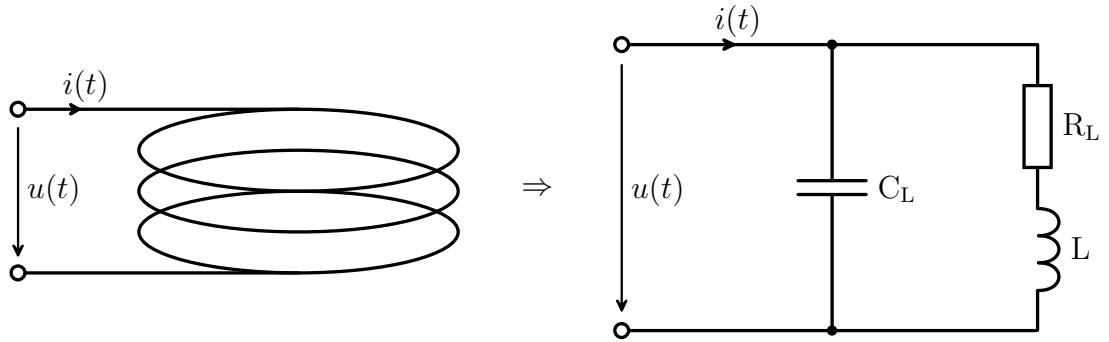


Figure 4.1: Equivalent circuit of a coil (adapted from [5])

Considering how coupling elements also assume the role of the antenna in data communication of inductively coupled RFID systems, the coil's equivalent circuit parameters are referred as antenna parameters. Values of these parameters strongly depend on the geometrical and material properties that are chosen for the antenna design. When it comes to determining the values of R_L , C_L and L , this can be done by evaluating the real and imaginary parts of the coil's equivalent impedance $\underline{Z}_{\text{COIL}}$ (eq. 4.1) at different frequencies using AC analysis. Another way is to use numerically approximated formulas of design parameters and to solve them using appropriate numerical computer software.

$$\underline{Z}_{\text{COIL}}(j\omega) = \frac{R_L + j\omega L}{1 - \omega^2 C_L L + j\omega R_L C_L} \quad (4.1)$$

This thesis uses existing values for R_L , C_L and L , determined previously by methods described in [3]. In addition, capacitance C_L is mostly neglected, as it is negligible compared to the values of other capacitances that are modeled into the equivalent circuits for PCD and PICC. Typical values of both PCD and PICC antenna parameters for proximity coupling systems are shown in table 4.1.

Table 4.1: Typical values for equivalent circuit parameters of reader and transponder coil (adapted from [5])

Antenna	L	R_L	C_L
PCD	300 nH	187 m Ω	≈ 0
PICC	2.26 μ H	2.4 Ω	5 pF

4.1.2 PCD

The equivalent circuit of a PCD for proximity coupling systems is essentially no different from a simple damped serial resonant circuit (chapter 3). Capacitance is primarily included in the circuit to allow resonance to be achieved (fig. 4.2).

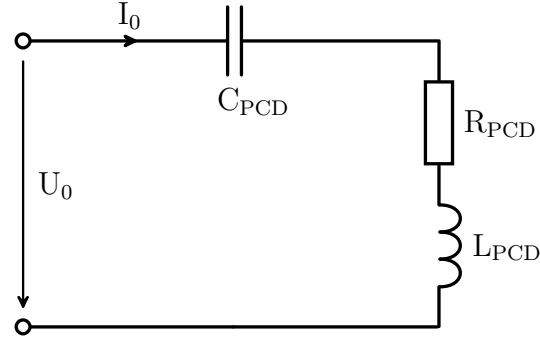


Figure 4.2: Basic equivalent circuit of a PCD (adapted from [5])

Common power supply of a PCD is a voltage source with an internal resistance (R_I) of $50\ \Omega$, so that impedance matching to minimize reflection losses is required before connecting the source to the coupling element. By introducing two capacitances, a serial (C_{MS}) and a parallel (C_{MP}) one, the PCD coil impedance is matched to the internal resistance of the source. This is referred to as *antenna matching* (fig. 4.3).

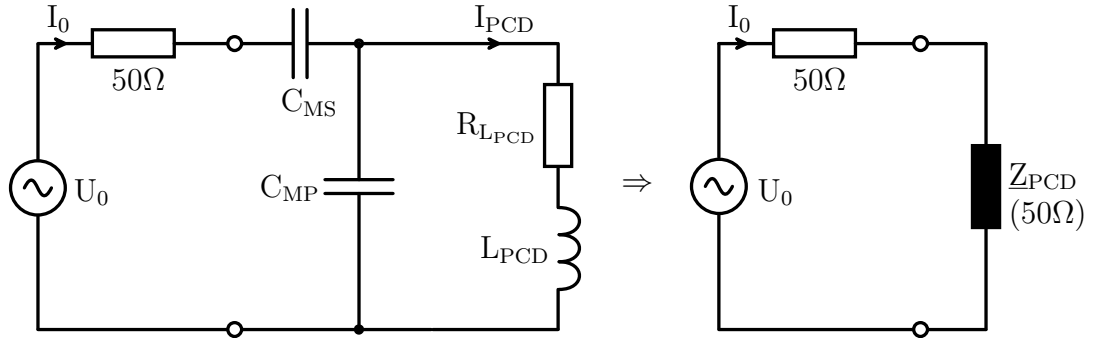


Figure 4.3: Equivalent circuit of a PCD including an antenna matching network (adapted from [5])

The equivalent network impedance $Z_{PCD}(j\omega)$ of the PCD is split into its real and imaginary parts, which are then set to be equal to R_I and zero, respectively.

$$Z_{PCD} = \Re\{Z_{PCD}\} + j\Im\{Z_{PCD}\}$$

$$\Re\{Z_{PCD}\} \stackrel{!}{=} R_I \text{ and } \Im\{Z_{PCD}\} \stackrel{!}{=} 0$$

Solving after these two conditions leads to the values for C_{MS} and C_{MP} .

$$C_{MP} = \frac{\omega R_I L_{PCD} - \sqrt{\omega^2 L_{PCD}^2 R_I R_{L_{PCD}} + R_I R_{L_{PCD}}^3 - R_I^2 R_{L_{PCD}}^2}}{\omega R_I (\omega^2 L_{PCD}^2 + R_{L_{PCD}}^2)} \quad (4.2)$$

$$C_{MS} = -\frac{\omega^4 C_{MP}^2 L_{PCD}^2 + \omega^2 C_{MP}^2 R_{L_{PCD}}^2 + 2\omega^2 C_{MP} L_{PCD} + 1}{\omega^4 C_{MP} L_{PCD}^2 + \omega^2 C_{MP} R_{L_{PCD}}^2 - \omega^2 L_{PCD}} \quad (4.3)$$

Considering the quality factor of the entire reader, it is mostly dependent on the quality factor of the reader's antenna. For the PCD antenna in the equivalent circuit from fig. 4.3 the Q-factor can be determined by eq. 3.26:

$$Q_{COIL} = \frac{\omega_{RES} L_{PCD}}{R_{L_{PCD}}}. \quad (4.4)$$

Performing measurements to find the Q-factor of an entire PCD and inserting the acquired results into eq. 3.27 shows that the Q-factor of the whole circuit approximately amounts to half the Q-factor of the circuit's antenna coil.

$$Q_{PCD} \approx \frac{Q_{COIL}}{2} \quad (4.5)$$

4.1.3 PICC

When it comes to transponders of proximity coupling systems, their typical components are a coupling element and an IC, colloquially also referred to as chip. The circuit model of a PICC therefore combines the equivalent circuits of a coil and of an IC, which results in a resonant circuit shown in fig. 4.4.

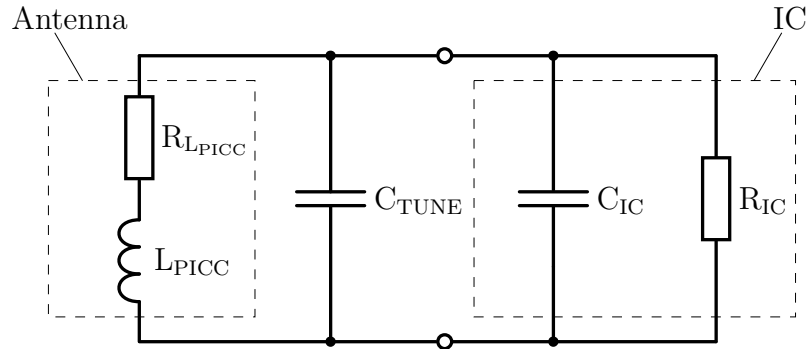


Figure 4.4: Equivalent circuit of a PICC (adapted from [5])

Modeling the IC, a highly complex semiconductor device, as merely a resistor in parallel with a capacitor is of course an oversimplification, although it is more

than justified for the level of abstraction used here. Resonance in the PICC is intentional, devised to maximize power transfer from the magnetic field of the PCD. However, the capacitance C_{IC} of the IC is fixed, meaning that it is not possible to vary C_{IC} to enable tuning of the resonance frequency. As a solution, a variable parallel capacitance C_{TUNE} is introduced to provide more freedom when specifying the resonance frequency.

Whenever the PICC finds itself within reach of the magnetic field originating from the PCD, a voltage is induced in the PICC coil via electromagnetic induction (chapter 3). This induced voltage U_{PICC} is modeled as an AC voltage source in the equivalent circuit (fig. 4.5).

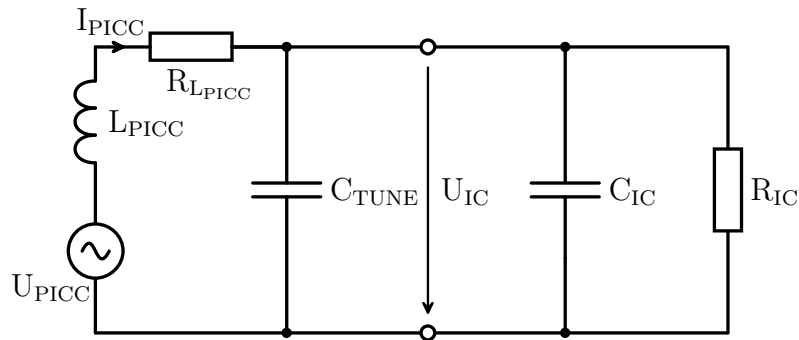


Figure 4.5: Equivalent circuit of a PICC with the induced voltage modeled as an AC source (adapted from [5])

Naturally, there are some important components of a transponder that are omitted in such an equivalent circuit model, one of them being the supply voltage U_{IC} of the IC. In a PICC, which is a passive transponder, voltage U_{IC} is rectified and smoothed using a low-loss bridge rectifier circuit (fig. 4.6) in order to power the IC, usually with a DC voltage of around 5 V for standard operation.

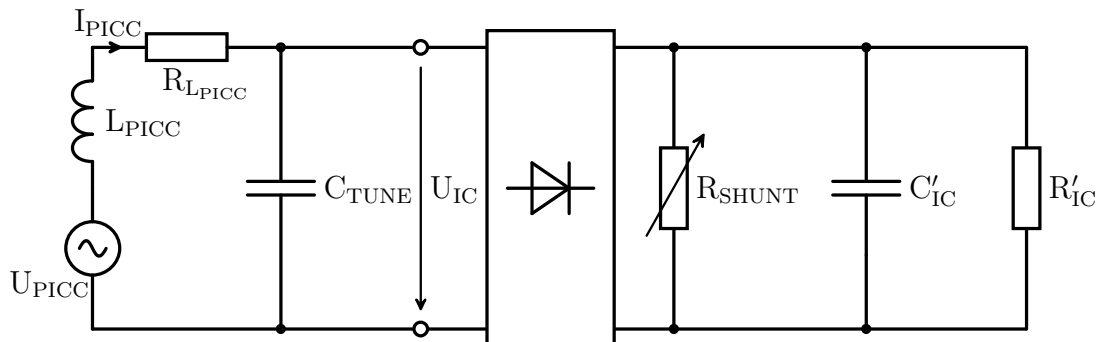


Figure 4.6: Equivalent circuit of a PICC including a rectifier and a shunt regulator (adapted from [5])

However, U_{IC} is prone to variation due to reasons such as resonance, variable distance between PCD and PICC, as well as changes in the resistance R_{IC} of the IC throughout different modes of operation. Some of these changes may cause U_{IC} to even reach values in hundreds of volts. For that reason, a shunt regulator is included in the PICC (fig. 4.6), which is modeled as a voltage-dependent resistor parallel to R_{IC} . A sudden tendency of U_{IC} to increase causes the shunt regulator to reduce the value of total parallel resistance, and with it the quality factor of the entire circuit, resulting in a stable and unchanged value of U_{IC} .

Considering how this thesis mainly focuses on the implications that resonance frequency has on the IC as a whole, it is sufficient to use a simplified equivalent circuit shown in fig. 5.1. The shunt regulator R_{SHUNT} is included in the resistance R_{IC} , so that R_{IC} represents power dissipation of the entire IC. On the other hand, capacitances C_{TUNE} and C_{IC} are combined in a single capacitance C , which shall be the only capacitance used in upcoming considerations of resonance frequency in the PICC.

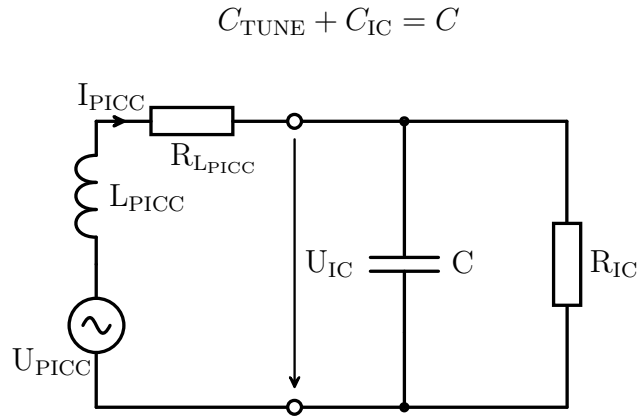


Figure 4.7: Simplified equivalent circuit of a PICC (adapted from [5])

As opposed to the PCD, quality factor of the simplified PICC equivalent circuit can rather easily be derived analytically:

$$Q_{PICC} = \frac{1}{R_{L_{PICC}} \sqrt{\frac{C}{L_{PICC}}} + \frac{1}{R_{IC}} \sqrt{\frac{L_{PICC}}{C}}} \quad (4.6)$$

4.1.4 Transformed Impedance \underline{Z}_T

Electromagnetic induction between the PCD and the PICC causes both devices to influence one another. Despite not having a voltage source of its own, the

PICC manages to affect the PCD with its magnetic field that tends to oppose the magnetic field of the PCD, as explained by Lenz's law (chapter 3). As a consequence, the weakened PCD field alters the current flow throughout the PCD, thereby also changing other electrical quantities: the PCD is said to be *loaded* by the PICC. This feedback of the PICC can actually be modeled with a single parameter, the so-called *transformed impedance* \underline{Z}_T (fig. 4.8) in the equivalent circuit of the PCD [1].

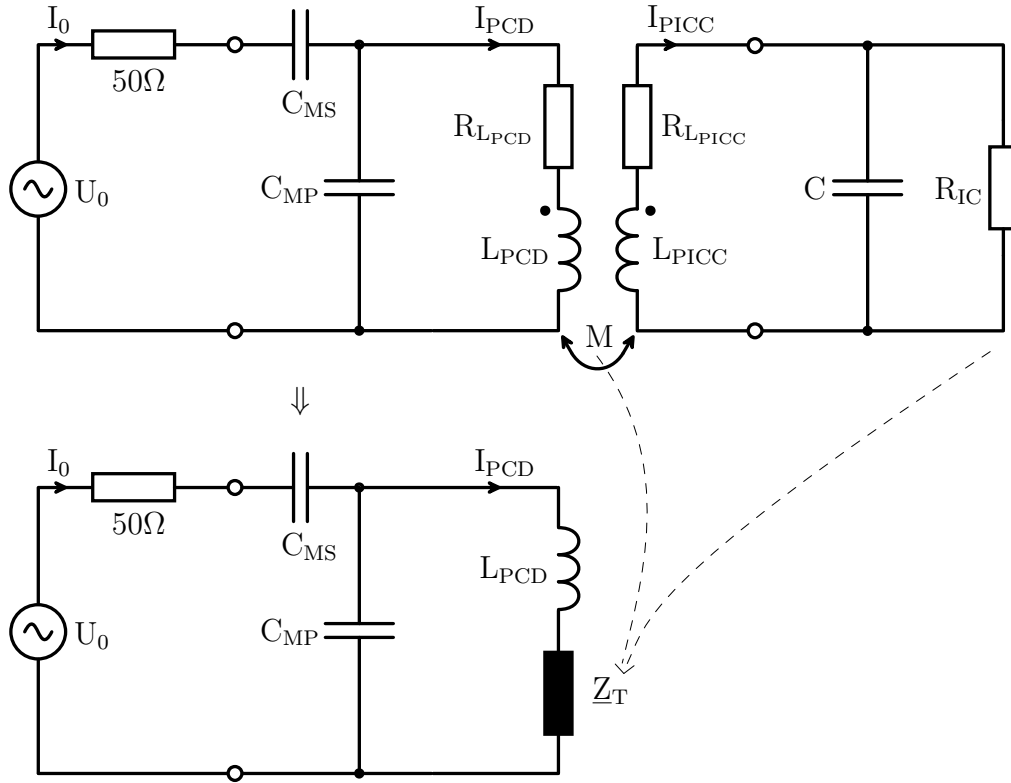


Figure 4.8: Equivalent circuit of a PCD including feedback of a PICC expressed through transformed impedance \underline{Z}_T (adapted from [5])

A mathematical expression for \underline{Z}_T is given by eq. 4.7, showing that it depends on the PICC circuit parameters, the inductance of the PCD, as well as on the distance between PCD and PICC, expressed by the coupling coefficient.

$$\underline{Z}_T = \frac{\omega^2 k^2 L_{\text{PCD}} L_{\text{PICC}}}{R_{L_{\text{PICC}}} + j\omega L_{\text{PICC}} + \frac{R_{\text{IC}}}{1 + j\omega R_{\text{IC}} C}} \quad (4.7)$$

If the distance between PCD and PICC is large enough that the coupling coefficient approaches zero, the transformed impedance disappears and the PCD

is said to be *unloaded*. Because magnetic field is undisturbed, power transfer and matching of the voltage source to the PCD antenna remain optimal in this state.

4.2 Data Communication

Communication principles with respect to coding and modulation techniques of proximity coupling systems are not regarded in detail in this thesis. However, after having presented the physics behind inductive coupling and introducing the PCD and PICC equivalent circuit models, it is at this point reasonable to briefly address the main principles of data communication between the PCD and the PICC.

4.2.1 Downlink

For proximity coupling systems, transfer of data from PCD to PICC is termed *downlink*, and it relies on manipulation of the PCD magnetic field in order to transmit the desired data. Speaking in communication engineering jargon, the PCD magnetic field assumes the role of a *carrier* signal, which is to further be *modulated*, i.e. changed in amplitude, frequency or phase in order to convey information. Digital modulation techniques utilized by the PCD are carried over to the PICC via the induced voltage. As a result, current in the PICC, which is proportional to the induced voltage, contains the information. Demodulation of the voltage or current allows the PICC to receive and interpret the data sent by the PCD.

In particular, the AC source in the PCD creates a sine voltage $u_0(t)$ (eq. 4.8) with a frequency of 13.56 MHz. Being proportional to $u_0(t)$, the magnetic field oscillates with the same frequency as well. Therefore, modulation of the magnetic field in amplitude, frequency or phase comes down to changing the corresponding parameter of $u_0(t)$.

$$u_0(t) = A(t) \sin(\omega_0 t + \varphi(t)) \quad (4.8)$$

Amplitude shift keying (ASK) is the most commonly used method of digital communication for proximity coupling systems. Some systems that make use of phase shift keying (PSK) also exist. However, frequency shift keying (FSK) is rarely applicable as a modulation scheme because the system relies on resonance by finely tuning the resonance frequency to match the one used by the PCD. Changing the frequency in order to send information would result in compromising the resonance and suffering power supply losses. Of course, ASK is also accompanied by a slight change in spectrum, which is acceptable.

4.2.2 Uplink

Data transfer from PICC to PCD, regarded as *uplink*, utilizes the already mentioned feedback that the PICC exerts upon the PCD by having the PICC appropriately change its electrical characteristics in order to be perceived as communication at the PCD end. This technique is called *load modulation*.

Change in the current flowing through the PICC is proportionate to the PICC magnetic field. Per Lenz's law, this change also has a direct consequence on the magnetic field of the PCD. Therefore, if the PICC current is to somehow be modulated, such modulation would be detected at the PCD as a variation in voltage or current due to the varied transformed impedance Z_T that represents the PICC. Load modulation changes the PICC current by introducing an electrical component into the circuit, for example a resistor or a capacitor, and having it switched on and off according to the transmitting data. In the PCD antenna, result is a variable voltage or current that contains information and is able to be demodulated in order to receive the data.

Depending on whether resistance R_{IC} or capacitance C is varied in the PICC circuit, there are two types of load modulation:

- *ohmic* load modulation
- *capacitive* load modulation.

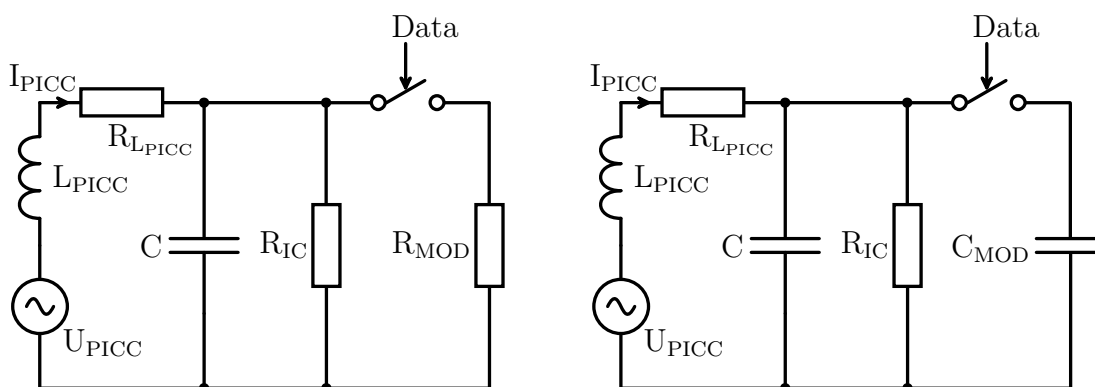


Figure 4.9: Load modulation: ohmic (left) and capacitive (right) (adapted from [5])

A look at fig. 4.9 shows a switch that connects a resistance R_{MOD} in parallel to the PICC resistance R_{IC} . Depending on the binary signal to be transmitted, the switch is either left open or closed. When closed, the resistance of the PICC changes because of the parallel R_{MOD} resulting in a change of the current I_{PICC} as well. If the transmitting data is represented by a binary stream, the current I_{PICC}

through the PICC changes accordingly. Considering how I_{PICC} is defined by the equivalent network impedance $\underline{Z}_{\text{PICC}}$, there are two states of $\underline{Z}_{\text{PICC}}$: *unmodulated* and *modulated*. Assigning symbols to the states is arbitrary, in this case an open switch is associated with a binary 0, while a closed switch corresponds to a binary 1.

Unmodulated:

$$\underline{I}_{\text{PICC},unmod} = \frac{\underline{U}_{\text{PICC}}}{\underline{Z}_{\text{PICC},unmod}}$$

$$\underline{Z}_{\text{PICC},unmod} = R_{\text{LPICC}} + j\omega L_{\text{PICC}} + \frac{R_{\text{IC}}}{1 + j\omega R_{\text{IC}}C}$$

Modulated:

$$\underline{I}_{\text{PICC},mod} = \frac{\underline{U}_{\text{PICC}}}{\underline{Z}_{\text{PICC},mod}}$$

$$\underline{Z}_{\text{PICC},mod} = R_{\text{LPICC}} + j\omega L_{\text{PICC}} + \frac{R_{\text{IC},mod}}{1 + j\omega R_{\text{IC},mod}C}$$

$$R_{\text{IC},mod} = \frac{R_{\text{IC}}R_{\text{MOD}}}{R_{\text{IC}} + R_{\text{MOD}}}$$

In order to gain more insight on load modulation, it is reasonable to more closely investigate how transformed impedance \underline{Z}_{T} affects the PCD electrical quantities while the PICC changes its own quantities. This can be achieved by deriving an expression for the current I_{PCD} as a function of \underline{Z}_{T} .

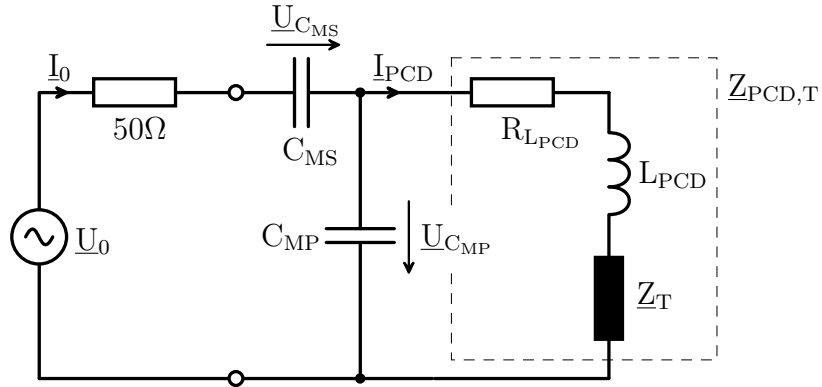


Figure 4.10: Equivalent circuit of a PCD (adapted from [5])

Assuming that regulatory resistances due to movement of the PICC inside the PCD magnetic field are neglected (shunt mechanism etc.), the transformed impedance \underline{Z}_{T} alternates between two states: unmodulated and modulated.

$$\text{Unmodulated:} \quad \underline{Z}_{T,unmod} = \frac{\omega^2 k^2 L_{PCD} L_{PICC}}{R_{L_{PICC}} + j\omega L_{PICC} + \frac{R_{IC}}{1 + j\omega R_{IC} C}}$$

$$\text{Modulated:} \quad \underline{Z}_{T,mod} = \frac{\omega^2 k^2 L_{PCD} L_{PICC}}{R_{L_{PICC}} + j\omega L_{PICC} + \frac{R_{IC,mod}}{1 + j\omega R_{IC,mod} C}}$$

$$R_{IC,mod} = \frac{R_{IC} R_{MOD}}{R_{IC} + R_{MOD}}$$

Admittance \underline{Y}'_{PCD} connects the PCD voltage source \underline{U}_0 with the current \underline{I}_{PCD} that defines the magnetic field in the PCD antenna. Deriving a mathematical expression for \underline{Y}'_{PCD} confirms that it is a function of \underline{Z}_T (eq. 4.9). Thus, \underline{Y}'_{PCD} also switches between unmodulated and modulated state, reacting in accordance with the uplink data transfer.

$$\begin{aligned} \underline{Z}_{PCD,T} &= R_{L_{PCD}} + j\omega L_{PCD} + \underline{Z}_T \\ \underline{I}_{PCD} &= \frac{\underline{U}_{CMP}}{\underline{Z}_{PCD,T}} = \underline{Y}_{PCD,T} (\underline{U}_0 - \underline{U}_{R_I} - \underline{U}_{C_{MS}}) = \\ &= \underline{Y}_{PCD,T} \left(\underline{U}_0 - \underline{I}_0 R_I - \underline{I}_0 \frac{1}{j\omega C_{MS}} \right) = \\ &= \underline{Y}_{PCD,T} \left(\underline{U}_0 - \underline{I}_0 \left(R_I + \frac{1}{j\omega C_{MS}} \right) \right) = \\ &= \underline{Y}_{PCD,T} \left(\underline{U}_0 - \underline{Y}_{PCD} \underline{U}_0 \left(R_I + \frac{1}{j\omega C_{MS}} \right) \right) = \\ &= \underbrace{\underline{Y}_{PCD,T} \left(1 - \underline{Y}_{PCD} \left(R_I + \frac{1}{j\omega C_{MS}} \right) \right)}_{\underline{Y}'_{PCD}} \underline{U}_0 \\ &\Rightarrow \underline{Y}'_{PCD} = f(\underline{Z}_T) \end{aligned} \tag{4.9}$$

A look at the expression for \underline{I}_{PCD} and its separate amplitude and phase components (eq. 4.10) shows that change in \underline{Z}_T has an impact not only on the amplitude of \underline{I}_{PCD} , but on the phase as well. In that sense, load modulation can be considered as a combination of amplitude shift keying and phase shift keying. Variations of both amplitude and phase are detectable in the PCD and possible to demodulate in order for PCD to receive the data.

$$\begin{aligned} \underline{I}_{\text{PCD}} &= |\underline{Y}'_{\text{PCD}}| e^{j\varphi'_{\text{PCD}}} |\underline{U}_0| e^{j(\omega_0 t + \varphi_0)} = \\ &= |\underline{Y}'_{\text{PCD}}| |\underline{U}_0| e^{j(\varphi'_{\text{PCD}} + \varphi_0)} e^{j\omega_0 t} \end{aligned} \quad (4.10)$$

4.3 ISO Test PCD Assembly

This section is intended to describe the standardized definitions and test methods for proximity coupling systems. These are provided by ISO (the International Organization for Standardization) and IEC (the International Electrotechnical Commission) in the form of ISO/IEC 14443 and ISO/IEC 10373-6 standards.

ISO/IEC 14443 is a standard divided in four parts that define the physical characteristics, radio frequency power, signal interface, initialization, anticollision and transmission protocol of contactless integrated circuit proximity identification cards.

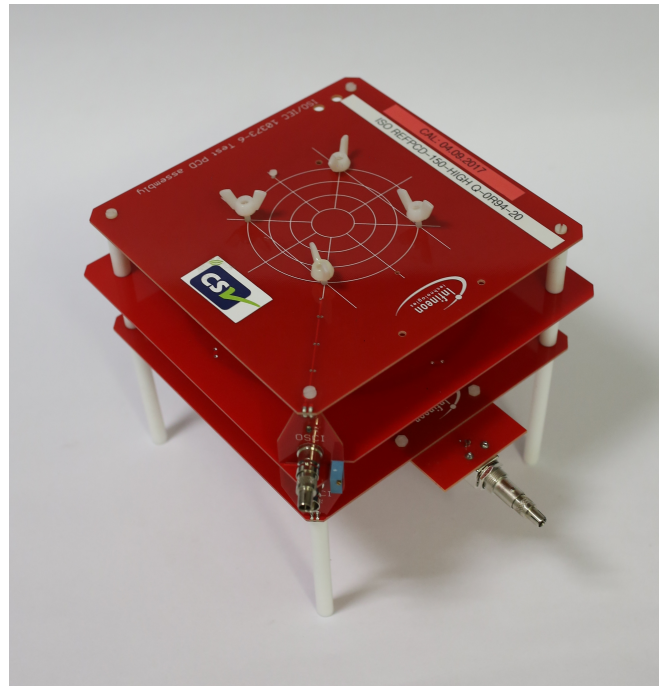


Figure 4.11: ISO test PCD assembly (courtesy of Infineon Technologies Austria AG)

ISO/IEC 10373-6, on the other hand, describes the various test methods for proximity identification cards where each method is cross-referenced to one or more base standards. Many test methods introduced in ISO/IEC 10373-6 are

performed with the *ISO test PCD assembly* (fig. 4.11), an important component in the test apparatus for verifying both PCD and PICC operation.

Considering how this thesis strongly focuses on the ISO test PCD assembly and the measurement setup built around it, it is important to understand the structure, functionality and circuit model of this setup.

4.3.1 Structure

Cross section of the ISO test PCD assembly is depicted in fig. 4.12. Essentially, it is a three-stage tower where the middle stage assumes the role of a PCD antenna coil that generates the magnetic field, and also includes an impedance matching network (capacitances C_{MS} and C_{MP}) that matches the PCD antenna to the voltage source at 13.56 MHz. The upper and lower stages, called *sense coils*, are identical in terms of size and number of windings, and are positioned at equal distances above and below the PCD antenna coil.

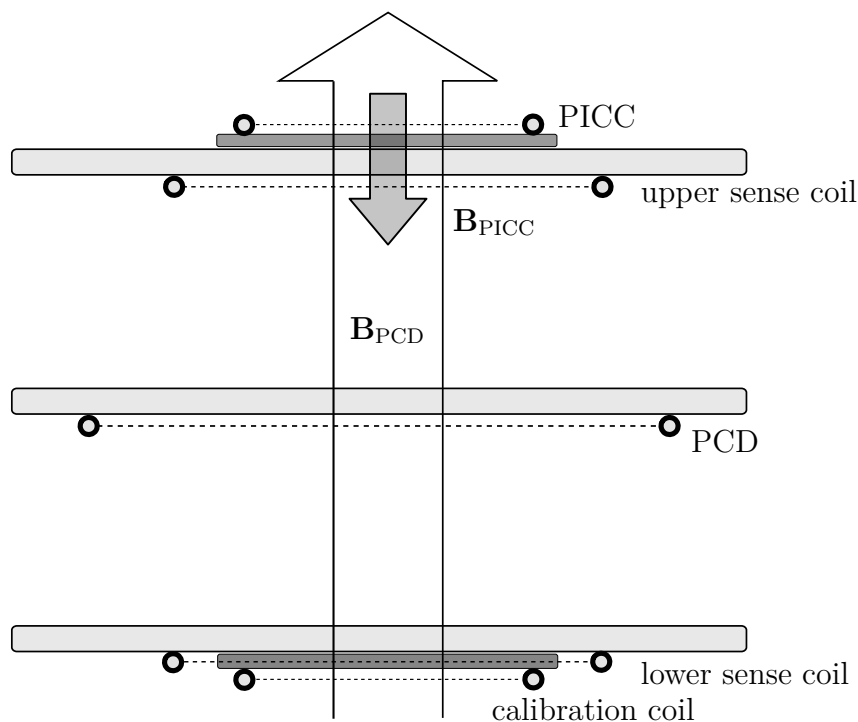


Figure 4.12: Cross section of ISO test PCD assembly (adapted from [6])

The main principle of ISO test PCD assembly is that the PCD antenna creates a magnetic field, expressed by magnetic flux density \mathbf{B}_{PCD} , that passes through both the upper and the lower sense coil, thereby inducing the same voltage level in both coils due to symmetrical structure. The sense coils interact with the

PCD only via mutual inductance, although they are connected to one another by the so-called *measuring bridge* (fig. 4.13). This bridge is constructed in a way that the induced voltages have opposite phase, and where a differential voltage is introduced across the bridge, representing a subtraction of the sense coil voltages. With no PICC present, the differential voltage is hence equal to zero. When a PICC is placed on the upper sense coil, it generates its own magnetic flux \mathbf{B}_{PICC} that counteracts its origin, as per Lenz's law. Result is a reduction of \mathbf{B}_{PCD} perceived by the upper sense coil, the PICC is said to *load* the ISO test PCD assembly. Because of a much larger distance to the lower sense coil, coupling between PICC and lower sense coil can be considered negligible. Thus, there is no reduction of \mathbf{B}_{PCD} in the lower sense coil. The differential voltage at the measuring bridge is no longer zero, because it shows only the influence of the PICC, as the effect of the PCD is eliminated through the subtraction.

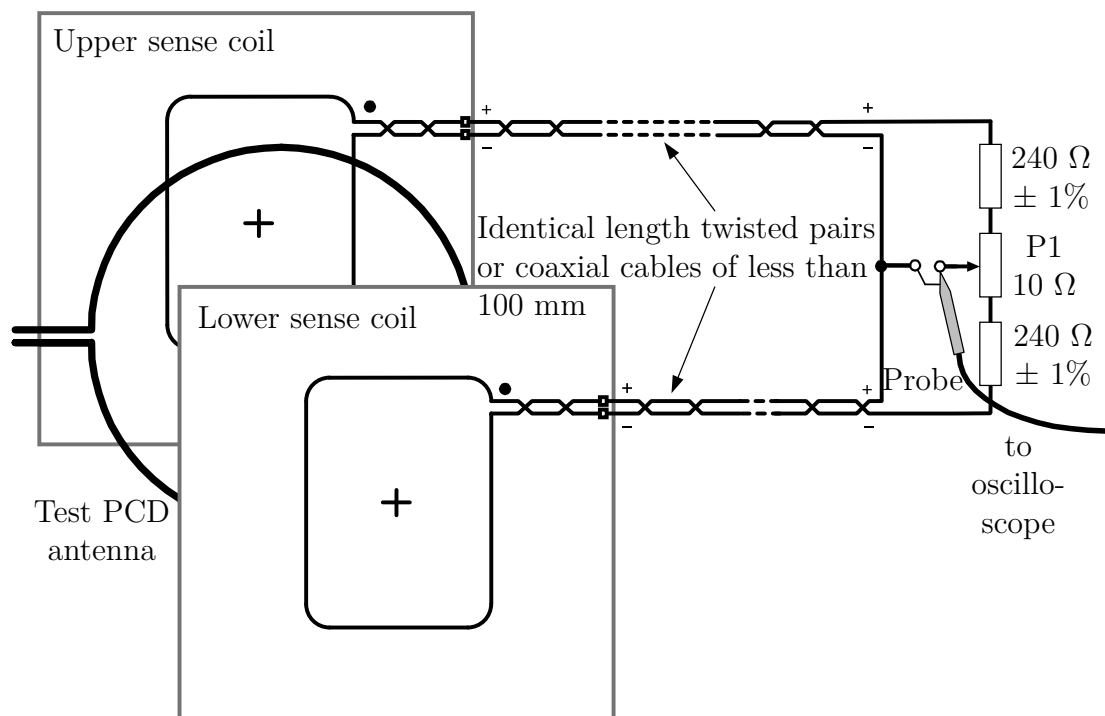


Figure 4.13: Measuring bridge of ISO test PCD assembly (adapted from [7])

In addition, another coil, called *calibration coil*, is placed directly below the lower sense coil. The calibration coil is designed to have the same distance from the PCD and layout (ID-1 format) as the PICC, therefore being coupled to the lower sense coil with the same coupling coefficient as the PICC is coupled to the upper sense coil. Due to such symmetry, one is able to know the magnetic field induced in the PICC by measuring the voltage at the calibration coil and

converting it to magnetic field strength. That way, there is no need for any additional measuring coils near the PICC that would introduce further loading with their own mutual inductance.

Ultimately, the two output signals of the ISO test PCD assembly are the calibration coil voltage, denoted by U_{CC} and the sense coil differential voltage, denoted by U_{SC} . The former describes the PCD magnetic field as “seen” by the PICC, while the latter shows the magnetic field created by PICC itself, i.e. the uplink communication. Both U_{CC} and U_{SC} can be measured using oscilloscope probes, provided they are high impedance RF-probes with a low internal capacitance (lower than 14 pF).

4.3.2 Circuit Model

Before presenting an equivalent circuit model of the entire ISO test PCD assembly, a closer look shall be taken at the circuit model of the measuring bridge (fig. 4.14). In this model, the induced sense coil voltages $U_{IND,up}$ and $U_{IND,down}$ are explicitly included as AC voltage sources. As previously mentioned, $U_{IND,up}$ and $U_{IND,down}$ should be equal, as long as there is no PICC present at the upper sense coil. The voltage that represents the difference of both sense coils is denoted by U_{SC} . This voltage is measurable with an oscilloscope probe, which has its internal impedance modeled as resistance R_{PR} parallel to capacitance C_{PR} . In construction of the ISO test PCD assembly, it is ideally aimed for equal inductance values for $L_{SC,up}$ and $L_{SC,down}$, as well as for the values of the coupling coefficient from PCD coil to both sense coils. However, this is difficult to achieve in practice because there are always some fabrication-dependent variations. Furthermore, perfect symmetry of the three stages in the assembly cannot be achieved, resulting in slightly different coupling coefficients. As a consequence, there is always a small voltage value, called error voltage, that is measured for U_{SC} when there is no PICC present. A variable resistance R_{POT} is included in the bridge with a purpose to minimize the error voltage.

Coupling via mutual induction between sense coils and both PCD and PICC are represented by the induced voltages $U_{IND,up}$ and $U_{IND,down}$. Therefore, these voltages contain magnetic flux components coming separately from the PCD and the PICC, which can mathematically be expressed with separate mutual inductances (eq. 4.11 and 4.12). The negative sign in both equations is attributed to Lenz’s law.

$$\underline{U}_{IND,up} = j\omega M_{PCD \leftrightarrow SC,up} \underline{I}_{PCD} - j\omega M_{PICC \leftrightarrow SC,up} \underline{I}_{PICC} \quad (4.11)$$

$$\underline{U}_{IND,down} = j\omega M_{PCD \leftrightarrow SC,down} \underline{I}_{PCD} - j\omega M_{PICC \leftrightarrow SC,down} \underline{I}_{PICC} \quad (4.12)$$

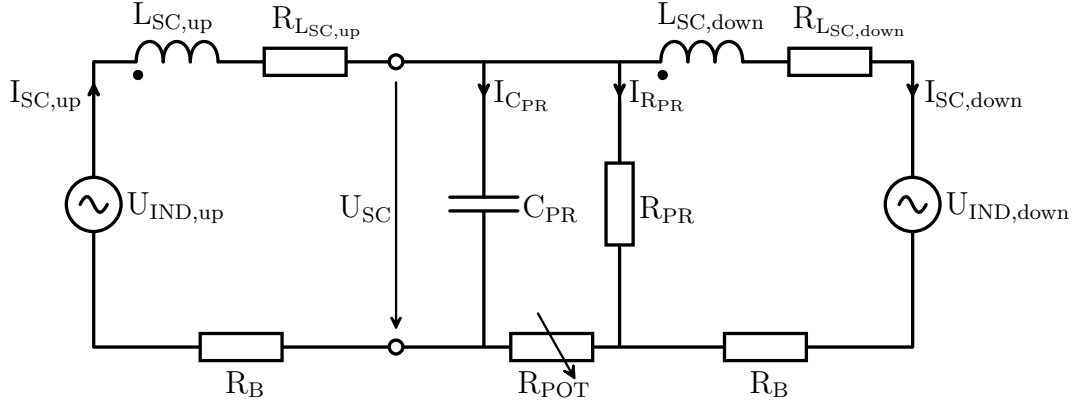


Figure 4.14: Equivalent circuit model of the measuring bridge (adapted from [6])

In an ideal case, the mutual inductance between PICC and upper sense coil $M_{\text{PICC} \leftrightarrow \text{SC,up}}$ should be maximized, whereas the one between PICC and lower sense coil $M_{\text{PICC} \leftrightarrow \text{SC,down}}$ should be equal to zero. This is not the case in practice, as there is rather weak coupling that exists between the PICC and the lower sense coil. However, for the circuit modeling purposes in this thesis, $M_{\text{PICC} \leftrightarrow \text{SC,down}}$ is neglected because of a considerably lower value when compared to $M_{\text{PICC} \leftrightarrow \text{SC,down}}$.

$$M_{\text{PICC} \leftrightarrow \text{SC,up}} \gg M_{\text{PICC} \leftrightarrow \text{SC,down}} \quad (4.13)$$

$$\Rightarrow M_{\text{PICC} \leftrightarrow \text{SC,down}} \approx 0 \quad (4.14)$$

Later in this thesis it shall be required to express only the voltage induced by the PICC in the upper sense coil. This can easily be done by subtracting $\underline{U}_{\text{SC,down}}$ from $\underline{U}_{\text{SC,up}}$ (eq. 4.15), assuming an ideal case where mutual inductances between PCD and both sense coils are equal (eq. 4.16).

$$M_{\text{PCD} \leftrightarrow \text{SC,up}} = M_{\text{PCD} \leftrightarrow \text{SC,down}} \quad (4.15)$$

$$\underline{U}_{\text{IND,picc}} = \underline{U}_{\text{IND,up}} - \underline{U}_{\text{IND,down}} = -j\omega M_{\text{PICC} \leftrightarrow \text{SC,up}} \underline{I}_{\text{PICC}} \quad (4.16)$$

The entire ISO test PCD assembly equivalent circuit model is shown in fig. 4.15. The only mutual inductance shown explicitly is the one between PCD and PICC. However, the circuit model presented in this thesis takes multiple mutual inductances into consideration, while also omitting some for simplifying reasons, such as $M_{\text{PICC} \leftrightarrow \text{SC,down}}$. Table 4.2 summarizes all mutual inductances that are contained in the circuit model.

Table 4.2: Mutual inductances considered by the ISO test PCD assembly circuit model

Coupling	Symbol
PCD with PICC	$M_{\text{PCD} \leftrightarrow \text{PICC}}$
PCD with SC,up	$M_{\text{PCD} \leftrightarrow \text{SC,up}}$
PCD with SC,down	$M_{\text{PCD} \leftrightarrow \text{SC,down}}$
PCD with CC	$M_{\text{PCD} \leftrightarrow \text{CC}}$
PICC with SC,up	$M_{\text{PICC} \leftrightarrow \text{SC,up}}$

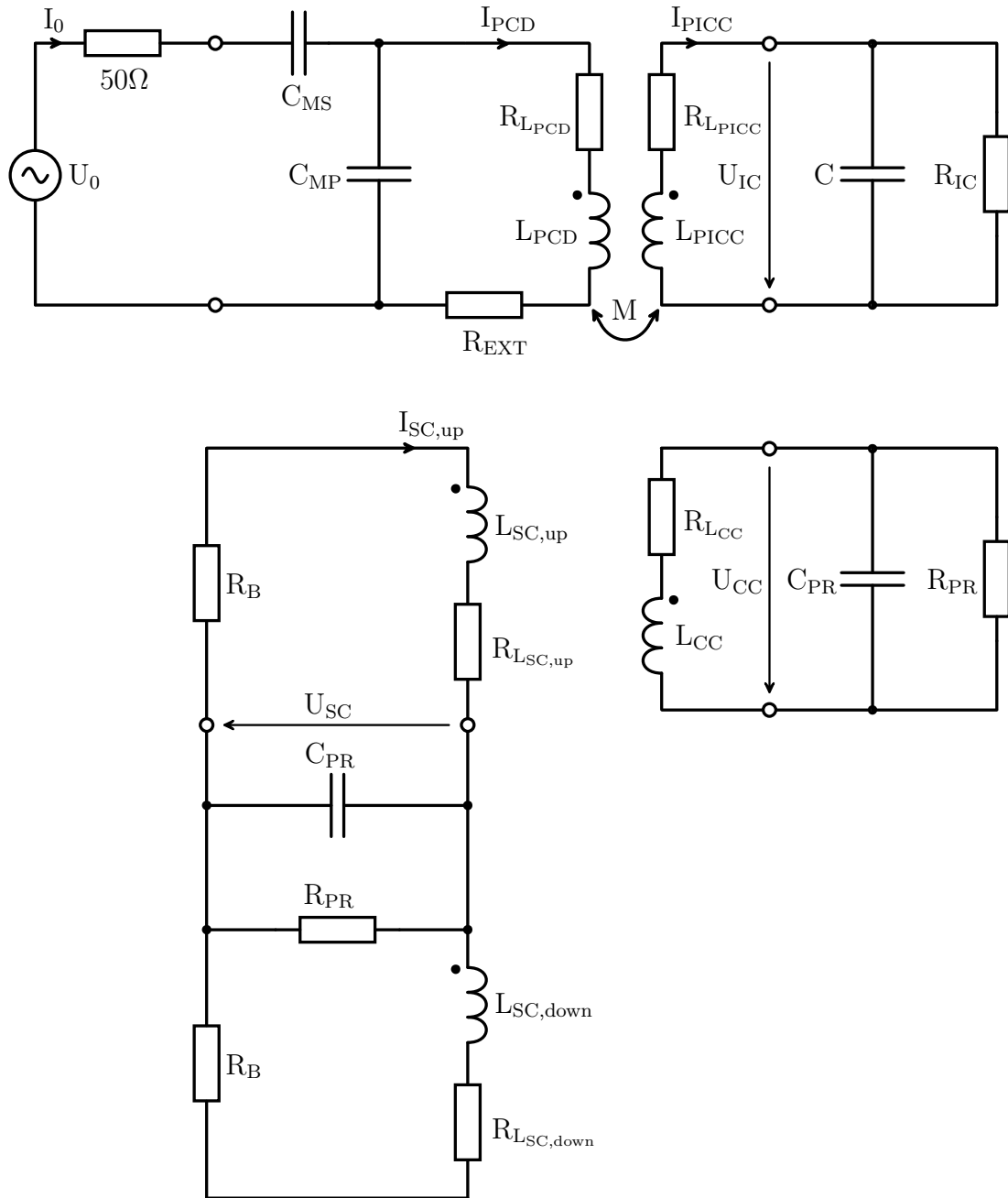


Figure 4.15: Equivalent circuit model of ISO test PCD assembly, including a PICC placed on the upper sense coil

4.3.3 Calculation of Magnetic Field Strength H

Calibration of the ISO test PCD assembly is required as a first step of any measurement process used for verification. During calibration, power of input signal to the assembly is correlated to a value of magnetic field strength that acts upon both sense coils. The calibration coil is designed to imitate the PICC in terms of geometry and coupling, allowing the magnetic field strength H determined at the calibration coil to be considered equal to the field strength that passes through the PICC. Voltage U_{CC} , measured at the calibration coil, provides the needed information about H in the PICC, which is especially important for a successful calibration of the assembly. However, in order for H to be obtained from U_{CC} , a certain conversion factor is needed. The purpose of this section is to derive this conversion factor based on a known calibration coil geometry.

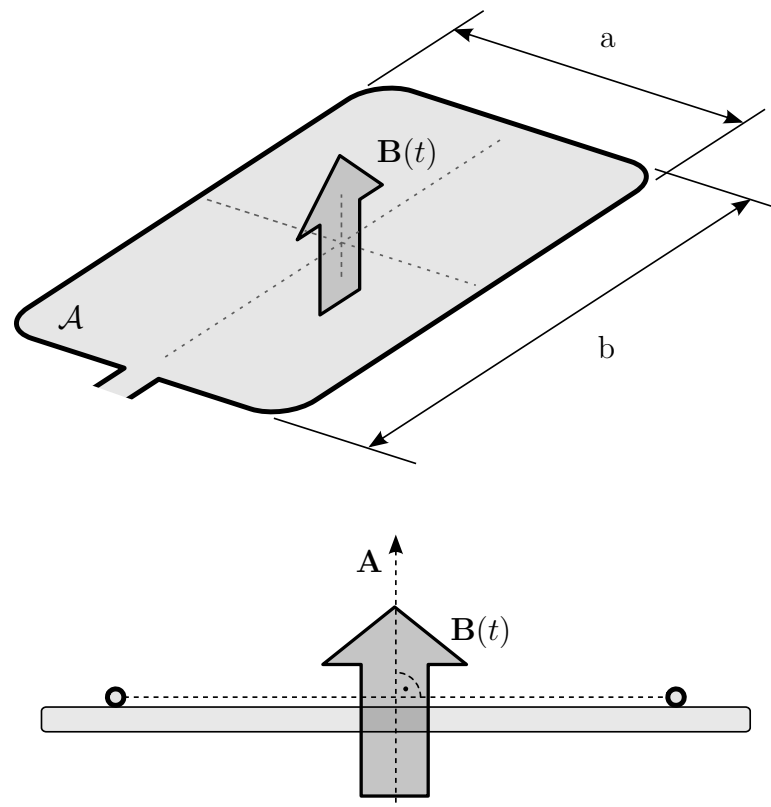


Figure 4.16: Calibration coil geometry used for calculating the conversion factor between U_{CC} and H (adapted from [6])

Fig. 4.16 shows a calibration coil arrangement with a magnetic field $\mathbf{B}(t)$ acting upon it. Following conditions are thereby presumed:

- Surface area \mathcal{A} is flat
- $\mathbf{B}(t)$ is homogeneous over the entire surface \mathcal{A} and proportional to:

$$\mathbf{B}(t) \sim B \cos(\omega t)$$

- $\mathbf{B}(t)$ is perpendicular to surface \mathcal{A} , and therefore to the area A of the calibration coil:

$$\alpha = \angle(\mathbf{A}, \mathbf{B}) = 0$$

Starting from the general expressions (chapter 3) for induced voltage $u_{ind}(t)$ and magnetic flux $\Phi(t)$:

$$\begin{aligned} u_{ind}(t) &= -N \frac{d\Phi(t)}{dt} & (4.17) \\ \Phi(t) &= \int_{\mathcal{A}} \mathbf{B}(t) \cdot d\mathbf{A} \\ \Phi(t) &= \int_{\mathcal{A}} B(t) dA \cos(\alpha) \end{aligned}$$

and applying the aforementioned conditions allows the expression for $\Phi(t)$ to be written as:

$$\begin{aligned} \Phi(t) &= BA \cos(\omega t) \\ &= \mu_0 H A \cos(\omega t) \end{aligned}$$

Relationship between \mathbf{B} and \mathbf{H} (chapter 3) is familiar as well:

$$\mathbf{B} = \mu_0 \mu_r \mathbf{H}$$

For simplifying reasons, area A is defined as:

$$A = ab [\text{m}^2]$$

Vector \mathbf{A} is pointing in direction of \mathbf{n} , which is the normal vector of area A :

$$\mathbf{A} = \mathbf{n} \cdot A$$

Thus, evaluating eq. 4.17 leads to the following expression for $u_{ind}(t)$:

$$u_{ind}(t) = \underbrace{\mu_0 N A \omega H}_{U_{ind}} \sin(\omega t)$$

The root mean square voltage U_{RMS} , measured at the calibration coil, differs from amplitude U_{ind} in a factor of $\frac{1}{\sqrt{2}}$, and is hence related to H_{RMS} by:

$$\begin{aligned} U_{\text{RMS}} &= \frac{1}{\sqrt{2}} U_{\text{ind}} \\ &= \mu_0 N A \omega H_{\text{RMS}} \end{aligned}$$

Expression for H_{RMS} can be obtained after rearranging:

$$\begin{aligned} H_{\text{RMS}} &= \frac{1}{\underbrace{\mu_0 N A \omega}_{k_{\text{RMS}}}} U_{\text{RMS}} \\ &= k_{\text{RMS}} U_{\text{RMS}} \end{aligned}$$

Usually it is the peak-to-peak voltage U_{PP} that is measured with an oscilloscope:

$$U_{\text{PP}} = \max(u_{\text{ind}}(t)) - \min(u_{\text{ind}}(t)) = 2U_{\text{ind}}$$

This allows H_{RMS} to be calculated from U_{PP} by the following relationship:

$$\begin{aligned} H_{\text{RMS}} &= \frac{1}{\mu_0 N A \omega} \cdot \frac{U_{\text{PP}}}{2\sqrt{2}} \\ &= \frac{1}{\underbrace{2\sqrt{2}\mu_0 N A \omega}_{k_{\text{PP}}}} U_{\text{PP}} \\ &= k_{\text{PP}} U_{\text{PP}} \end{aligned}$$

where k_{PP} is the desired conversion factor.

Table 4.3: Calibration coil parameters used in calculations of k_{RMS} and k_{PP}

a	b	ω	μ_0	N
(cm)	(cm)	(MHz)	($\text{VsA}^{-1}\text{m}^{-1}$)	
4.2	7.2	$2\pi \cdot 13.56$	$4\pi \cdot 10^{-7}$	1

Based on calibration coil parameters from table 4.3, the calculated values for k_{RMS} and k_{PP} are given in eq. 4.18 and 4.19, respectively.

$$k_{\text{RMS}} = \frac{1}{(4\pi \cdot 10^{-7}) \cdot 1 \cdot 0.042 \cdot 0.072 \cdot (2\pi \cdot 13.56 \cdot 10^6)} = 3.089 \text{ Am}^{-1}\text{V}^{-1} \quad (4.18)$$

$$k_{\text{PP}} = \frac{1}{2\sqrt{2}(4\pi \cdot 10^{-7}) \cdot 1 \cdot 0.042 \cdot 0.072 \cdot (2\pi \cdot 13.56 \cdot 10^6)} = 1.092 \text{ Am}^{-1}\text{V}^{-1} \quad (4.19)$$

Therefore, the number value of magnetic field strength H can be obtained from the peak-to-peak voltage measured at the calibration coil approximately as:

$$H_{\text{RMS}} \approx 1.1 \cdot U_{\text{PP}}$$

4.3.4 ISO Measurement Setup

Following the introduction of its important components, the entire measurement setup for verification and analysis of proximity coupling systems shall now be briefly presented. Fig. 4.17 shows a block diagram of a possible measurement apparatus used for the test methods defined in ISO/IEC 10373-6, whereas fig. 4.18 shows an actual setup, as used in a verification laboratory.

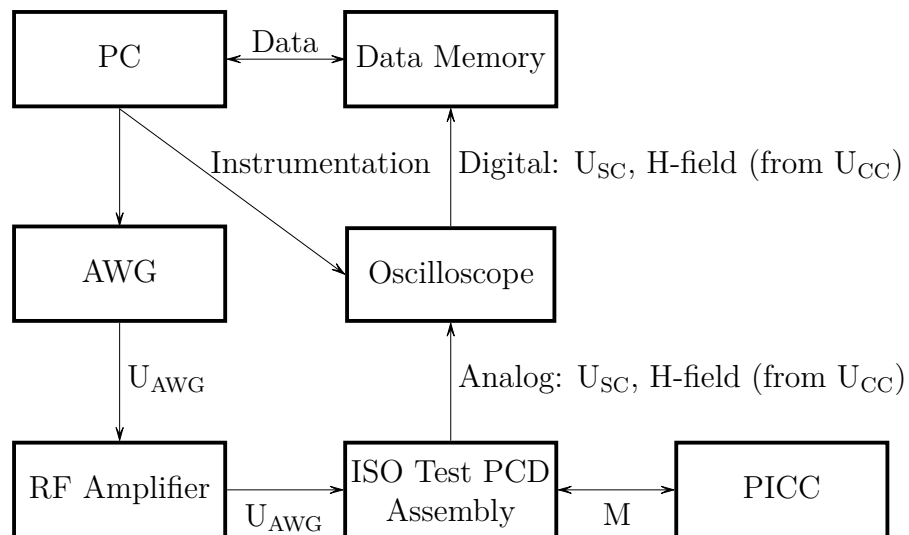


Figure 4.17: The entire measurement setup used for verification of proximity coupling systems (adapted from [6])

Essentially, the input signal is created by an arbitrary waveform generator (AWG) controlled by a PC. The shape and function of the waveform depend on the desired test case in the verification plan. Considering how an AWG does not usually provide an input voltage high enough to sustain the attenuation of the assembly due to geometry and other factors, the AWG signal is first passed through an RF amplifier before it is connected to the assembly.

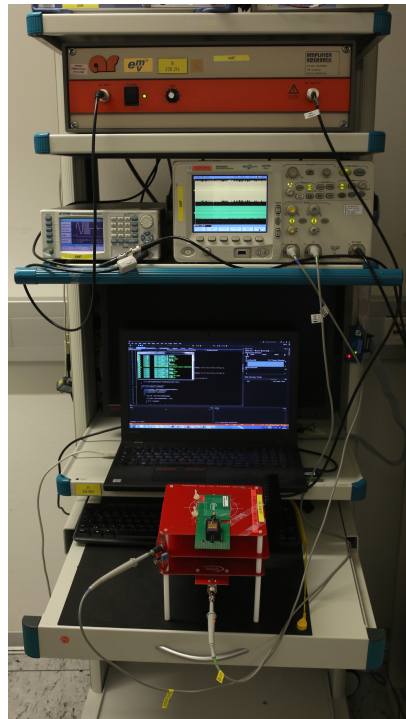


Figure 4.18: ISO measurement setup (courtesy of Infineon Technologies Austria AG)

Thanks to the amplifier, the PICC that is placed on the upper sense coil can feel a magnetic field strength in the range from 1 up to 15 A/m. As mentioned previously, there are two outputs of the system: the calibration coil voltage U_{CC} and the sense coil differential voltage U_{SC} . Both voltages are measured using oscilloscope probes, which are also included in the equivalent circuit model of the assembly (fig. 4.15). After being acquired by the oscilloscope, the now digital output signals are stored in memory and can be further processed by the PC in order to produce results of the particular verification test case.

This thesis focuses on the measurement setup shown in fig. 4.17, with a strong emphasis on the ISO test PCD assembly. With a deeper understanding about the system in question, it is now possible to move on to the main topic of the thesis, which is measuring the resonance frequency of PICCs.

Chapter 5

The Vector Network Analyzer Measurement Method

The proximity coupling systems described in this thesis utilize the principle of inductive coupling, which in turn relies on mutual induction of resonant circuits. This means that information about the resonance frequency at which these systems operate is of great importance. It is often required to measure the resonance frequency of contactless chip cards, for which the typical measurement method of today is performed on a vector network analyzer (VNA), and shall therefore be referred to as the *VNA method*. This chapter elaborates on this method by initially deriving different definitions of resonance frequency analytically, followed by describing the network analyzer measurement setup and its main disadvantages. It shall be seen that there is need for a new method that would outperform the network analyzer method in precision, reproducibility, and interoperability with other standardized test setups.

5.1 Definition of Resonance Frequency

There was already some word on the ambiguity that comes with defining resonance frequency in general (chapter 3), where it was explained that the different definitions are not mutually exclusive and that they are chosen based on the desired function of the system at hand. Here, the familiar equivalent circuit of a PICC (fig. 5.1) shall be used to exemplify the different definitions of resonance frequency for proximity coupling systems. For PICCs, and especially important for IC manufacturers, the goal is to maximize the voltage U_{IC} . However, the setback of this definition is that U_{IC} is not directly measurable. Contactless measurement of resonance frequency is therefore usually performed on a vector

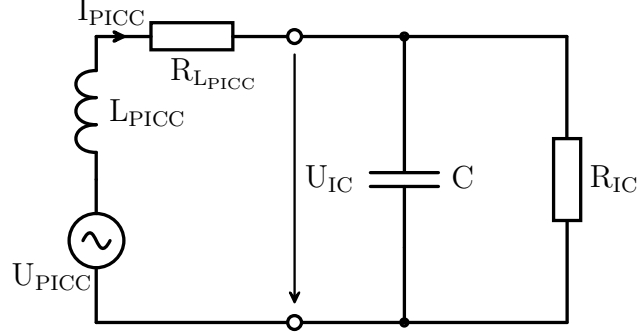


Figure 5.1: PICC equivalent circuit used for definition of resonance frequency

network analyzer, resulting in yet another definition of ω_{RES} .

Before any discussion of the measurement method and its setup, an analytical interpretation of the different ω_{RES} definitions is required. In this section, three such definitions shall be presented: the phase resonance ($\omega_{\text{RES},ph}$), the resonance at maximum U_{IC} ($\omega_{\text{RES},U_{\text{IC}}}$), and the resonance determined by maximum real part of the measured impedance, which is the definition used by the VNA method ($\omega_{\text{RES},\text{VNA}}$).

5.1.1 Phase Resonance

The most common resonance condition is the phase resonance, which occurs when impedance of the treated system is purely resistive. For the circuit in fig. 5.1, before resonance frequency $\omega_{\text{RES},ph}$ can be determined, it is first required to formulate an expression for the equivalent network impedance of the entire PICC:

$$\underline{Z}_{\text{PICC}} = R_{L_{\text{PICC}}} + j\omega L_{\text{PICC}} + \underline{Z}_{\text{IC}}$$

The integrated circuit impedance $\underline{Z}_{\text{IC}}$ is modeled as a parallel connection of C and R_{IC} :

$$\underline{Z}_{\text{IC}} = \frac{R_{\text{IC}}}{1 + j\omega R_{\text{IC}}C}$$

The expression for $\underline{Z}_{\text{PICC}}$ thus becomes:

$$\underline{Z}_{\text{PICC}} = R_{L_{\text{PICC}}} + j\omega L_{\text{PICC}} + \frac{R_{\text{IC}}}{1 + j\omega R_{\text{IC}}C}$$

Setting the condition that imaginary part of impedance $\underline{Z}_{\text{PICC}}$ must be equal to zero ultimately leads to the following expression for $\omega_{\text{RES},ph}$:

$$\Im\{\underline{Z}_{\text{PICC}}\} \stackrel{!}{=} 0 \Rightarrow \omega_{\text{RES},ph} = \sqrt{\frac{1}{L_{\text{PICC}}C} - \frac{1}{C^2 R_{\text{IC}}^2}} \quad (5.1)$$

5.1 Definition of Resonance Frequency

A notable difference between ohmic and capacitive load modulation concerns the influence of the chosen modulation scheme on the resonance frequency. Provided R_{IC} is high enough, a change in this resistance results in an almost negligible variation of f_{RES} , whereas changing the capacitance C always leads to a considerable change of f_{RES} . If phase resonance is assumed, the transformed impedance \underline{Z}_T is real at $\omega_{RES,ph}$ because it represents the PICC, which now has only the resistive part of its impedance. In this special case, applying ohmic load modulation affects only the amplitude of the PCD field, acting as pure amplitude shift keying, although this is not generally the case. A closer look at eq. 5.1 leads to the conclusion that as long as the resistance R_{IC} is high enough, the term $\frac{1}{C^2 R_{IC}^2}$ is negligible and $\omega_{RES,ph}$ reduces to the Thomson equation (eq. 3.21). However, the PICC may alter the value of R_{IC} because of the shunt regulator, or in order to perform load modulation, which can lead to lower values of R_{IC} and result in detuning from the desired operating frequency. An example of how resonance frequency behaves with respect to R_{IC} for a PICC tuned to 13.56 MHz is shown in fig. 5.2.

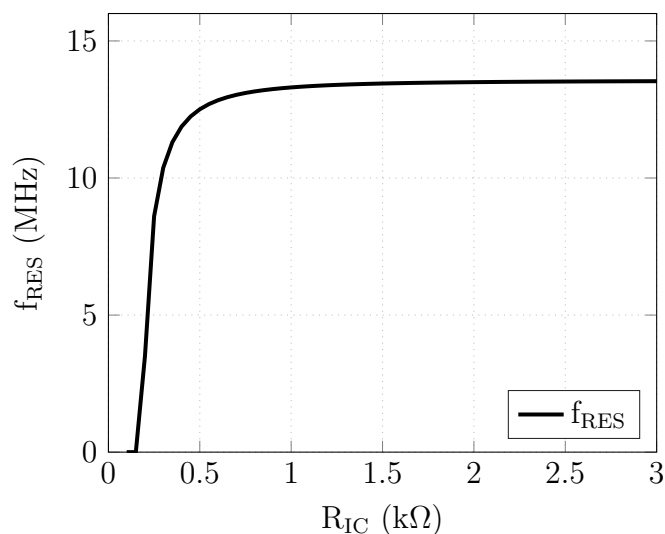


Figure 5.2: Resonance frequency of a PICC as a function of R_{IC}

Detuning means that the PICC is no longer in phase resonance, i.e. the transformed impedance is now complex, so that a phase shift is also introduced in the current flowing through the PCD antenna. Therefore, it must be assumed that both load modulation techniques are accompanied with a change in amplitude *and* a phase shift.

5.1.2 Maximum U_{IC}

Although resonance frequency is determined for the entire PICC in mind, there may be a frequency different from $\omega_{RES,ph}$ that allows an individual component of a PICC to operate at its optimal conditions. In case of IC manufacturers, for example, it is reasonable to define resonance at the frequency where the voltage across the IC is at maximum (U_{IC} in fig. 5.1). This also means that most active power shall be dissipated by the IC if operated at this frequency, denoted as $\omega_{RES,U_{IC}}$. Hence, $\omega_{RES,U_{IC}}$ is the most important definition of resonance frequency for manufacturers that provide ICs for proximity coupling systems. In order to determine $\omega_{RES,U_{IC}}$, one starts from the expression for U_{IC} and uses the familiar expressions for Z_{IC} and Z_{PICC} :

$$\begin{aligned} \underline{U}_{IC} &= \underline{U}_{PICC} \frac{Z_{IC}}{Z_{PICC}} = \underline{U}_{PICC} \frac{\frac{R_{IC}}{1 + j\omega R_{IC}C}}{R_{LPICC} + j\omega L_{PICC} + \frac{R_{IC}}{1 + j\omega R_{IC}C}} \\ &= \frac{\underline{U}_{PICC}}{\left(1 - \omega^2 L_{PICC}C + \frac{R_{LPICC}}{R_{IC}}\right) + j\omega \left(CR_{LPICC} + \frac{L_{PICC}}{R_{IC}}\right)} \end{aligned}$$

Furthermore, voltage U_{PICC} in fig. 5.1 is induced by the PCD current via mutual induction, and can thus be expressed as:

$$\underline{U}_{PICC} = j\omega M \underline{I}_{PCD}$$

That allows U_{IC} to be defined by the following equation:

$$\underline{U}_{IC} = \frac{j\omega M \underline{I}_{PCD}}{\left(1 - \omega^2 L_{PICC}C + \frac{R_{LPICC}}{R_{IC}}\right) + j\omega \left(CR_{LPICC} + \frac{L_{PICC}}{R_{IC}}\right)} \quad (5.2)$$

If the magnitude of eq. 5.2 is set at maximum, a final expression for $\omega_{RES,U_{IC}}$ can be obtained:

$$\begin{aligned} \Rightarrow |\underline{U}_{IC}| &= M |\underline{I}_{PCD}| \frac{\omega}{\sqrt{\left(1 - \omega^2 L_{PICC}C + \frac{R_{LPICC}}{R_{IC}}\right)^2 + \left[\omega \left(CR_{LPICC} + \frac{L_{PICC}}{R_{IC}}\right)\right]^2}} \\ \frac{d|\underline{U}_{IC}|}{d\omega} &\stackrel{!}{=} 0 \Rightarrow \omega_{RES,U_{IC}} = \sqrt{\frac{1 + \frac{R_{LPICC}}{R_{IC}}}{L_{PICC}C}} \quad (5.3) \end{aligned}$$

5.1 Definition of Resonance Frequency

Eq. 5.3 closely resembles the Thomson equation, except for the term $\frac{R_{LPICC}}{R_{IC}}$, which is an important relation in the considerations to come. For now, a conclusion can be drawn that $\omega_{RES,U_{IC}}$ is the primarily desired theoretical resonance frequency. Unfortunately, it cannot be measured in practice because there is no way to measure U_{IC} of enclosed and laminated PICCs without contacting them directly. Therefore, one has to rely on measurements that are based on magnetic coupling, such as the one performed on a vector network analyzer.

5.1.3 Maximum $\Re\{\underline{Z}_{VNA}\}$

The currently established VNA method for measuring resonance frequency of PICCs is also based on the main principle behind proximity coupling systems: the inductive coupling. Before describing the actual measurement setup, it is required to elaborate on how resonance frequency is defined by the VNA method, as well as how it differs from $\omega_{RES,U_{IC}}$, which is chosen as the optimal frequency that can be achieved.

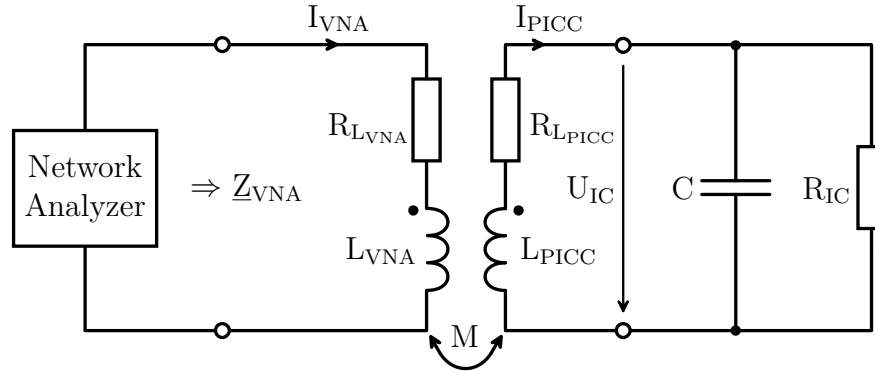


Figure 5.3: Equivalent circuit of a network analyzer measurement setup (adapted from [1])

An equivalent circuit of the VNA method is depicted in fig. 5.3. The role of the PCD is assumed by the VNA, including a measuring coil with inductance L_{VNA} and serial resistance R_{LVNA} . Same as with a typical PCD, the PICC is represented by the transformed impedance \underline{Z}_T in the VNA circuit. Therefore, the input impedance \underline{Z}_{VNA} , measured by the network analyzer, is given as:

$$\underline{Z}_{VNA} = R_{LVNA} + j\omega L_{VNA} + \underline{Z}_T$$

Substituting the familiar expression for \underline{Z}_T (eq. 4.7) gives:

$$\underline{Z}_{VNA} = R_{LVNA} + j\omega L_{VNA} + \frac{\omega^2 k^2 L_{VNA} L_{PICC}}{R_{LPICC} + j\omega L_{PICC} + \frac{R_{IC}}{1 + j\omega R_{IC} C}} \quad (5.4)$$

5.1 Definition of Resonance Frequency

Generally, when the PICC is tuned to the transmission frequency of the PCD, the transformed impedance \underline{Z}_T is real and at maximum. This means that it would be reasonable to define resonance frequency at the maximum *magnitude* of \underline{Z}_T . However, the VNA method does not measure only $\underline{Z}_T(f)$, but rather it measures $\underline{Z}_{VNA}(f)$, which is essentially \underline{Z}_T that also includes the impedance of the measuring coil, measured over frequency. This can be visualized by a locus curve of $\underline{Z}_{VNA}(f)$ (fig. 5.4).

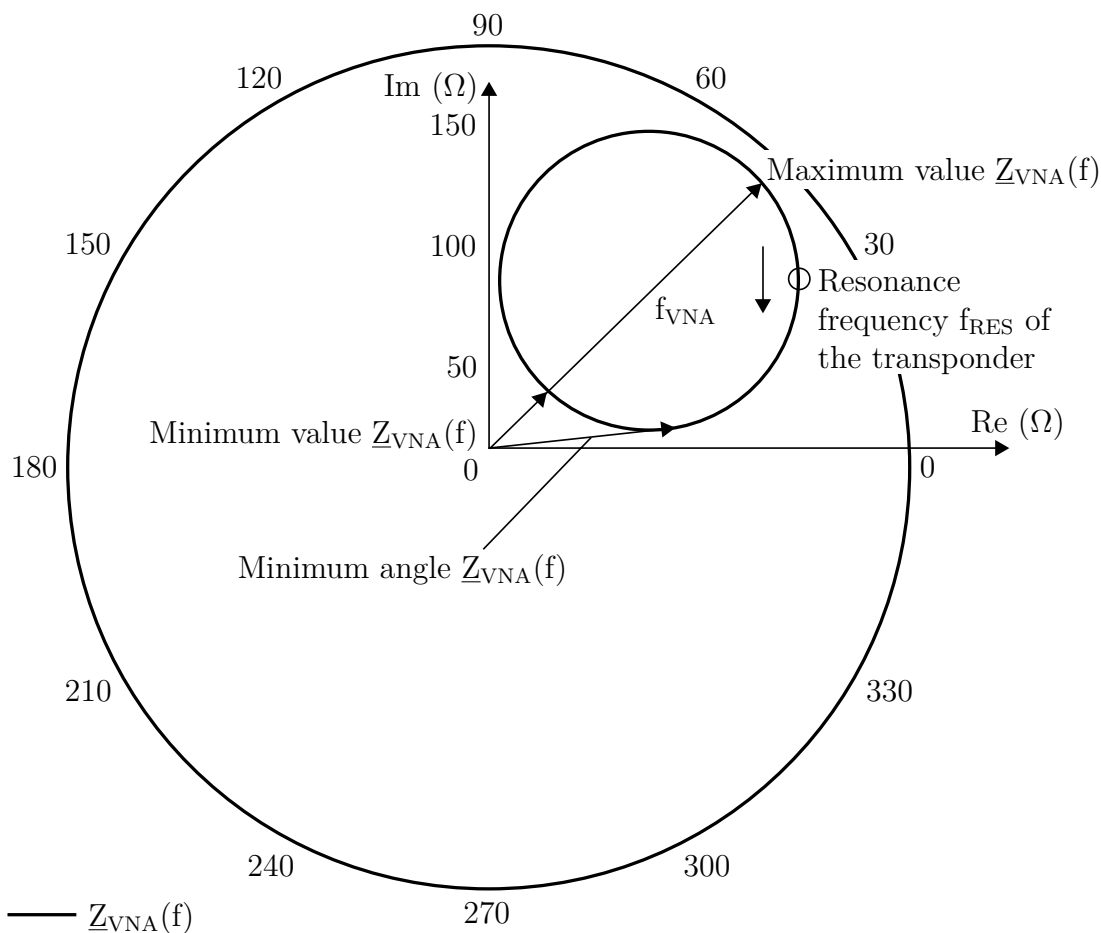


Figure 5.4: Locus curve of the impedance \underline{Z}_{VNA} measured with a network analyzer (adapted from [1])

Examining both eq. 5.4 and fig. 5.4, it is clear that the measuring coil parameters R_{LVNA} and L_{VNA} merely cause the center of the $\underline{Z}_{VNA}(f)$ circle to shift away from the real axis. Therefore, the resonance frequency of the VNA method must be defined as the frequency where the *real part* of \underline{Z}_{VNA} reaches its maximum. This point is also visible in fig. 5.4 as the encircled f_{RES} . If a compensation measurement were to be performed to eliminate the measuring coil, the center of

5.1 Definition of Resonance Frequency

the circle would lie on the real axis and $\underline{Z}_{\text{VNA}}(f)$ would be equivalent to $\underline{Z}_{\text{T}}(f)$ in that case, allowing the resonance frequency to be determined by the maximum magnitude of $\underline{Z}_{\text{VNA}}(f)$ as well.

Now that the resonance frequency for the VNA method is defined as maximum real part of $\Re\{\underline{Z}_{\text{VNA}}\}$, it can be proceeded with the analytical considerations. Expression for $\underline{Z}_{\text{VNA}}$ (eq. 5.4) is split into its real and imaginary components:

$$\Re\{\underline{Z}_{\text{VNA}}\} = R_{\text{LVNA}} + \frac{\omega^2 k^2 L_{\text{VNA}} L_{\text{PICC}} \left(1 + \frac{R_{\text{LPICC}}}{R_{\text{IC}}} + \omega^2 C^2 R_{\text{LPICC}} \right)}{\left(1 + \frac{R_{\text{LPICC}}}{R_{\text{IC}}} - \omega^2 L_{\text{PICC}} C \right)^2 + \omega^2 \left(\frac{L_{\text{PICC}}}{R_{\text{IC}}} + C R_{\text{LPICC}} \right)^2}$$

$$\Im\{\underline{Z}_{\text{VNA}}\} = \omega \left\{ L_{\text{VNA}} + \frac{\omega^2 k^2 L_{\text{VNA}} L_{\text{PICC}} \left(C(1 - \omega^2 L_{\text{PICC}} C) - \frac{L_{\text{PICC}}}{R_{\text{IC}}^2} \right)}{\left(1 + \frac{R_{\text{LPICC}}}{R_{\text{IC}}} - \omega^2 L_{\text{PICC}} C \right)^2 + \omega^2 \left(\frac{L_{\text{PICC}}}{R_{\text{IC}}} + C R_{\text{LPICC}} \right)^2} \right\}$$

The real part of $\underline{Z}_{\text{VNA}}$ is subsequently set at maximum:

$$\frac{d\Re\{\underline{Z}_{\text{VNA}}\}}{d\omega} \stackrel{!}{=} 0 \quad (5.5)$$

Solving 5.5 for ω is very complicated, and is therefore not shown. However, the expression for $\Re\{\underline{Z}_{\text{VNA}}\}$ can be simplified if the following conditions are met:

$$\begin{aligned} R_{\text{LPICC}} &\ll \omega L_{\text{PICC}} \\ R_{\text{LPICC}} &\ll R_{\text{IC}} \end{aligned}$$

$\Re\{\underline{Z}_{\text{VNA}}\}$ then becomes:

$$\Re\{\underline{Z}_{\text{VNA}}\} \approx \frac{\omega^2 k^2 L_{\text{VNA}} L_{\text{PICC}} \left(\frac{1}{R_{\text{IC}}} + \omega^2 C^2 R_{\text{LPICC}} \right)}{(1 - \omega^2 L_{\text{PICC}} C)^2 + \omega^2 \left(\frac{L_{\text{PICC}}}{R_{\text{IC}}} + C R_{\text{LPICC}} \right)^2}$$

The resonance frequency $\omega_{\text{RES,VNA}}$ for the VNA method is in that case approximated by the Thomson equation:

$$\Rightarrow \omega_{\text{RES,VNA}} \approx \sqrt{\frac{1}{L_{\text{PICC}} C}} \quad (5.6)$$

5.1.4 Comparison of Different Definitions

The three presented definitions of resonance frequency: $\omega_{\text{RES},ph}$ (eq. 5.1), $\omega_{\text{RES},U_{\text{IC}}}$ (eq. 5.3), and $\omega_{\text{RES},\text{VNA}}$ (eq. 5.6) have in common that, under certain conditions, all of them reduce to the Thomson equation, which allows them to be considered equivalent to one another. The most important of these conditions is that the resistance of the IC in a PICC should be much higher than serial resistance of the antenna:

$$R_{L_{\text{PICC}}} \ll R_{\text{IC}} \quad (5.7)$$

As this is usually the case for PICCs in proximity coupling systems, this is the main reason why the VNA method is widely accepted as the method for measuring resonance frequency. However, if condition 5.7 is not fulfilled and resistance R_{IC} at some point happens to have a much lower value (e.g. due to shunt regulator or load modulation), the three definitions for f_{RES} are no longer equivalent. This can be illustrated with a polar plot of transformed impedance \underline{Z}_{T} with now clearly different values of the aforementioned three resonance frequencies (fig. 5.5).

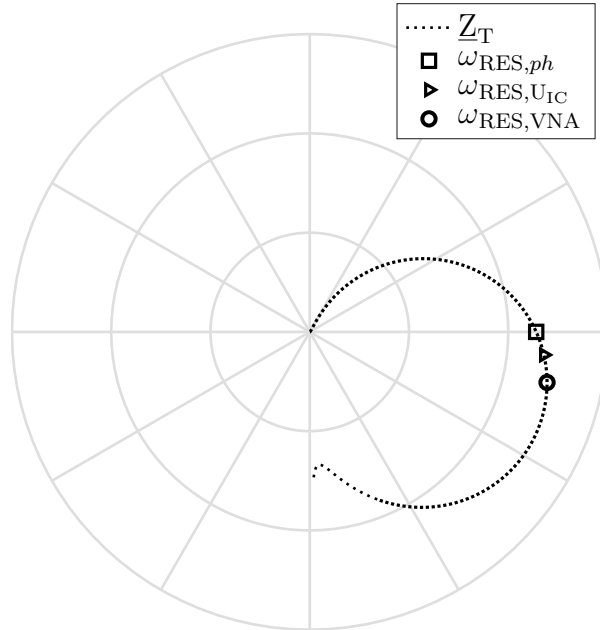


Figure 5.5: Different definitions of resonance frequency

5.2 Measuring the Resonance Frequency

The measurement with the VNA method is performed by a vector network analyzer, such as the one depicted in fig. 5.6. The PICC is placed on the measuring coil and the curve representing the real part of the measured impedance $\underline{Z}_{\text{VNA}}$ over frequency is displayed. The frequency sweep lasts only several seconds, so that f_{RES} can also be tuned to another frequency while being measured, typically by using a tune capacitance included in the PICC (fig. 4.4). The desired range of the frequency sweep can be chosen by configuring the VNA, usually falling between 10 and 20 MHz because most PICCs are tuned to a frequency around 13.56 MHz.

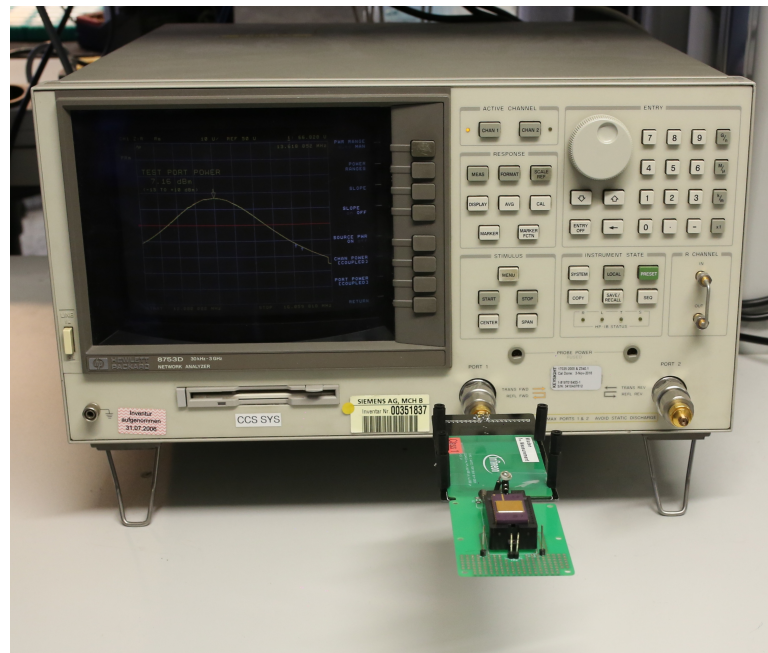


Figure 5.6: Vector network analyzer setup used for measuring f_{RES} (courtesy of Infineon Technologies Austria AG)

In order to determine f_{RES} , it is only required to read out the frequency from the display where the $\Re\{\underline{Z}_{\text{VNA}}\}$ curve is at maximum (fig. 5.7). Some VNAs are able to simultaneously measure the Q factor as well. Despite being so straightforward with respect to readout, measurement of the resonance frequency with the VNA method is faced with many challenges. This has to do with the general properties of ICs that are utilized for PICCs in proximity coupling systems.

Up to this point, the PICC has been described as a system consisting of an antenna and an IC and modeled as a linear circuit with the highest possible degree of simplification. In reality, the IC part of the PICC is a highly sophisticated

5.2 Measuring the Resonance Frequency

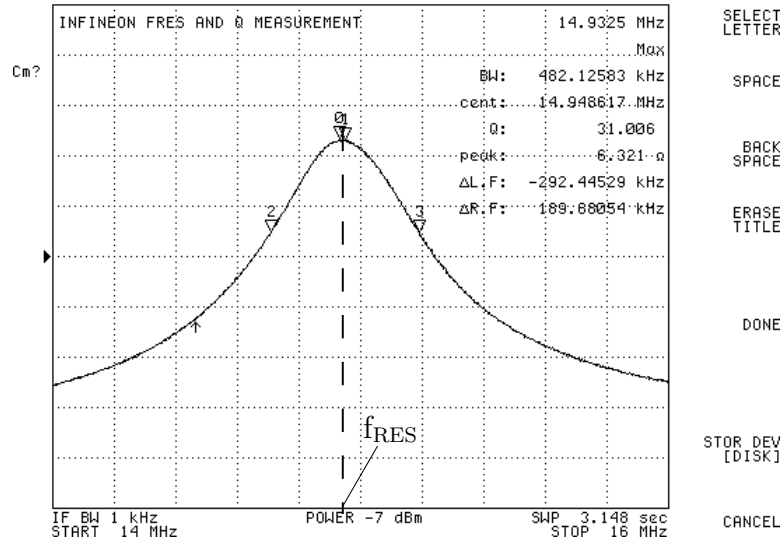


Figure 5.7: Resonance frequency f_{RES} shown as maximum real part of the impedance Z_{VNA} measured with a network analyzer (adapted from [1])

micro-controller, and is therefore far from being a linear circuit. During numerous different stages in communication and execution, the IC continuously changes its electrical properties. Observed from outside, it can still be considered as a black box and modeled by its input characteristics (C_{IC} and R_{IC} in fig. 4.4). The consequence is, however, that these input characteristics depend on the *input voltage* (U_{IC}) and hence also implicitly depend on the *input power* to the entire PICC. Qualitative behavior of C_{IC} and R_{IC} with respect to input voltage in case of a commercial IC can be seen in fig. 5.8.

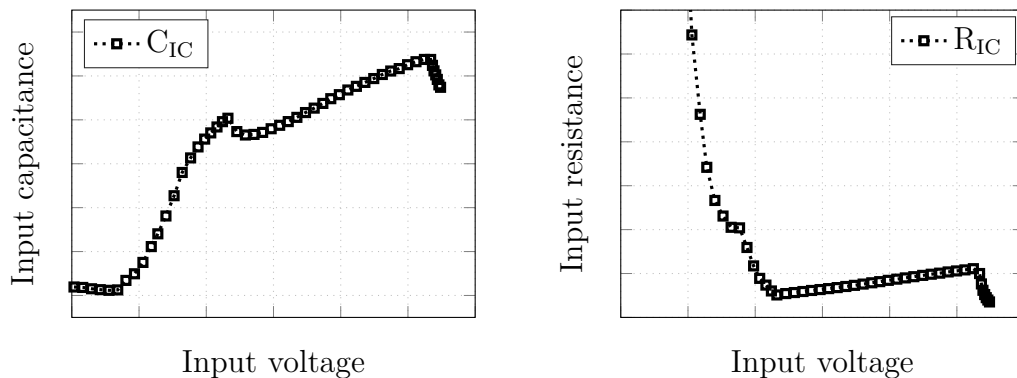


Figure 5.8: Exemplary input characteristics as function of input voltage in case of a commercial IC

5.3 Disadvantages of the VNA method

The dependence on input power to the ICs introduces a whole new dimension in measuring the resonance frequency. Therefore, one must define the power level at which f_{RES} shall be measured, because C_{IC} and R_{IC} change with the input power, causing the resonance frequency to change as well. Typically, this power level is defined as the point where the IC receives enough energy to turn on, also referred to as the *start-up* point. Unfortunately, the start-up point cannot be quantitatively defined when using a VNA, because it depends on many parameters such as the chosen IC, antenna, field strength, and even f_{RES} . For that reason, when measuring f_{RES} with the VNA method, one has to rely on qualitative definitions for the start-up point, which are mainly based on the shape of the $\Re\{Z_{\text{VNA}}\}$ curve. The input power of the network analyzer must first be appropriately adjusted so the start-up point can be visible, and only then can the resonance frequency be read out from the display. This is one of the main disadvantages of the VNA method, which shall be discussed in the next section.

5.3 Disadvantages of the VNA method

The motivation behind finding a new method to measure resonance frequency is reflected in the disadvantages of the currently used VNA method. They are pointed out in this section, along with some possibilities for improvement.

Different definitions for f_{RES} : The analytical derivation of $\omega_{\text{RES,VNA}}$ in this chapter showed that the maximum $\Re\{Z_{\text{VNA}}\}$ definition used by the VNA method only partly coincides with $\omega_{\text{RES,UIC}}$, which is chosen as the optimal resonance frequency. Nevertheless, considering how condition 5.7 is mostly fulfilled for the input power levels at which PICCs are usually measured, the maximum $\Re\{Z_{\text{VNA}}\}$ definition is accepted. If a new definition of resonance frequency were to be found, one that is closer to $\omega_{\text{RES,UIC}}$, it would undoubtedly take precedence over the current definition.

Start-up point must be determined manually: Due to the fact that the input characteristics of an IC change depending on the input power (fig. 5.8), the $\Re\{Z_{\text{VNA}}\}$ curve also changes during measurement with the VNA method as soon as the input power of the VNA frequency sweep is changed. As resonance frequency is defined at the IC start-up point, one has to qualitatively adjust the input power level on the VNA in order to determine f_{RES} . It is thus desirable to have a measurement method that can set the input power at the start-up point automatically.

Subjective: Because the search for the start-up point is qualitative and not defined at an exact input power value, there is a great deal of subjectivity

5.3 Disadvantages of the VNA method

involved in the VNA method. Two different people may not always decide on exactly the same power level when performing the measurement on the same PICC, which can lead to reproducibility issues. Hence, there is great need for a measurement method that would be objective and reproducible, irrespective of the human factor.

No correlation to field strength H: The input power level on the VNA is chosen in dBm, whereas for PICCs it is often required to know the value of magnetic field strength at which the IC starts up. However, as H depends on the PICC antenna (i.e. on the coupling coefficient k), and because the VNA performs a sweep over a large range of frequencies in a several seconds time, there is no way to correlate the chosen dBm level of input power on the VNA to the magnetic field strength acting on the PICC. A correlation between f_{RES} and H is strongly desired, which can perhaps be achieved by measuring f_{RES} using systems that are focused on determining H , such as the ISO test PCD assembly.

Not integrated into standardized setups: Many measurements performed in development and verification of proximity coupling systems utilize standardized setups, such as the ISO setup with a test PCD assembly described in chapter 4. On the other hand, when measuring the resonance frequency is required between two other measurements on an ISO setup, one has to remove the PICC from the ISO setup and go to the network analyzer to measure f_{RES} . If a method were integrated into the standardized setups, it would save a lot of time and even introduce possibility for automation.

No automation: If resonance frequency measurement must be performed for multiple PICCs, all of them must be measured on the VNA individually. The VNA method hence offers no automation whatsoever. However, if a resonance frequency measurement were possible on the ISO test PCD assembly, there are constellations where multiple PICCs could be measured in a single run, without the need of an engineer to be present. This would greatly save time and increase productivity.

Due to all reasons mentioned above, a new and improved method of measuring resonance frequency was conceptualized and developed in this thesis. The intent was to eliminate the disadvantages of the VNA method, as well as to streamline the productivity of standardized tests used in verification of proximity coupling systems. This new method shall be presented in the next chapter.

Chapter 6

Theory of the Extended Measurement Method

A new method for measuring the resonance frequency of contactless chip cards is proposed in this chapter. This method takes into account the pitfalls of the VNA method and offers a better realization of the measurement by integrating it into the ISO test PCD assembly. This chapter gives a theoretical overview for the new method, thoroughly explaining each step of the process. Based on these theoretical assumptions, the feasibility of the method is further examined using software simulations and computations. Results of the simulated measurement will show that measuring resonance frequency offers certain advantages when using this new method, henceforth regarded as the *extended method*.

This chapter explains the underlying theoretical principles upon which the extended method is conceived. However, it should be noted that a certain level of abstraction is assumed for the considerations described here. The actual implementation of the measurement and the measured samples are not the focus of this chapter and shall be covered in the following chapters. Nevertheless, this chapter defines the measurement procedure in its entirety, starting from a new definition of resonance based on active power in the PICC, up to the last signal processing step in obtaining the resonance frequency.

6.1 Active Power in the PICC

As described in chapter 5, the VNA method defines resonance frequency as frequency where the real part of impedance Z_{VNA} reaches its maximum. The proposed new definition deviates from this and defines resonance frequency as the frequency where the *active power* in the PICC is at maximum. Again, the fa-

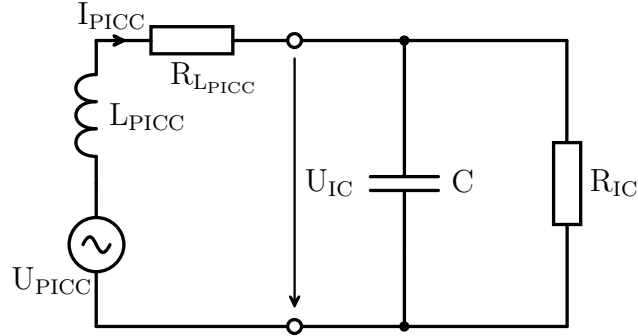


Figure 6.1: The simplified PICC equivalent circuit is also used for the extended method's definition of resonance frequency

miliar simplified PICC circuit (fig. 6.1) shall be used for defining the resonance frequency.

For this purpose, an AC analysis is performed where U_{PICC} has a constant amplitude over all frequencies considered in the analysis. Two active power quantities are defined for the circuit: The total active power in the PICC, denoted as P_{PICC} , and the active power consumed only by the IC, denoted as P_{IC} . These two quantities are not identical, although they may be treated equally for the purpose of obtaining resonance frequency, as long as a certain condition is fulfilled. Using P_{PICC} instead of P_{IC} is one of the main premises of the extended method, which shall be justified by the aforementioned condition (derived later).

Applying complex AC analysis allows both forms of active power to be determined, starting from the expression for complex apparent power \underline{S} :

$$\underline{S} = \underline{U} \underline{I}^* = P + jQ \quad (6.1)$$

where active power P is defined as real part of \underline{S} :

$$P = \Re\{\underline{S}\} \quad (6.2)$$

Two complex apparent power expressions are distinguished, $\underline{S}_{\text{PICC}}$ for the entire PICC and $\underline{S}_{\text{IC}}$ for only the IC:

$$\underline{S}_{\text{PICC}} = \underline{U}_{\text{PICC}} \underline{I}_{\text{PICC}}^* \quad (6.3)$$

$$\underline{S}_{\text{IC}} = \underline{U}_{\text{IC}} \underline{I}_{\text{PICC}}^* \quad (6.4)$$

Current $\underline{I}_{\text{PICC}}$ and voltage $\underline{U}_{\text{IC}}$ are expressed in relation to impedances $\underline{Z}_{\text{PICC}}$ and $\underline{Z}_{\text{IC}}$:

$$\underline{I}_{\text{PICC}} = \frac{\underline{U}_{\text{PICC}}}{\underline{Z}_{\text{PICC}}} \quad (6.5)$$

$$\underline{U}_{\text{IC}} = \underline{I}_{\text{PICC}} \underline{Z}_{\text{IC}} = \underline{U}_{\text{PICC}} \frac{\underline{Z}_{\text{IC}}}{\underline{Z}_{\text{PICC}}} \quad (6.6)$$

6.1 Active Power in the PICC

The impedance \underline{Z}_{IC} is obtained by connecting C_{IC} and R_{IC} in parallel:

$$\underline{Z}_{IC} = \frac{1}{j\omega C} \parallel R_{IC} = \frac{1}{\frac{1}{R_{IC}} + j\omega C} \quad (6.7)$$

The denominator is rationalized, followed by separating the real and imaginary part of \underline{Z}_{IC} , which shall later become useful:

$$\begin{aligned} \underline{Z}_{IC} &= \frac{1}{\frac{1}{R_{IC}} + j\omega C} \cdot \frac{\frac{1}{R_{IC}} - j\omega C}{\frac{1}{R_{IC}} - j\omega C} = \frac{\frac{1}{R_{IC}} - j\omega C}{\frac{1}{R_{IC}^2} + \omega^2 C^2} = \\ &= \underbrace{\frac{\frac{1}{R_{IC}}}{\frac{1}{R_{IC}^2} + \omega^2 C^2}}_{\Re} - j \underbrace{\frac{\omega C}{\frac{1}{R_{IC}^2} + \omega^2 C^2}}_{\Im} \end{aligned} \quad (6.8)$$

The total impedance \underline{Z}_{PICC} includes the antenna impedance as well, and is also split in real and imaginary parts:

$$\begin{aligned} \underline{Z}_{PICC} &= j\omega L_{PICC} + R_{L_{PICC}} + \underline{Z}_{IC} = j\omega L_{PICC} + R_{L_{PICC}} + \frac{\frac{1}{R_{IC}} - j\omega C}{\frac{1}{R_{IC}^2} + \omega^2 C^2} = \\ &= \underbrace{R_{L_{PICC}} + \frac{\frac{1}{R_{IC}}}{\frac{1}{R_{IC}^2} + \omega^2 C^2}}_{\Re} + j \underbrace{\left\{ \omega L_{PICC} - \frac{\omega C}{\frac{1}{R_{IC}^2} + \omega^2 C^2} \right\}}_{\Im} \end{aligned} \quad (6.9)$$

Next, the active power P_{PICC} is defined and using eq. 6.3 and 6.5 expressed as:

$$\begin{aligned} P_{PICC} &= \Re\{\underline{S}_{PICC}\} = \Re\{\underline{U}_{PICC} \underline{I}_{PICC}^*\} = \\ &= \Re\left\{ \underline{U}_{PICC} \left(\frac{\underline{U}_{PICC}}{\underline{Z}_{PICC}} \right)^* \right\} = \Re\left\{ \frac{|\underline{U}_{PICC}|^2}{\underline{Z}_{PICC}^*} \right\} \end{aligned}$$

Rationalizing the denominator leads to:

$$\begin{aligned} P_{PICC} &= \Re\left\{ \frac{|\underline{U}_{PICC}|^2}{\underline{Z}_{PICC}^*} \cdot \frac{\underline{Z}_{PICC}}{\underline{Z}_{PICC}} \right\} = \Re\left\{ \frac{|\underline{U}_{PICC}|^2}{|\underline{Z}_{PICC}|^2} \underline{Z}_{PICC} \right\} = \\ &= \frac{|\underline{U}_{PICC}|^2}{|\underline{Z}_{PICC}|^2} \Re\{\underline{Z}_{PICC}\} \end{aligned} \quad (6.10)$$

6.1 Active Power in the PICC

The active power P_{IC} is expressed in the same manner, using eq. 6.4 and 6.6:

$$\begin{aligned}
 P_{IC} &= \Re\{S_{IC}\} = \Re\{U_{IC}I_{PICC}^*\} = \Re\left\{U_{IC}\left(\frac{U_{PICC}}{Z_{PICC}}\right)^*\right\} = \\
 &= \Re\left\{U_{PICC}\frac{Z_{IC}}{Z_{PICC}}\cdot\left(\frac{U_{PICC}}{Z_{PICC}}\right)^*\right\} = \\
 &= \frac{|U_{PICC}|^2}{|Z_{PICC}|^2}\Re\{Z_{IC}\}
 \end{aligned} \tag{6.11}$$

The preferred definition for resonance frequency would be the frequency where P_{IC} is at maximum. In order to find this frequency, denoted as ω_{RES} , first derivative of P_{IC} from eq. 6.11 is set to zero:

$$\frac{dP_{IC}}{d\omega} \stackrel{!}{=} 0 \tag{6.12}$$

Solving eq. 6.12 for ω leads to the following expression for ω_{RES} :

$$\omega_{RES,ic} = \frac{\sqrt{2CR_{IC}^2L_{PICC} - C^2R_{IC}^2R_{LPICC}^2 - L_{PICC}^2}}{\sqrt{2}CR_{IC}L_{PICC}} \tag{6.13}$$

However, the extended method does not define ω_{RES} this way. In order to understand the reason, the entire system consisting of test PCD assembly and PICC needs to be taken into account, which shall be explained later. For now, let eq. 6.10 and eq. 6.11 be more closely examined. It can be seen that P_{IC} and P_{PICC} differ only in the real part of impedances Z_{IC} and Z_{PICC} , which are taken from eq. 6.8 and 6.9, respectively:

$$\Re\{Z_{IC}\} = \frac{1}{\frac{1}{R_{IC}} + \omega^2C^2} \tag{6.14}$$

$$\Re\{Z_{PICC}\} = R_{LPICC} + \frac{1}{\frac{1}{R_{IC}} + \omega^2C^2} \tag{6.15}$$

Expressions 6.14 and 6.15, on the other hand, differ only in the antenna resistance R_{LPICC} occurring in eq. 6.15. The assumption is that most of the active power in the PICC will be consumed by the IC, so that the R_{PICC} term in eq. 6.15 has a

negligible effect on the active power. Thus, the familiar condition of R_{PICC} being significantly lower than R_{IC} appears once again:

$$R_{LPICC} \ll R_{IC} \quad (6.16)$$

When the condition is fulfilled, the expression 6.10 for P_{PICC} can be used instead of P_{IC} . Similarly, setting the first derivative of P_{PICC} to zero:

$$\frac{dP_{PICC}}{d\omega} \stackrel{!}{=} 0 \quad (6.17)$$

determines the resonance frequency ω_{RES} of the active power in the entire PICC as:

$$\omega_{RES,picc} = \frac{\sqrt{\frac{CR_{IC}\sqrt{R_{IC}^2 + R_{LPICC}R_{IC}}}{L_{PICC}} + \frac{\sqrt{R_{IC}^2 + R_{LPICC}R_{IC}}}{R_{LPICC}} - \frac{R_{IC}}{R_{LPICC}} - 1}}{CR_{IC}} \quad (6.18)$$

Eq. 6.18 reduces to eq. 6.13 when condition 6.16 is fulfilled. Therefore, resonance frequency for the extended method is defined by eq. 6.18.

6.2 Relative Active Power P_{REL}

Next step is to take the entire ISO test PCD assembly into consideration, its equivalent circuit being shown in fig. 4.15 and the considered mutual inductances listed in table 4.2.

As explained in chapter 4, the only coupling concerning the calibration coil is the one with the PCD. However, it is important to notice that the coupling between the PICC antenna L_{PICC} and lower sense coil $L_{SC,down}$ is neglected for the purpose of simplifying the extended method's theoretical model. Although this is not the case in reality, neglecting this very weak coupling significantly reduces effort in analytical calculations.

Two signals are observable in the ISO test PCD assembly, the calibration coil voltage U_{CC} and the sense coil differential voltage U_{SC} . The voltage U_{PICC} that is induced in the PICC is not explicitly shown in fig. 4.15, but rather represented through mutual inductance M between the PCD and the PICC:

$$U_{PICC} = j\omega MI_{PCD} \quad (6.19)$$

Nevertheless, the voltage U_{CC} measured by the calibration coil has the same phase characteristics as U_{PICC} because both voltages are induced simultaneously

by the PCD. They do differ in amplitude, although only by a mere proportionality due to a different coupling coefficient k .

Eq. 6.10 states that the total active power in the PICC can be obtained when U_{PICC} and I_{PICC} are known, whereas the active power on the IC, given by eq. 6.11, requires knowledge of U_{IC} instead of U_{PICC} . Unfortunately, the voltage U_{IC} is not directly observable by the ISO test PCD assembly. Due to unavailability of U_{IC} , it is also not possible to determine the active power P_{IC} . Therefore, the proposed definition of resonance frequency ω_{RES} for the extended method is based on P_{PICC} , with its difference to active power P_{IC} available at the IC depending on the power dissipated by the PICC antenna resistance R_{LPICC} . Under the condition given in 6.16 that R_{LPICC} is significantly lower than R_{IC} it is assumed that this part is negligible, which is generally the case for circuit parameters of a system that consists of an ISO test PCD assembly and a PICC.

The following question arises: *How can a resonance frequency measurement be implemented relying on the test PCD assembly?* An answer is given by the extended method describing a measurement that can be performed with a time domain signal including frequency components covering the frequency range of interest. Such signal would be supplied by the AWG and thus integrable into the AWG test set-up. An obvious choice for the input signal presents itself in form of a so-called chirp signal, which is a signal whose frequency is linearly swept over time.

If a chirp signal with a constant amplitude and a certain range of frequencies, between 10 MHz and 20 MHz for example, is fed into the test PCD assembly, the output voltage at the calibration coil also has the form of a chirp signal. However, the envelope of this output is not constant in amplitude. This is because the PCD circuit of the test assembly is impedance matched to $50\ \Omega$ at exactly 13.56 MHz, which results in an optimized power transfer between the signal generator and the PCD antenna at this frequency. Due to mismatch at other frequency components present in the chirp, the input chirp with constant envelope is detected by the calibration coil as a voltage chirp signal (U_{CC}) with an envelope that varies in amplitude and has a maximum at 13.56 MHz. As already mentioned, voltage is induced in the PICC as well (U_{PICC}), having the same phase characteristics and shape as U_{CC} . Its amplitude is proportional to the amplitude of U_{CC} by a certain factor. By looking again at the expression for active power in the PICC:

$$P_{PICC} = \Re\{U_{PICC}I_{PICC}^*\} \quad (6.20)$$

it can be seen that the two signals necessary for obtaining P_{PICC} in frequency domain are U_{PICC} and I_{PICC} . Expressing eq. 6.20 in phasor form results in:

$$P_{PICC} = U_{PICC}I_{PICC} \cos(\varphi) \quad (6.21)$$

where U_{PICC} and I_{PICC} are the magnitudes of \underline{U}_{PICC} and \underline{I}_{PICC} :

$$\begin{aligned} U_{PICC} &= |\underline{U}_{PICC}| \\ I_{PICC} &= |\underline{I}_{PICC}| \end{aligned}$$

Angle φ represents the phase angle between \underline{U}_{PICC} and \underline{I}_{PICC} phasors, as shown in fig. 6.2.

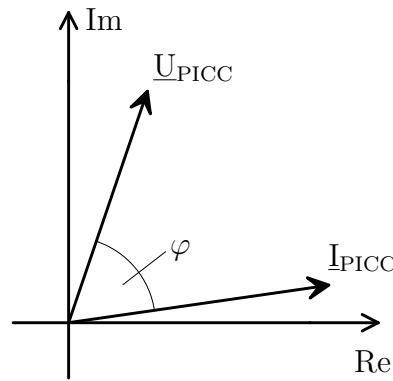


Figure 6.2: Phasor representation of \underline{U}_{PICC} and \underline{I}_{PICC} , with phase angle φ

Using a chirp signal as input, P_{PICC} can be calculated if time domain signals U_{PICC} and I_{PICC} are known. The instantaneous frequency of the chirp signal can then be determined for the point in time where P_{PICC} is maximal, which is ultimately defined as the resonance frequency of the PICC. However, a setback that occurs is that U_{PICC} is influenced by the aforementioned envelope variation due to impedance mismatch at frequencies other than 13.56 MHz. For the P_{PICC} calculation to be applicable, the influence of the test PCD assembly requires to be compensated in some way. This can be achieved by manipulating the input chirp signal's amplitude, in this thesis regarded as *shaping*, so that the envelope of output U_{CC} becomes constant for the entire range of frequencies present in the chirp. Because U_{PICC} is proportional to and in-phase with U_{CC} , it can be assumed that a constant voltage is also induced in the PICC for the desired range of frequencies, thus validating the use of a constant voltage source in the PICC for the AC analysis shown in fig. 4.5. On the other hand, the current I_{PICC} is not constant over the range of frequencies and it shall depend on the frequency response of the PICC and therefore shall reflect the PICC's resonance frequency. In order to simplify the calculation, a new physical quantity denoted as *relative active power* P_{REL} can be introduced by eliminating the constant magnitude

U_{PICC} from eq. 6.21:

$$\begin{aligned}
 U_{PICC} &= \text{const.} \\
 \Rightarrow P_{REL} &= \frac{P_{PICC}}{U_{PICC}} = \frac{\overline{U_{PICC}} I_{PICC} \cos(\varphi)}{\overline{U_{PICC}}} \\
 \Rightarrow P_{REL} &= I_{PICC} \cos(\varphi) \tag{6.22}
 \end{aligned}$$

In phasor form, this corresponds to dividing the phasor \underline{U}_{PICC} by its magnitude U_{PICC} , thus preserving the resulting unity phasor to be used as a reference for the phase angle φ between \underline{U}_{PICC} and \underline{I}_{PICC} :

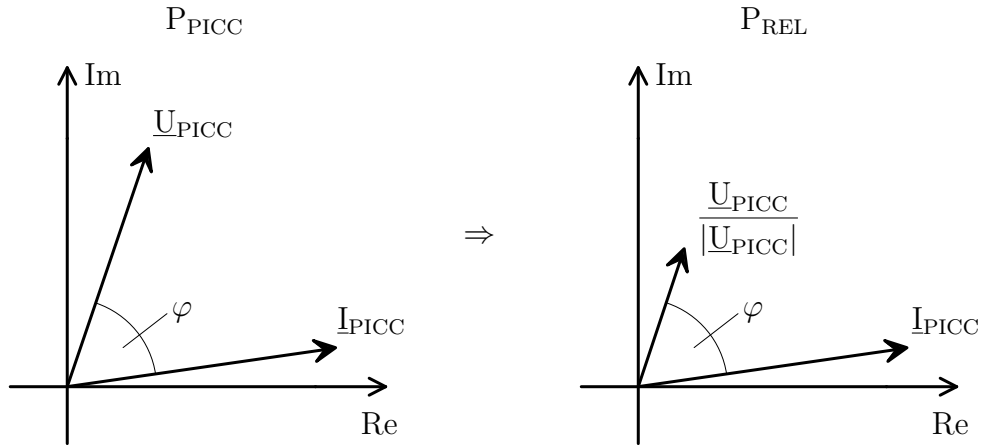


Figure 6.3: Phasor representation of \underline{U}_{PICC} and \underline{I}_{PICC} for P_{REL}

Consequently, the relative active power P_{REL} is proportional to P_{PICC} , maintaining the position of its maximum on the time axis, and the information about the resonance frequency along with it. One could argue that the physical dimension of P_{REL} from eq. 6.22 is that of current instead of power, but for this purpose it shall be regarded as power, and its lack of proper dimension expressed through the word “relative”. To summarize, the requirements for obtaining P_{REL} are:

- constant envelope of voltage U_{PICC} for the desired range of frequencies
- current I_{PICC}
- phase angle φ between \underline{U}_{PICC} and \underline{I}_{PICC}

The two main objectives of the extended method are the shaping of the voltage U_{PICC} based on measured voltage U_{CC} on the one hand, and obtaining the current I_{PICC} by applying the transfer function that describes the relation between U_{SC} and I_{PICC} on the other hand. These two tasks are described separately in the following sections. The phase angle φ is easily acquired as phase difference between the shaped U_{PICC} and I_{PICC} . Fulfilling all objectives allows the relative active power P_{REL} in the PICC, as formulated in eq. 6.22, to be obtained, so that resonance frequency can be determined at the point where P_{REL} reaches its maximum.

6.3 Shaping of U_{PICC}

The ISO test PCD assembly shown in fig. 4.15 is a system with AWG voltage U_{AWG} as the input, whereas the calibration coil voltage U_{CC} and sense coil differential voltage U_{SC} are the two outputs. In this section, the only output of interest is U_{CC} . Both input and output shall be expressed in signal form, independent of their physical quantities. This simplified system description is shown in fig. 6.4.

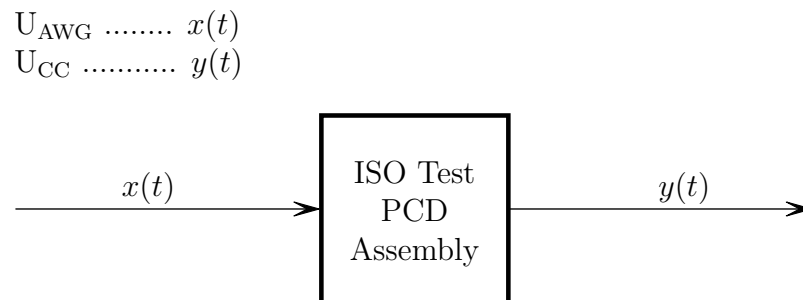


Figure 6.4: Simplified system for shaping the U_{PICC} voltage, with U_{AWG} as input signal $x(t)$ and U_{CC} as output signal $y(t)$

A linear chirp signal with a certain range of frequencies is fed to the system as input, expressed mathematically as:

$$x(t) = A \Re\{\exp[j(2\pi f(t)t)]\}$$

Setting $A = 1$ and taking the real part results in a cosine chirp signal with zero phase delay and a constant amplitude:

$$x(t) = \cos(2\pi f(t)t) \tag{6.23}$$

Time and frequency domain representations of this signal are shown in fig. 6.5.

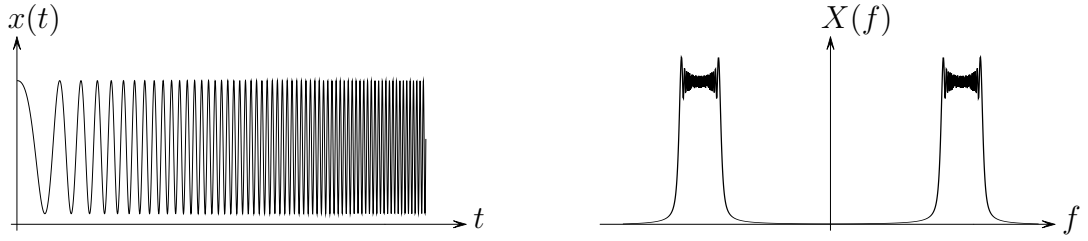


Figure 6.5: Input chirp signal $x(t)$, representing the voltage U_{AWG} , with its corresponding spectrum $X(f)$

Considering that this section is meant to abstractly describe the theory behind the shaping of U_{PICC} , the variable and parameter values are not required to be specified. However, it is required that the input chirp $x(t)$ has a range of frequencies that contains the 13.56 MHz component. From the actual system's point of view, this is important because the PCD circuit is impedance matched at exactly 13.56 MHz. Consequently, the other frequency components present in the chirp signal shall suffer a certain degree of mismatch, which has an effect on the system response at the calibration coil output. This output voltage U_{CC} is a chirp signal with the same frequency components as U_{AWG} , but with a certain phase delay and with mentioned variations in amplitude. Fig- 6.6 depicts the U_{CC} voltage in signal form, both in time and frequency domain, denoted as output $y(t)$ and its spectrum $Y(f)$, respectively.

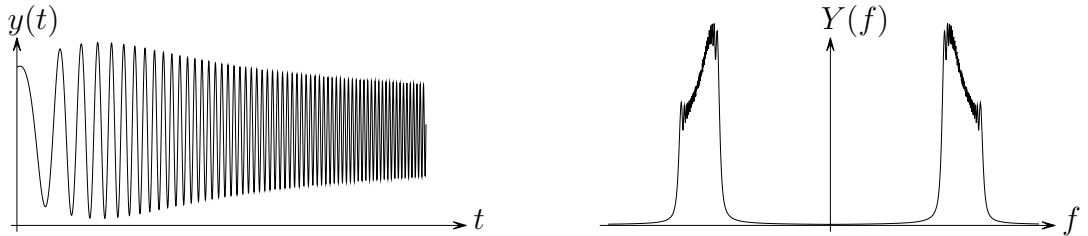


Figure 6.6: Output chirp signal $y(t)$, representing the voltage U_{CC} , with its corresponding spectrum $Y(f)$

Mathematically, $y(t)$ can be expressed as:

$$y(t) = B(t) \cos(2\pi f(t)t) \quad (6.24)$$

where $B(t)$ is the envelope varying in time, shown in fig. 6.7.

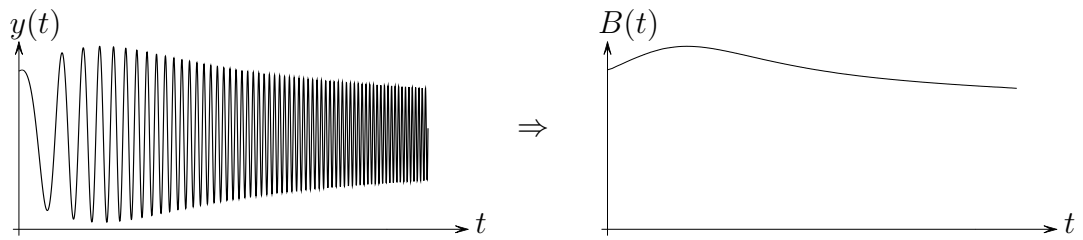


Figure 6.7: Output chirp envelope $B(t)$

The system output $y(t)$ also features a certain phase delay from $x(t)$, which shall be neglected for now in order to simplify the assumptions that are about to follow.

The premise of shaping the voltage U_{CC} is to modify the input voltage U_{AWG} in a way that it behaves as the inverse system response, so that the modified U_{AWG} and the effect of the ISO test assembly on the U_{CC} output would negate one another, resulting in a constant amplitude envelope for the output U_{CC} .

In signal form, this corresponds to multiplying the $x(t)$ signal with $B^{-1}(t)$, which is the inverse of envelope $B(t)$, so that $B^{-1}(t)$ and $B(t)$ would cancel each other out when the modified signal $x_{NEW}(t)$ is fed into the system. The resulting output $y_{NEW}(t)$ would then have the desired constant envelope amplitude, as shown in fig. 6.8.

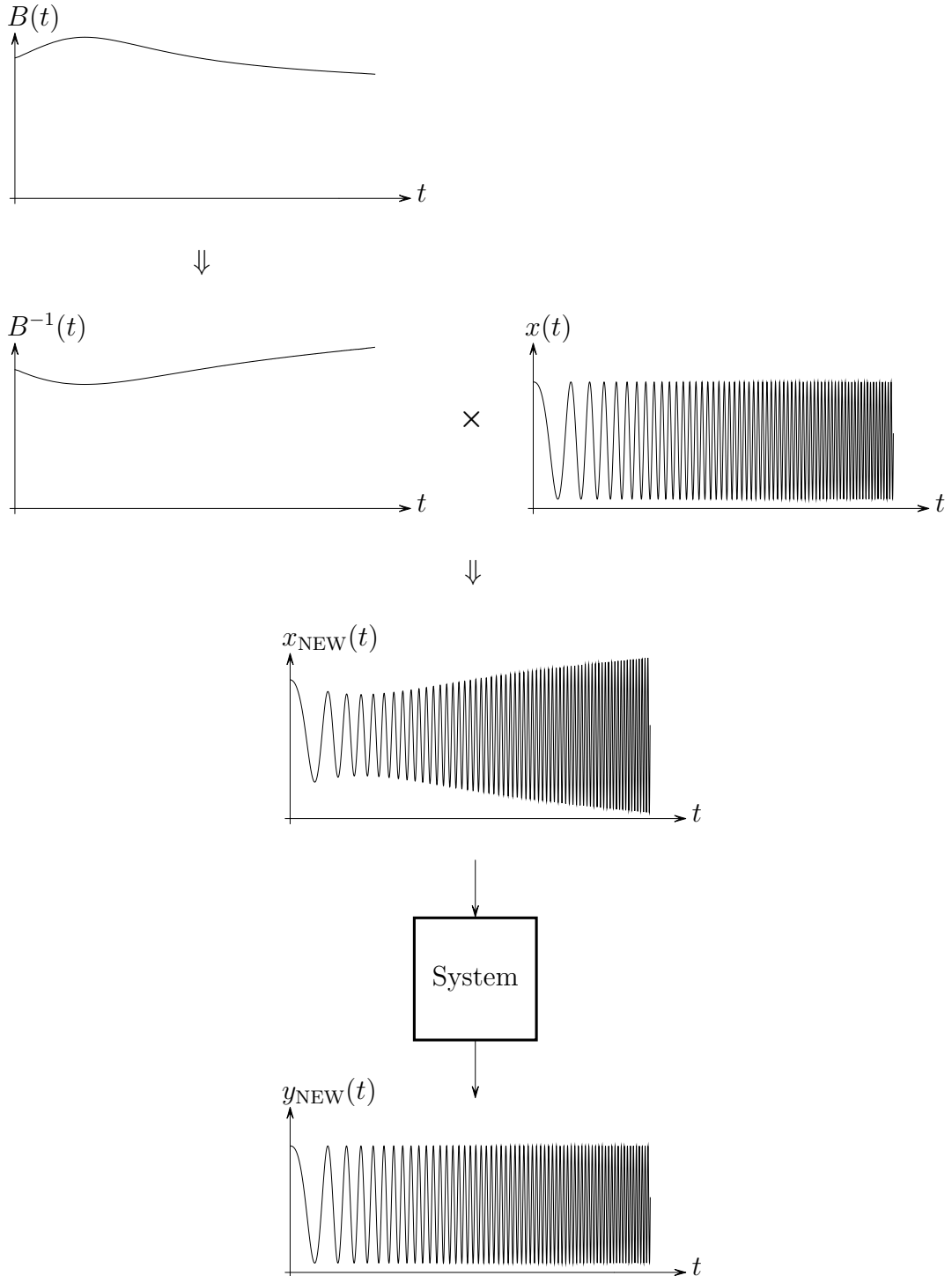


Figure 6.8: Shaping of $x(t)$ with the inverse envelope $B^{-1}(t)$

In order to construct its inverse, the envelope $B(t)$ of U_{CC} first needs to be acquired, which can be done using the method of complex down-modulation. A frequency shift of a signal can be achieved by multiplication with a complex exponential function in time domain. Consider a complex chirp signal of the form:

$$x_{\text{C}}(t) = \exp[j(2\pi f(t)t)] \quad (6.25)$$

and its complex conjugate:

$$x_{\text{C}}^*(t) = \exp[-j(2\pi f(t)t)] \quad (6.26)$$

The $x_{\text{C}}(t)$ signal is a complex exponential chirp so that the $x(t)$ signal from eq. 6.23 represents its real part. Being a complex signal, $x_{\text{C}}(t)$ has a one sided spectrum, whereas its complex conjugate $x_{\text{C}}^*(t)$ has a symmetric spectrum with only negative frequency components. Both spectra, $X_{\text{C}}(f)$ and $X_{\text{C}}^*(f)$, are shown in fig. 6.9.

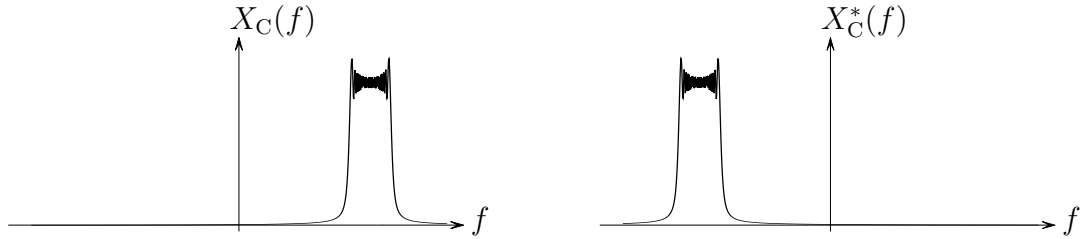


Figure 6.9: Spectrum of complex chirp $x_{\text{C}}(t)$ and its complex conjugate $x_{\text{C}}^*(t)$

A multiplication of the output signal $y(t)$ by either $x_{\text{C}}(t)$ or $x_{\text{C}}^*(t)$ in time domain corresponds to convolution in frequency domain. This results in shifting of the spectrum $Y(f)$ by the range of frequencies contained in the chirp, direction of the shift depending on whether $x_{\text{C}}(t)$ or $x_{\text{C}}^*(t)$ is used. In this case, $Y(f)$ is convolved with $X_{\text{C}}^*(f)$, so spectrum $Y(f)$ is shifted towards negative frequencies, the positive side of $Y(f)$ to baseband, and the negative side to twice the range of $Y(f)$. The result is a down-modulated version of $Y(f)$, denoted as $Y_{\text{MOD}}(f)$. However, only the baseband component $Y_{\text{BB}}(f)$ of $Y_{\text{MOD}}(f)$ is of interest, as it corresponds to the envelope $B(t)$, and it can be extracted by filtering out the unwanted negative frequency components. A 3rd order Butterworth low-pass filter is applied on $Y_{\text{MOD}}(f)$ in this case, which leaves only the envelope spectrum $Y_{\text{BB}}(f)$. Fig. 6.10 shows the down-modulation of the U_{CC} signal $y(t)$ in frequency domain, followed by low-pass filtering in order to obtain the envelope spectrum $Y_{\text{BB}}(f)$.

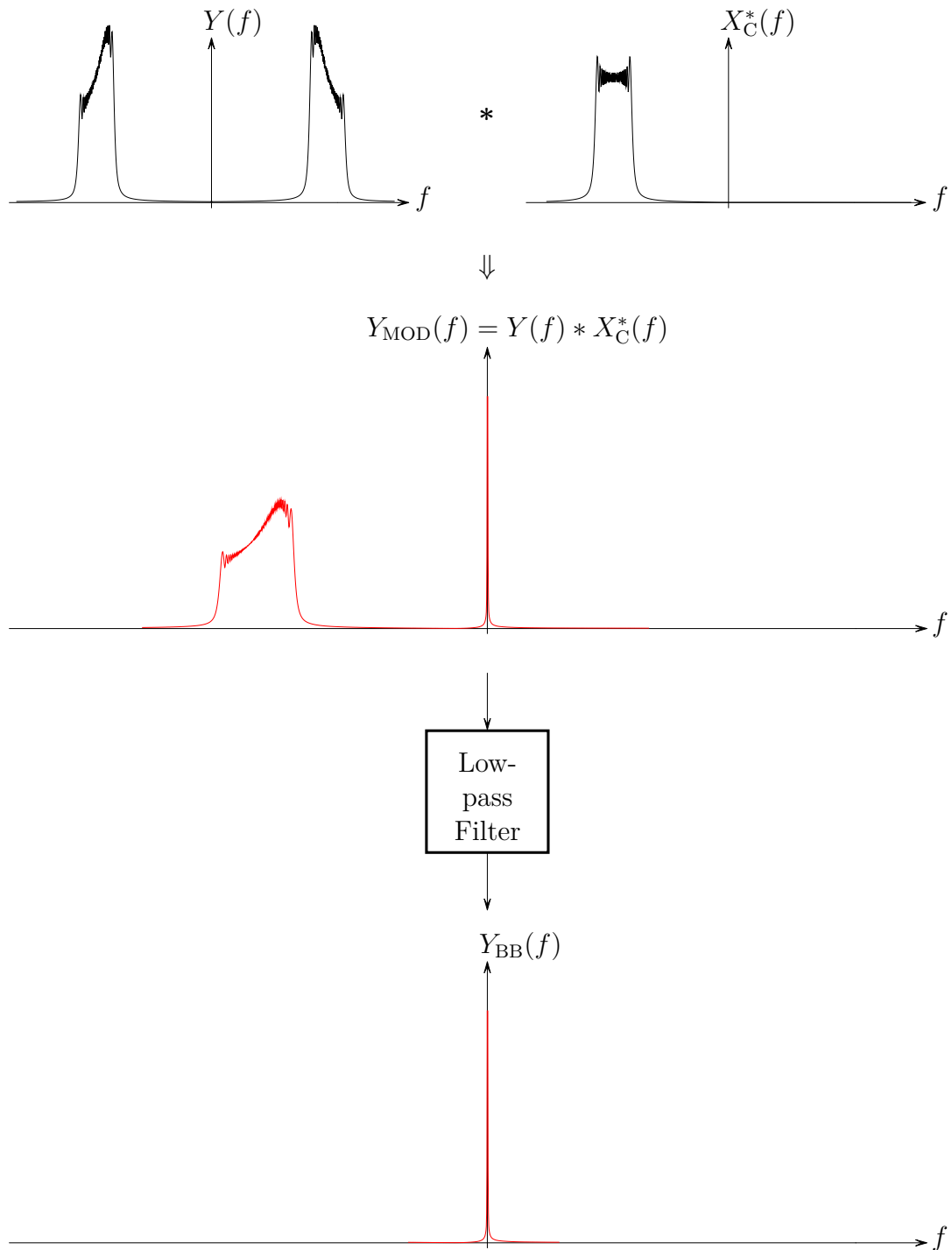


Figure 6.10: Down-modulation of $Y(f)$ with a complex exponential $X_C^*(f)$

The baseband spectrum $Y_{\text{BB}}(f)$ represents the desired envelope $B(t)$ in frequency domain, as shown in fig. 6.11.

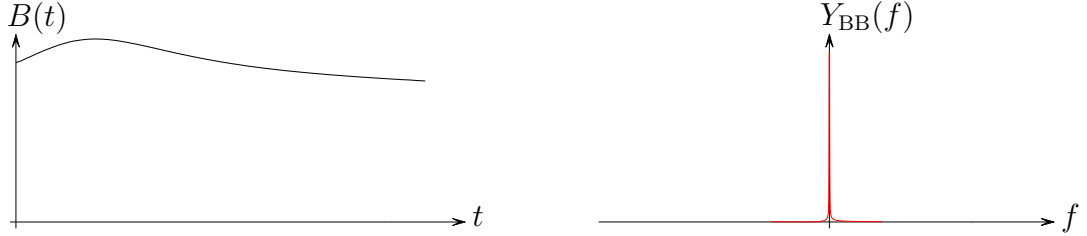


Figure 6.11: Envelope $B(t)$ and its spectrum $Y_{\text{BB}}(f)$

The acquired envelope $B(t)$ is subsequently inverted and multiplied with the initial input signal $x(t)$ from eq. 6.23, as already shown in fig. 6.8. The result is a shaped input signal $x_{\text{NEW}}(t)$, expressed mathematically as:

$$x_{\text{NEW}}(t) = B^{-1}(t)x(t) = B^{-1}(t) \cos(2\pi f(t)t) \quad (6.27)$$

where $B(t)^{-1}$ is the inverse envelope of the output signal $y(t)$. This shaped input signal $x_{\text{NEW}}(t)$ undergoes the system response of the test PCD assembly which results in the desired constant envelope $y_{\text{NEW}}(t)$ at the U_{CC} output. Because U_{PICC} is proportional to U_{CC} , the shaping of U_{PICC} is therefore achieved. The entire shaping procedure is shown again in fig 6.12.

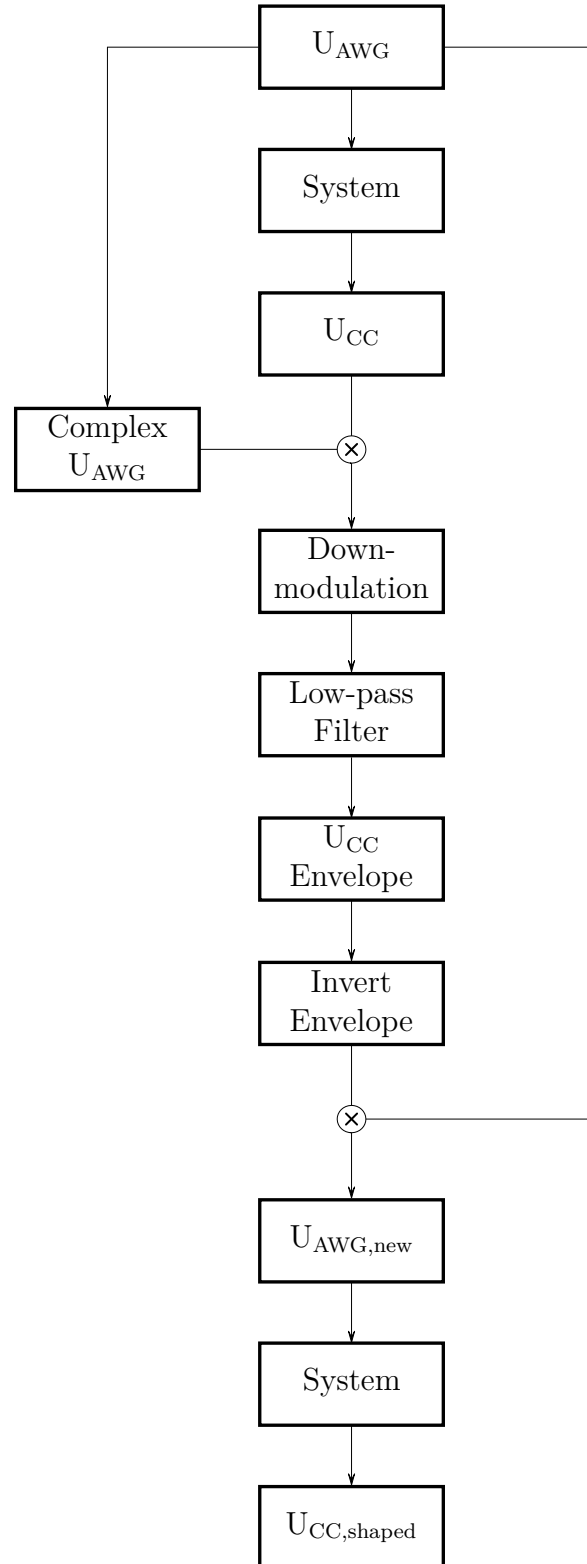


Figure 6.12: Block diagram for the shaping of U_{CC}

6.4 $U_{SC} \rightarrow I_{PICC}$ Transfer Function

Beside U_{CC} , the ISO test PCD assembly also allows differential voltage U_{SC} to be observed, which is the output of interest in this section. As described in chapter 4, the signal U_{SC} implicitly represents the current in the PICC. However, this assumption is not entirely accurate, because circuit components in the sense coils, as well as the oscilloscope probe, have an influence on the amplitude and phase of U_{SC} . These effects can be taken into consideration by estimating the transfer function between I_{PICC} and U_{SC} . The transfer function $H(s)$ has U_{SC} as its input and produces I_{PICC} as the output, which is the signal required for the extended method. Simplified description of this assumption is shown in fig. 6.13.

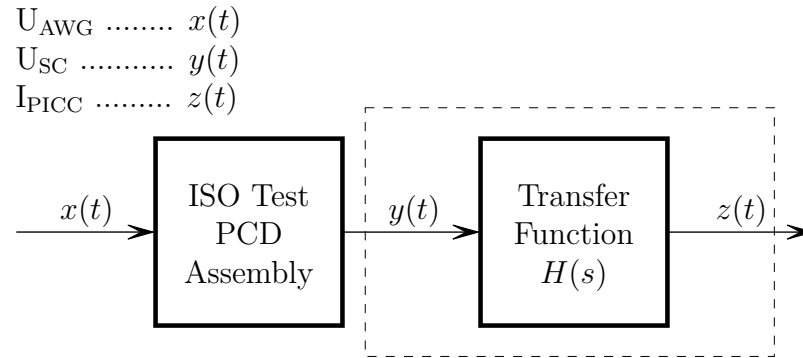


Figure 6.13: Simplified system for obtaining I_{PICC} using the transfer function $H(s)$, with U_{SC} as input signal $y(t)$ and I_{PICC} as output signal $z(t)$

The transfer function $H(s)$ can be modeled based on the system shown in fig. 6.14, which shows the PICC, both sense coils, and the equivalent capacitance and resistance of the oscilloscope probe.

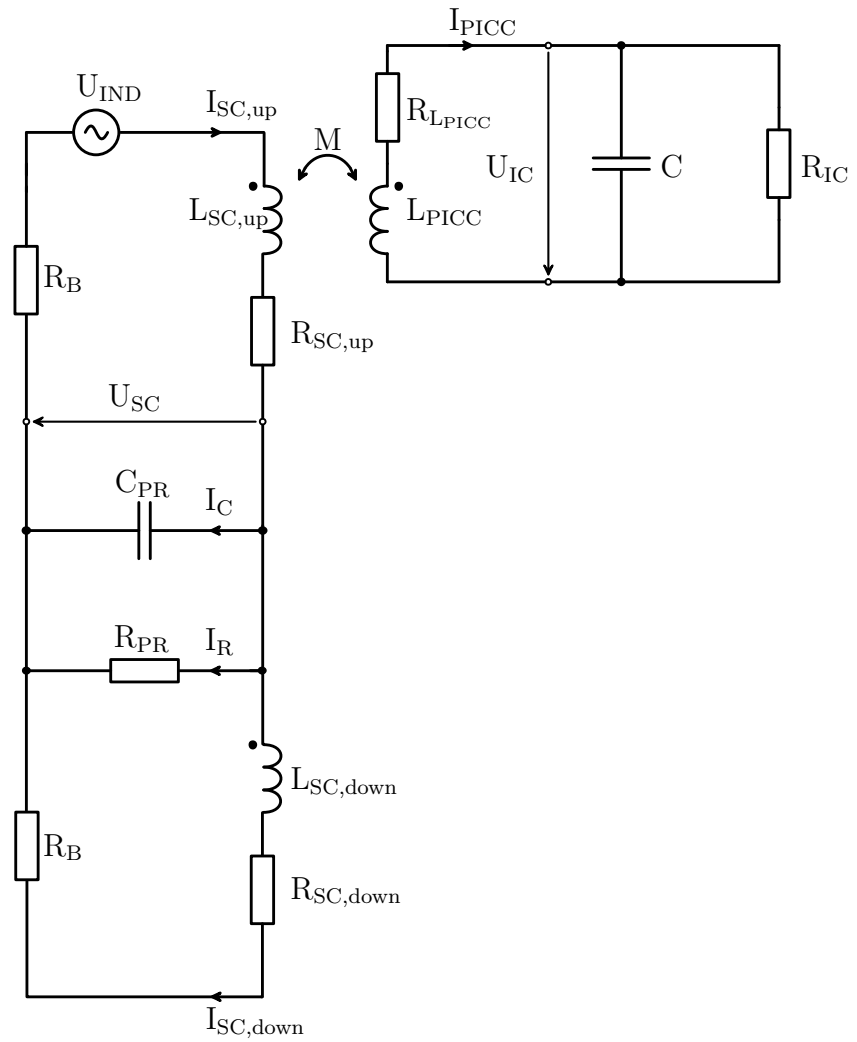


Figure 6.14: Equivalent circuit for determining $H(s)$ involves both sense coils and a PICC, adapted from [5]

6.4 $U_{SC} \rightarrow I_{PICC}$ Transfer Function

The components that are depicted are relevant for estimating $H(s)$, which explains the absence of PCD and calibration coil from the system. The only coupling shown is between PICC and upper sense coil, whereas the one between PICC and lower sense coil is neglected because the coupling coefficient $k_{SC,down}$ is negligibly small. For the purpose of modeling $H(s)$ it is therefore assumed that no voltage is induced by the PICC in the lower sense coil. The total voltages $U_{SC,up}$ and $U_{SC,down}$ induced in both sense coils are represented through the voltage induced by the PICC in the upper sense coil, denoted as U_{IND} . According to chapter 4, U_{IND} is given by subtracting $U_{SC,up}$ and $U_{SC,down}$:

$$U_{IND} = U_{SC,up} - U_{SC,down} \quad (6.28)$$

Therefore, U_{IND} represents the voltage induced by current I_{PICC} through mutual inductance M :

$$\underline{U}_{IND} = j\omega M \underline{I}_{PICC} \quad (6.29)$$

Referring to fig. 6.14, $H(s)$ can be derived from the following equations:

$$\text{I :} \quad \underline{U}_{IND} = \underline{I}_{SC,up}(j\omega L_{SC,up} + R_{SC,up} + R_B) + \underline{U}_{SC}$$

$$\text{II :} \quad \underline{U}_{SC} = \underline{I}_{SC,down}(j\omega L_{SC,down} + R_{SC,down} + R_B)$$

$$\text{III :} \quad \underline{U}_{SC} = \underline{I}_R R_{PR}$$

$$\text{IV :} \quad \underline{I}_{SC,up} = \underline{I}_C + \underline{I}_R + \underline{I}_{SC,down}$$

$$\text{V :} \quad \underline{I}_C = j\omega C_{PR} \underline{U}_{SC}$$

Together with eq. 6.29, the final expression for $H(s)$ is given as:

$$H(s) = \frac{(sL_{SC,up} + R_{SC,up} + R_B) \left(sC_{PR} + \frac{1}{R_{PR}} + \frac{1}{sL_{SC,down} + R_{SC,down} + R_B} \right) + 1}{sM} \quad (6.30)$$

$H(s)$ given in eq. 6.30 is in fact an improper transfer function, because it has more zeros than poles and is therefore not stable at certain frequencies. However, the used range of frequencies is a sweep around 13.56 MHz, the same as in the chirp signal, where $H(s)$ shows stable behavior. Bode plot of $H(s)$ is shown in fig. 6.15.

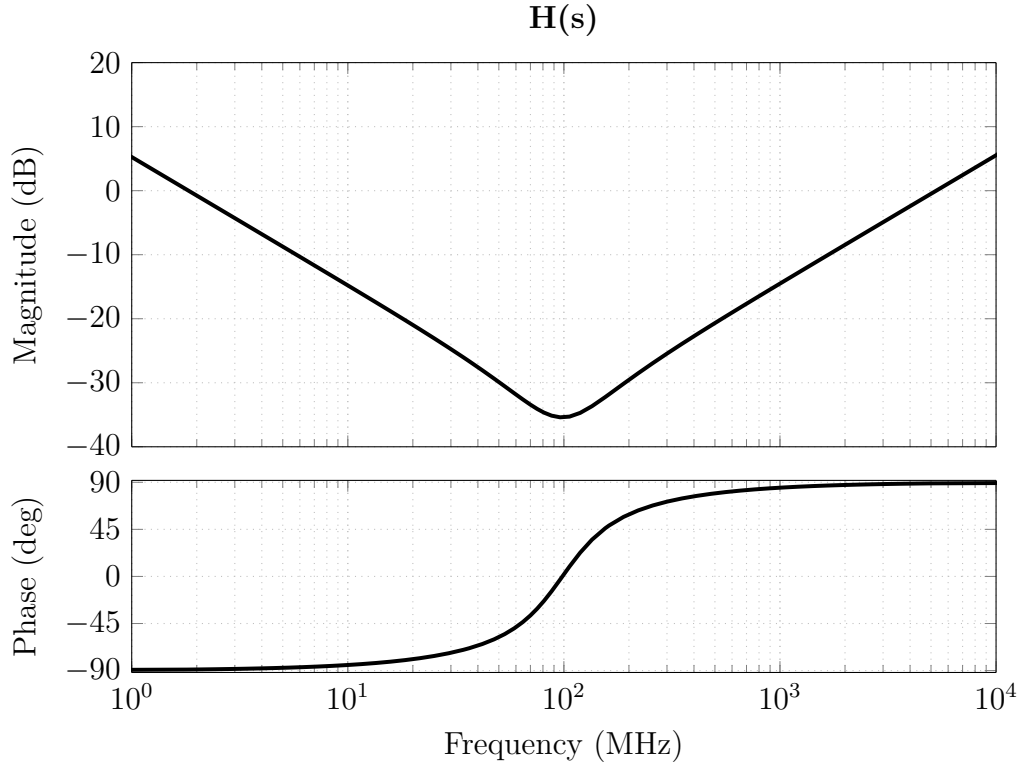


Figure 6.15: Bode plot of $H(s)$

In general, this model is not ideal because, beside assuming $k_{SC,down}=0$, it also neglects the parasitic capacitances of the PCD and both sense coils. Nevertheless, $H(s)$ shows that the relationship between differential voltage U_{SC} and the current I_{PICC} is not merely given by $U_{SC} = j\omega M I_{PICC}$, but rather depends on several other factors as well.

Applying the transfer function on U_{SC} input enables I_{PICC} to be determined as output, which along with shaping of U_{PICC} fulfills another prerequisite for determining the relative active power P_{REL} .

6.5 Phase Angle φ

With a constant envelope U_{PICC} and I_{PICC} obtained using the transfer function $H(s)$, the remaining element for determining P_{REL} is the phase angle φ between phasors $\underline{U}_{\text{PICC}}$ and $\underline{I}_{\text{PICC}}$. As mentioned in section 6.2, U_{PICC} and U_{CC} have the same phase characteristics, because both voltages are induced simultaneously by the PCD. In case of linear chirp signals frequency changes linearly over time, which means that the phase is quadratic, defined as the integral of the instantaneous frequency. Therefore, the phase angle of U_{PICC} is set as reference, and the angle φ is expressed as relation of I_{PICC} to this reference by subtracting the two phase angles:

$$\varphi = \arg(\underline{I}_{\text{PICC}}) - \arg(\underline{U}_{\text{PICC}}) \quad (6.31)$$

The phase angle φ based on the U_{PICC} and I_{PICC} phasors is shown again in fig. 6.16.

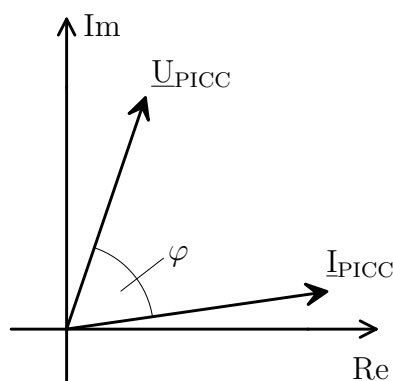


Figure 6.16: Phasor representation of the phase angle φ

After obtaining φ , the relative active power P_{REL} is ready to be determined.

6.6 Determining Resonance Frequency from P_{REL}

The relative active power P_{REL} is determined according to the following expression:

$$P_{REL} = I_{PICC} \cos(\varphi) \quad (6.32)$$

Both I_{PICC} and U_{CC} signals are down-modulated so that I_{PICC} can be interpreted as magnitude of the I_{PICC} phasor. The complex down-modulation enables the phase information to be acquired as well, so that the phase angle φ can be easily determined by subtracting the two phase characteristics as shown in eq. 6.31. Taking the cosine of φ represents calculating the real part of the complex apparent power phasor \underline{S} . Main premise of the extended method is that resonance frequency f_{RES} is defined for P_{REL} at its maximum, and in order to obtain f_{RES} there are several signal processing steps that need to be applied.

The P_{REL} signal from eq. 6.32 stems from the two signals observable by the ISO test PCD assembly: U_{CC} and U_{SC} . These signals share the same linear frequency sweep characteristics as the input chirp signal U_{AWG} . Therefore, the maximum of P_{REL} can be assigned to an appropriate point in time belonging to either of the two signals, although U_{CC} is the slightly preferred option because it has a constant amplitude spectrum. Based on a portion of the signal chosen accordingly, f_{RES} is determined from P_{REL} as shown in fig. 6.17.

Mapping $P_{REL,max}$ to a point in time corresponding to the signal U_{CC} presents no obstacle in the actual signal processing implementation, because P_{REL} has the same number of indexes as U_{CC} , provided that no decimation or extrapolation is performed. This means that the indexes of P_{REL} inherently correspond to the time samples of U_{CC} . A certain number of U_{CC} values left and right from the observed point in time are subsequently cut ($U_{CC,cut}$). Zero padding and windowing are performed before FFT is applied onto the $U_{CC,cut,windowed}$ signal. The spectral peak corresponds to the instantaneous frequency at $P_{REL,max}$, which is the desired resonance frequency f_{RES} . Obtaining f_{RES} concludes the final step of the extended method. To summarize, the entire procedure is shown as a block diagram in fig. 6.18.

6.6 Determining Resonance Frequency from P_{REL}

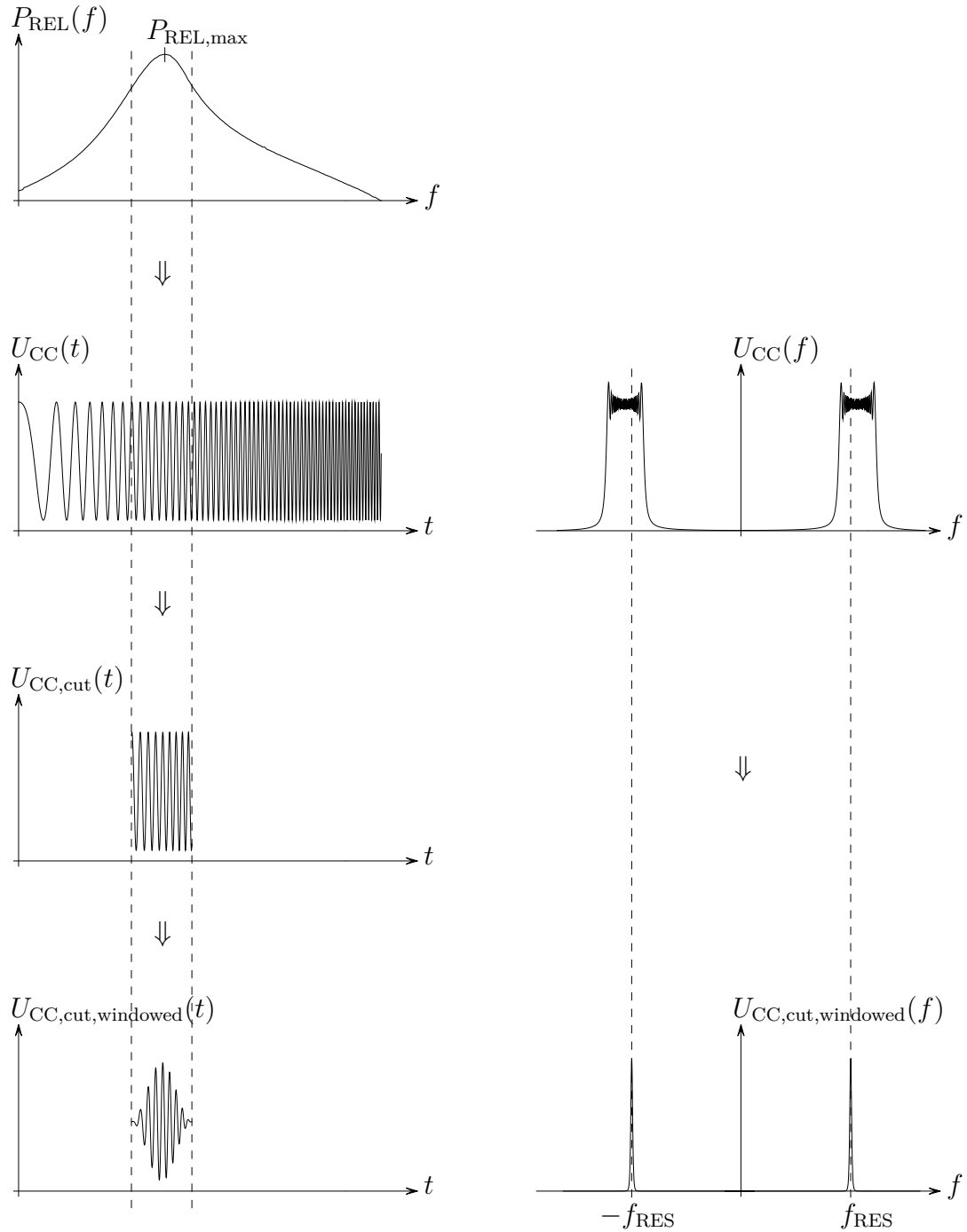


Figure 6.17: Obtaining f_{RES} from P_{REL}

6.6 Determining Resonance Frequency from P_{REL}

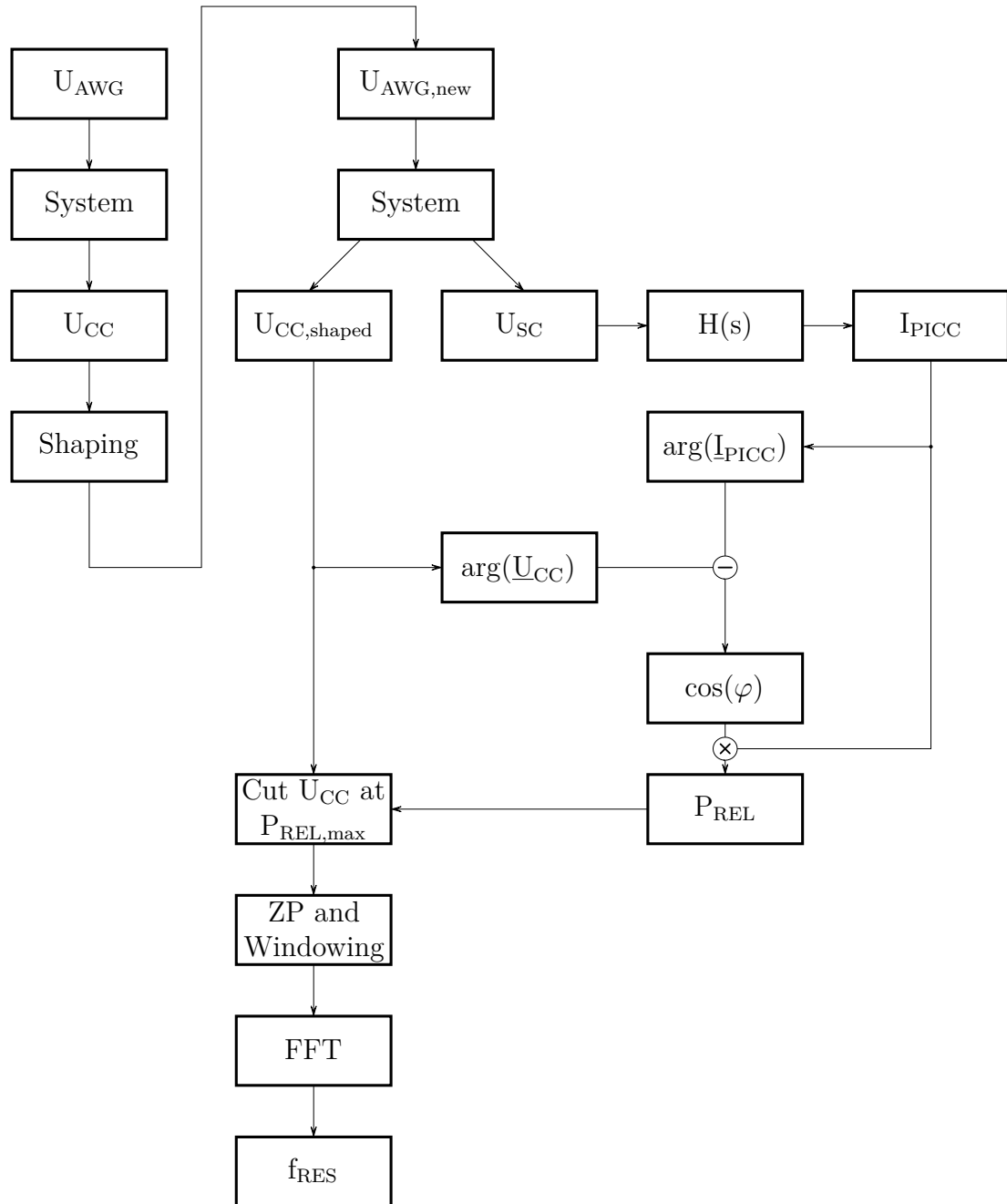


Figure 6.18: Block diagram of the extended method

Chapter 7

Extended Method in a Simulation Environment

Developing a coherent model for simulation is required in order to grasp the concepts used in the extended method, while simultaneously maintaining a certain degree of abstraction. That way, despite refraining from an actual implementation of the measurement, it is possible to observe how a resonance frequency measurement would take place when performed on an ISO test PCD assembly used in a standardized measurement setup.

This chapter gives a step-by-step description of the extended method performed in a simulation environment. Considering the fact that all measurement data originates from simulation, some simplification is assumed, particularly by neglecting IC nonlinearities, noise, and measurement uncertainties of devices used in actual measurements. On the other hand, this allows the general idea of the extended method to step into the foreground, thus conserving a great deal of time in development of the method, as opposed to performing all measurement steps from start to finish in reality. In addition, successfully performing a simulated measurement on a system with a predetermined resonance frequency would confirm the feasibility of the extended method.

7.1 Simulation of the PICC

Prior to modeling the entire system, the expressions concerning the definition of resonance frequency for the extended method (chapter 6) are simulated for the simplified circuit of a PICC (fig. 4.5). An AC simulation is performed with a range of frequencies from 1 MHz to 40 MHz while the voltage source U_{PICC} is held constant at 1 V. The values of PICC circuit parameters are taken from ta-

ble 7.2. Following variables are thereby computed: $U_{IC}(f)$, $P_{IC}(f)$, and $P_{PICC}(f)$. Fig. 7.1 shows the magnitudes of these variables normalized around their maximum values. In addition, the real part of the transformed impedance Z_T is also included in the plot in order to illustrate the comparison with the VNA method. The reason why Z_T was simulated instead of Z_{VNA} is because Z_{VNA} locus curve has the same form as Z_T locus curve, only shifted in the complex plane by the VNA measuring coil parameters, as explained in chapter 5. Furthermore, it is reasonable to observe how Z_T itself behaves compared to the other variables. The two remaining parameters necessary for obtaining Z_T (eq. 4.7), the PCD antenna inductance L_{PCD} and the coupling coefficient k , are taken from tab. 7.2 as well.

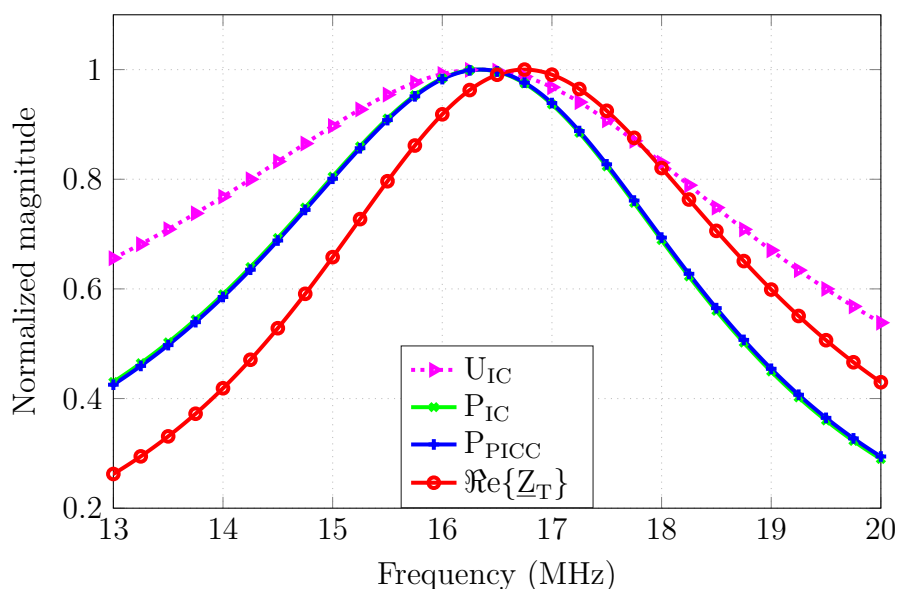


Figure 7.1: AC analysis in the PICC showing maximum values of the quantities used in different definitions of f_{RES}

It can be seen that the maximum of U_{IC} and the maxima of the two active power quantities P_{IC} and P_{PICC} are essentially coinciding with one another, which means that in this case all of them approximately correspond to the same resonance frequency. On the other hand, the maximum of $\Re\{Z_T\}$ can be seen to substantially differ from the rest. For the case of resistance $R_{LPICC}=2.4\ \Omega$, which is significantly lower than IC resistance $R_{IC}=800\ \Omega$, the P_{IC} and P_{PICC} curves are nearly overlapping, thus confirming the premise of using P_{PICC} for definition of f_{RES} by the extended method. For comparison, fig. 7.2 depicts how the active power quantities behave when the condition 6.16 is not fulfilled, after setting a ten times higher value ($24\ \Omega$) for R_{LPICC} .

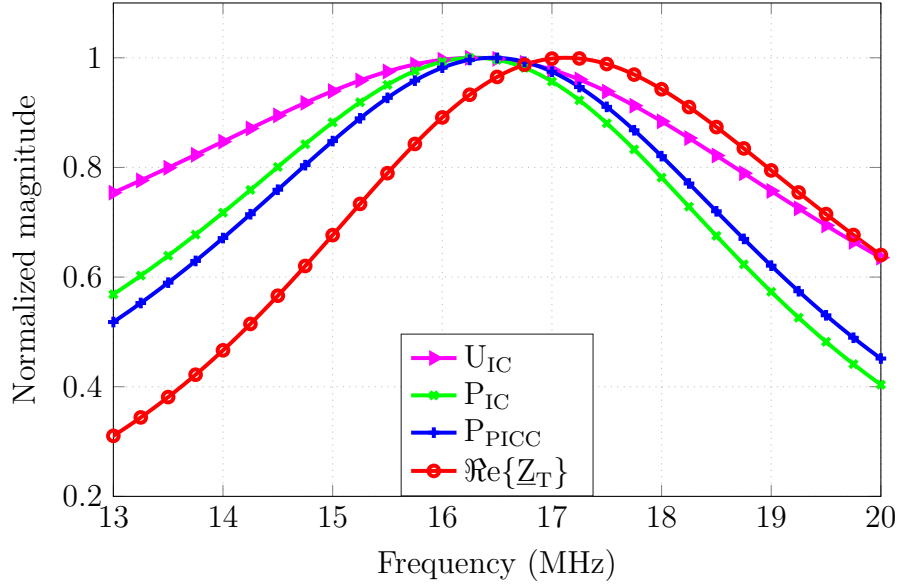


Figure 7.2: AC analysis in the PICC when condition 6.16 is not fulfilled

The P_{PICC} curve in fig. 7.2 now deviates from the P_{IC} curve that still shares the same maximum with voltage U_{IC} . Therefore, in this case the extended method cannot be applied with high accuracy.

Reverting back to the previous case where $R_{L_{PICC}}$ satisfies the condition 6.16, maximum values of the variables from fig. 7.1 are mapped to their corresponding frequencies, which are given in table 7.1. Resonance frequency obtained by the Thomson equation is included as well. One notices how f_{RES} defined by the extended method at $P_{PICC,max}$ is much closer to the “true” f_{RES} defined at $P_{IC,max}$ than it is the case with f_{RES} defined by the VNA method at $\Re\{Z_T\}_{max}$.

Another point of view useful for comparing the two measurement methods can be seen in fig. 7.3, where a polar representation of the transformed impedance Z_T is shown for the range of frequencies between 1 MHz and 40 MHz. In addition, depicted are the values of Z_T at the frequencies from table 7.1, along with the

Table 7.1: Different resonance frequencies obtained in the AC simulation

Definition of f_{RES}	(MHz)
$U_{IC,max}$	16.3361
$P_{IC,max}$	16.3361
$P_{PICC,max}$	16.3490
$\Re\{Z_T\}_{max}$	16.7488
Thomson eq.	16.7108

frequency at which \underline{Z}_T is real (phase resonance). In order to find the phase resonance frequency, the phase angle of \underline{Z}_T must be equal to zero, which is computed simply by finding the minimum value of the phase angle, denoted as $\arg(\underline{Z}_T)_{\min}$.

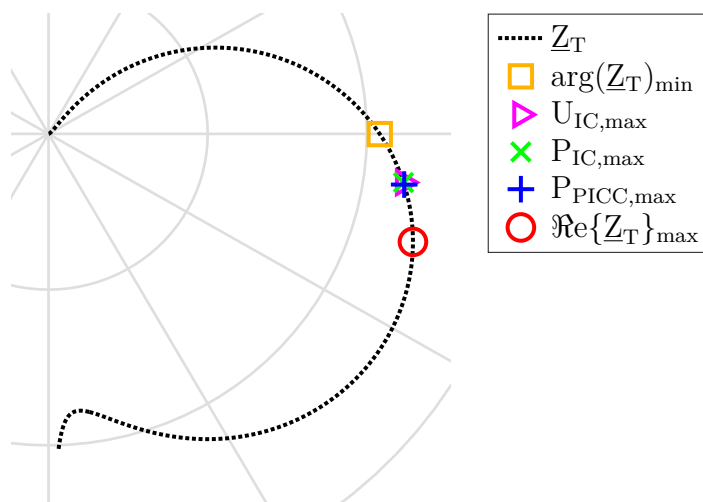


Figure 7.3: Polar representation of \underline{Z}_T at the frequencies from table 7.1 for $R_{IC}=800\ \Omega$

Discrepancy between $\Re\{\underline{Z}_T\}_{\max}$ and $P_{PICC,\max}$, defined by the two measurement methods, is clearly visible. The disadvantage of the VNA method is somewhat reduced when condition 5.7 is exaggerated, i.e. when R_{IC} takes on a significantly higher value. Fig. 7.4 shows the same simulation, with an exception that R_{IC} is increased from $800\ \Omega$ to $5\ \text{k}\Omega$.

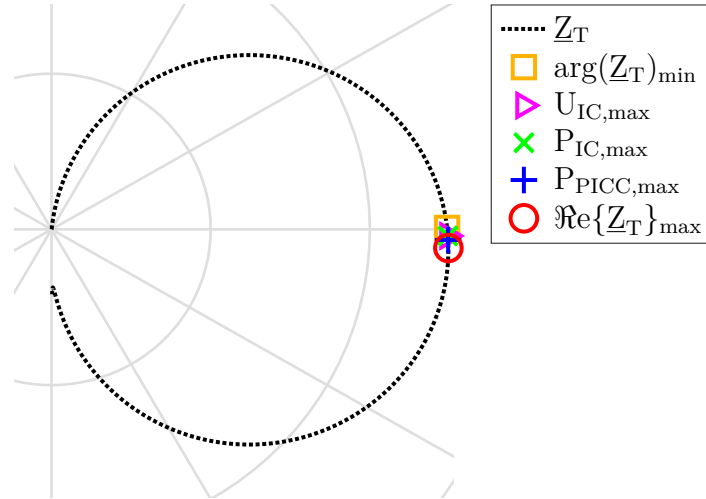


Figure 7.4: Polar representation of \underline{Z}_T after setting $R_{IC}=5\text{ k}\Omega$

In this case, the resonance frequency of the VNA method is considerably closer to the other resonance frequencies, thereby justifying the use of this method in cases where R_{IC} reaches high values.

7.2 The System Model

Similar to expanding the theoretical considerations from just the PICC onto the entire system, the upcoming task is to construct a model that can fully simulate the measurement procedure of the extended method. Software used for this model is Advanced Design System (ADS) by Agilent Technologies, a standard software tool used in RF engineering. One of the hallmarks of ADS is the ability to “tune” various circuit parameters in the simulation and instantly see the consequences in processing the simulated data, thus reducing the effort for example in impedance matching of the parameters and generally providing more insight on the overall system behavior.

The simulation model embodies the circuit of the entire system used for the extended method (fig. 4.15). Therefore, circuit representations of the AWG, the ISO test PCD assembly, the PICC, as well as of the oscilloscope probes are all incorporated in the model. Table 7.2 shows the circuit parameters and coupling coefficients used for the model based on the equivalent circuit of the system (fig. 4.15). These values are obtained by measuring the circuit parameters of the same ISO test PCD assembly, PICC antenna, and oscilloscope probes that shall later be used in actual measurements. On the other hand, values of the IC do not represent the real behavior of commercial ICs (fig. 5.8) and are

Table 7.2: Circuit parameters and coupling coefficients used in the model based on fig. 4.15

Part of system	Parameter	Value	Unit
PCD	C_{MS}	91.38	pF
	C_{MP}	180	pF
	L_{PCD}	466.51	nH
	$R_{L_{PCD}}$	0.4	Ω
	R_{EXT}	4.7	Ω
PICC	L_{PICC}	2.2677	μ H
	$R_{L_{PICC}}$	2.4	Ω
	C	40	pF
	R_{IC}	800	Ω
Sense Coils	$L_{SC,up}$	435.98	nH
	$L_{SC,down}$	437.65	nH
	$R_{L_{SC,up}}$	0.7	Ω
	$R_{L_{SC,down}}$	0.7	Ω
	R_B	245	Ω
Calibration Coil	L_{CC}	250	nH
	$R_{L_{CC}}$	0.4	Ω
Oscilloscope Probes	C_{PR}	12	pF
	R_{PR}	2.2	$M\Omega$
Coupling Coefficients	$k_{PCD \leftrightarrow PICC}$	0.05745	
	$k_{PCD \leftrightarrow CC}$	0.04425	
	$k_{PCD \leftrightarrow SC,up}$	0.086	
	$k_{PCD \leftrightarrow SC,down}$	0.0848	
	$k_{PICC \leftrightarrow SC,up}$	0.17477	
	$k_{PICC \leftrightarrow SC,down}^*$	0.0164	

simply represented as a parallel connection of simple passive components (C and R_{IC}). This way, the focus can be maintained on the model of the system and the feasibility of the extended method, instead of trying to model the complex behavior of a commercial IC. If the simulation proves that the extended method is possible for passive components, next step would just be to implement the method in reality and measure the resonance frequency of commercial ICs.

Coupling coefficients between antenna coils are measured on the actual ISO test assembly and PICC antenna (using methods described in [3]), and their values are included in table 7.2. The coupling coefficient $k_{PICC \leftrightarrow SC, down}$ (denoted with a *) is also measured, although not included in the model because it was neither included in $H(s)$ for simplifying reasons. The advantage of modeling mutual inductances between coils allows the, in reality not directly measurable, $U_{SC} \rightarrow I_{PICC}$ transfer function and its effects to be observed in the simulations. This proved to be of significant assistance, because implicit numerical simulations of the transfer function in the ADS model enabled comparison with the analytically derived transfer function $H(s)$ (chapter 6).

7.2.1 Simulation of the Extended Method

Based on the developed model, it is possible to perform measurements with the extended method through a simulation. What follows is a series of simulated measurement steps according to the proposed theoretical concepts (chapter 6), acting as an interim stage between theory and reality.

Chirp Generation

The extended method proposes that an input signal with a constant envelope amplitude containing the desired range of frequency components should be fed into the system by an AWG. As these requirements are fulfilled by the signal given in eq. 6.23, a chirp signal of the same form is generated in MATLAB, with frequency components between 10 MHz and 20 MHz and duration of 20 μ s. Fig. 7.5 shows this U_{AWG} signal, both in time and frequency domain.

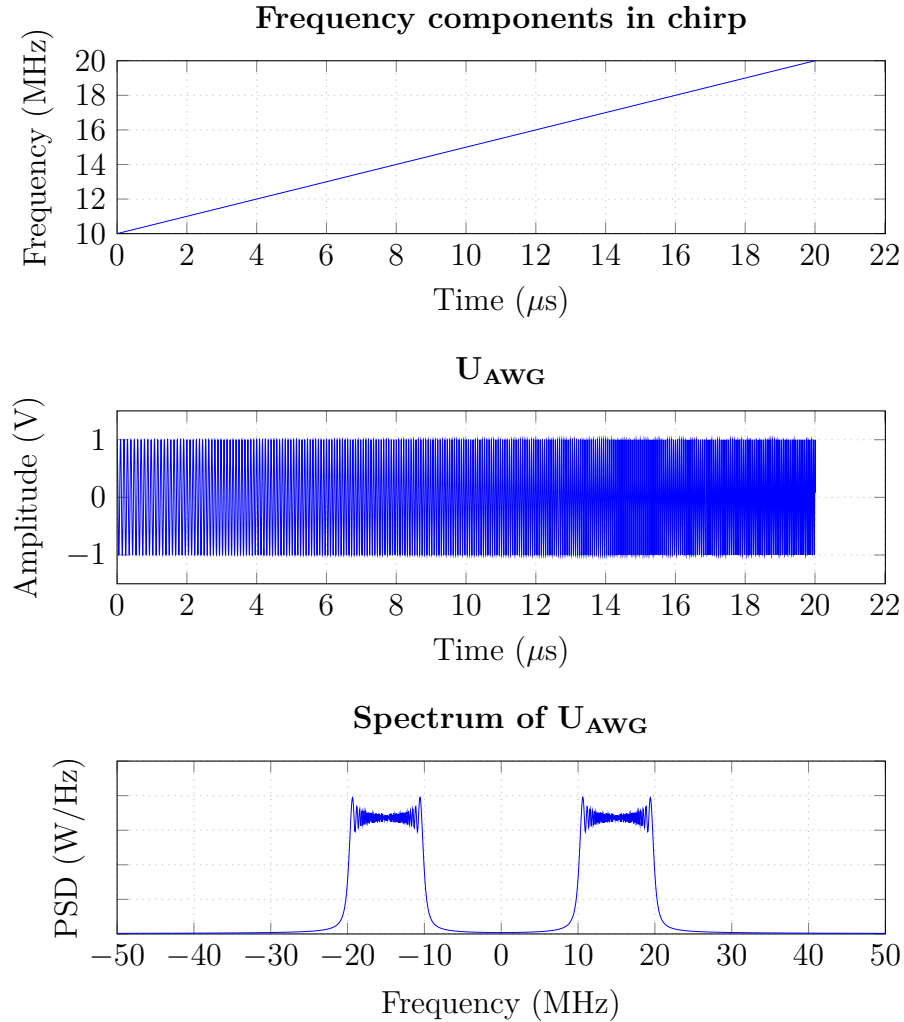


Figure 7.5: Input signal U_{AWG} for the simulation, along with its spectrum

The reason why such a short duration of the chirp is chosen is to reduce the simulation time. Considering how the IC is modeled by a simple parallel connection of passive components (C and R_{IC}), there should be no influence of the chirp duration on the simulated measurement. In reality, however, the chirp duration should be much longer (several ms) in order to take the behavior of an actual IC into account and neglect transient processes occurring in such short time spans.

According to section 6.3, a complex chirp signal of which U_{AWG} is the real part is required for down-modulation. Hence, this signal is also generated in MATLAB and its complex conjugate $\underline{U}_{\text{AWG,complex}}$ is taken so that its spectrum only has negative frequency components. Real and imaginary part of $\underline{U}_{\text{AWG,complex}}$,

including its spectrum are depicted in fig. 7.6.

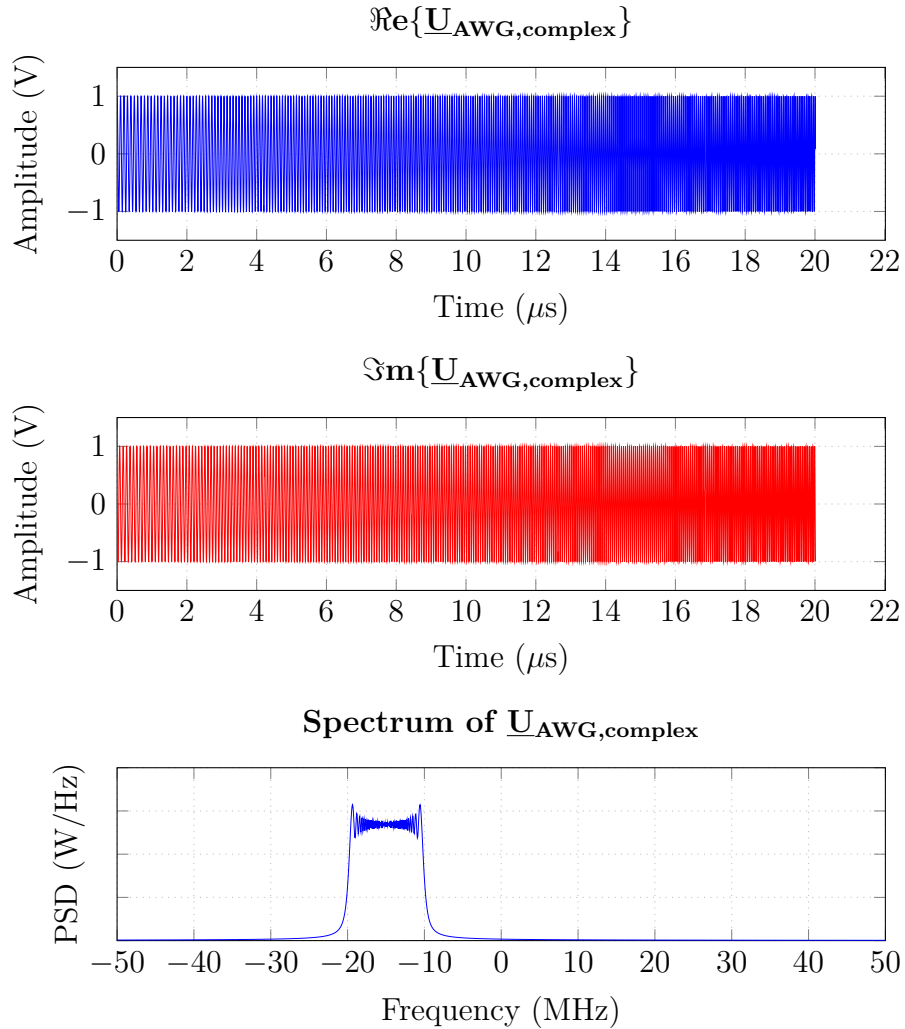


Figure 7.6: Complex conjugate signal $\underline{U}_{AWG,complex}$: its real part (U_{AWG} signal from fig. 7.5), followed by its imaginary part and spectrum

Shaping of U_{CC}

The U_{AWG} signal is sent to the model as input and a transient simulation of the system is performed. The expected simulation output signals are U_{CC} and U_{SC} . However, only U_{CC} is of interest at this point, as it is the only signal required for the shaping process. Fig. 7.7 depicts U_{CC} and its spectrum as the initial output, before shaping is carried out.

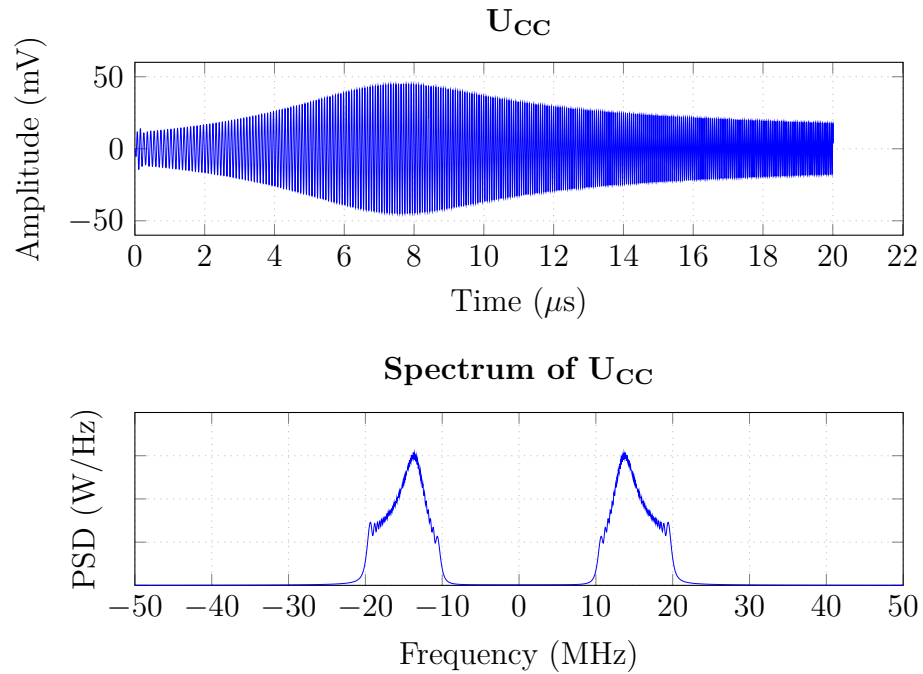


Figure 7.7: Simulation output signal U_{CC} with its spectrum, before shaping

Next, the shaping processing steps described in section 6.3 are performed on the U_{CC} signal. Firstly, down-modulation is performed using $\underline{U}_{AWG,complex}$ (fig. 7.6), followed by low-pass filtering to obtain the envelope, and finally multiplying the initial U_{AWG} with the inverted envelope to obtain the shaped input signal $U_{AWG,new}$. Time and frequency representations of signals used in the shaping process are depicted in fig. 7.8.

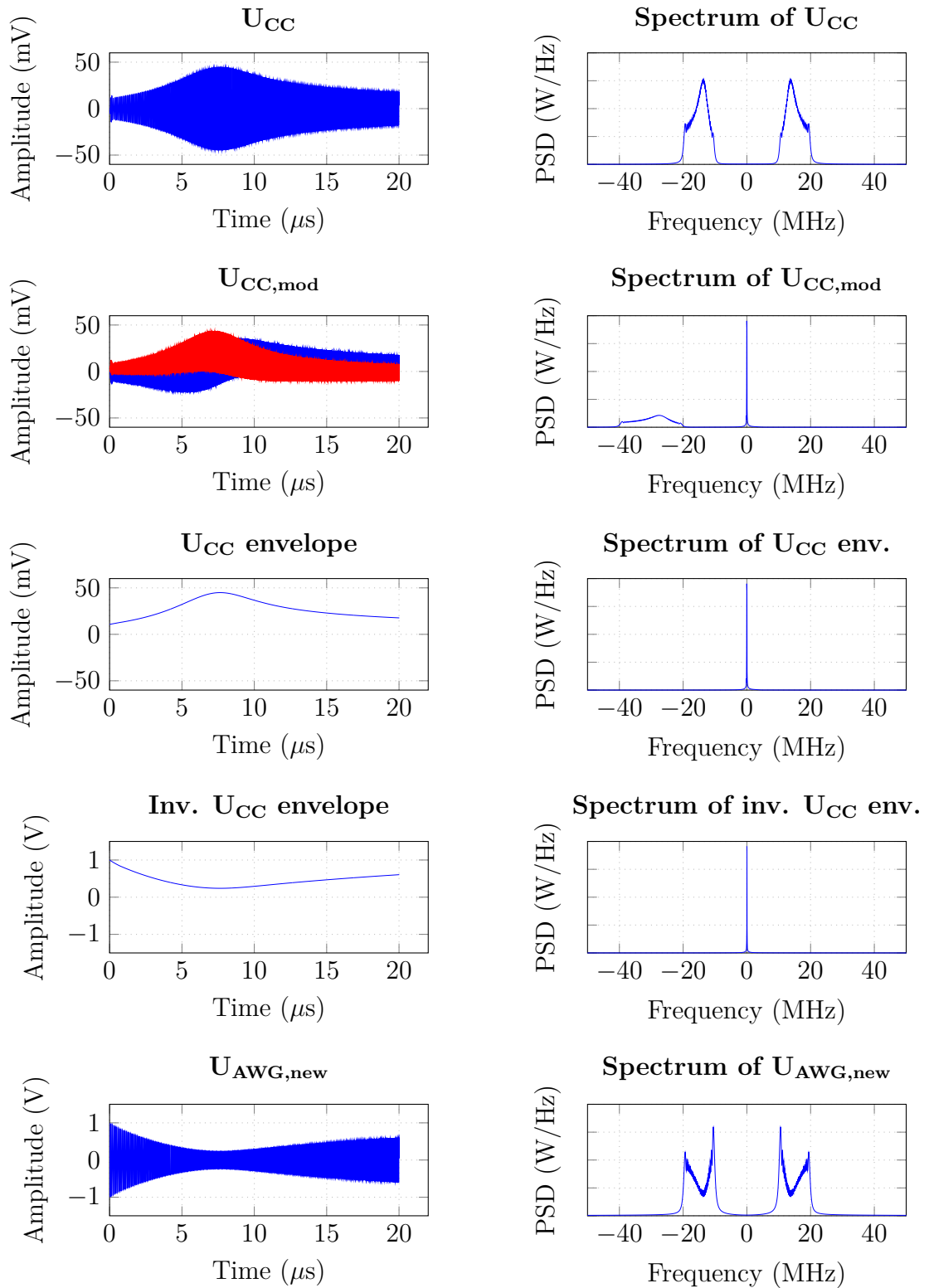


Figure 7.8: Simulation of the shaping process for U_{CC}

End result of the simulated shaping process is a new signal $U_{AWG,new}$ that is sent as input for the second transient simulation, for which both outputs ($U_{CC,shaped}$ and U_{SC}) are shown in fig. 7.9.

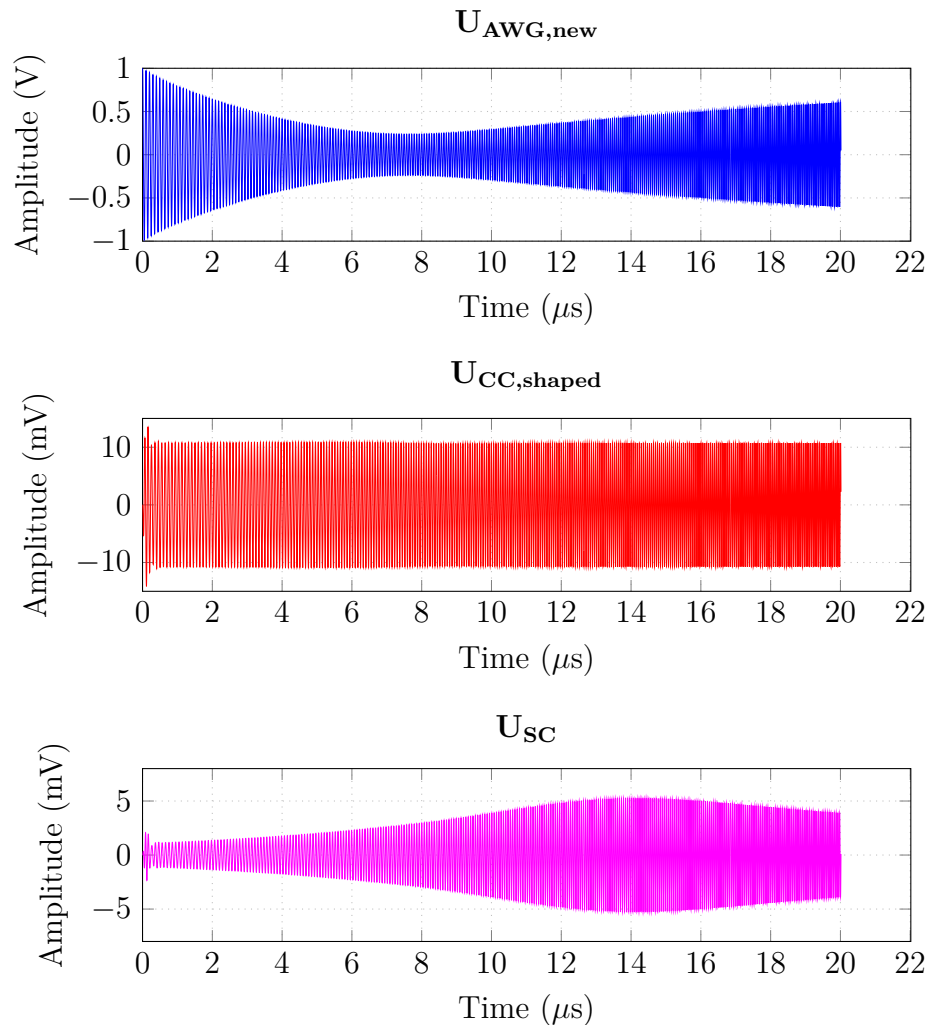


Figure 7.9: Shaped input signal $U_{AWG,new}$ for the second simulation that gives signals $U_{CC,shaped}$ and U_{SC} as outputs

Transfer Function $H(s)$

According to section 6.4, next step is to obtain the I_{PICC} current from U_{SC} by applying the appropriate transfer function $H(s)$. One of main advantages of the model is that any desired voltage or current in the circuit can be observed in an AC or transient simulation, including those that are not observable in a

real system, such as I_{PICC} . The software therefore implicitly applies a certain transfer function when performing numerical calculations in the simulation. In order to ascertain the validity of the software model, the analytically determined $H(s)$ (eq. 6.30) is compared with the implicit transfer function $H_{\text{model}}(s)$, which is extracted from the model as relation between U_{SC} and I_{PICC} . Fig. 7.10 shows Bode plots of both transfer functions in the range of frequencies relevant for the extended method, which is between 10 MHz and 20 MHz (the range of frequencies in the chirp signal).

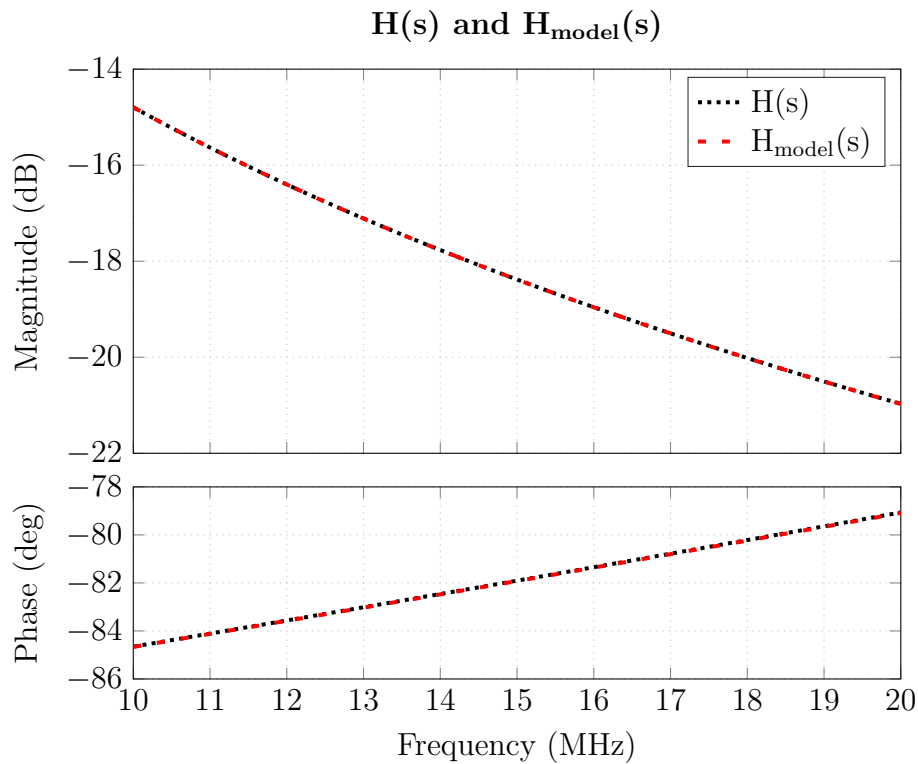


Figure 7.10: Bode plots of analytically determined $H(s)$ (eq. 6.30) and implicit transfer function $H_{\text{model}}(s)$ acquired from the software model

The model is thereby proven to be in accordance with the analytical derivation of $H(s)$, which allows current I_{PICC} to be observable from the model. Fig. 7.11 shows the output signal U_{SC} of the second transient simulation and the current I_{PICC} , related to one another via $H_{\text{model}}(s)$.

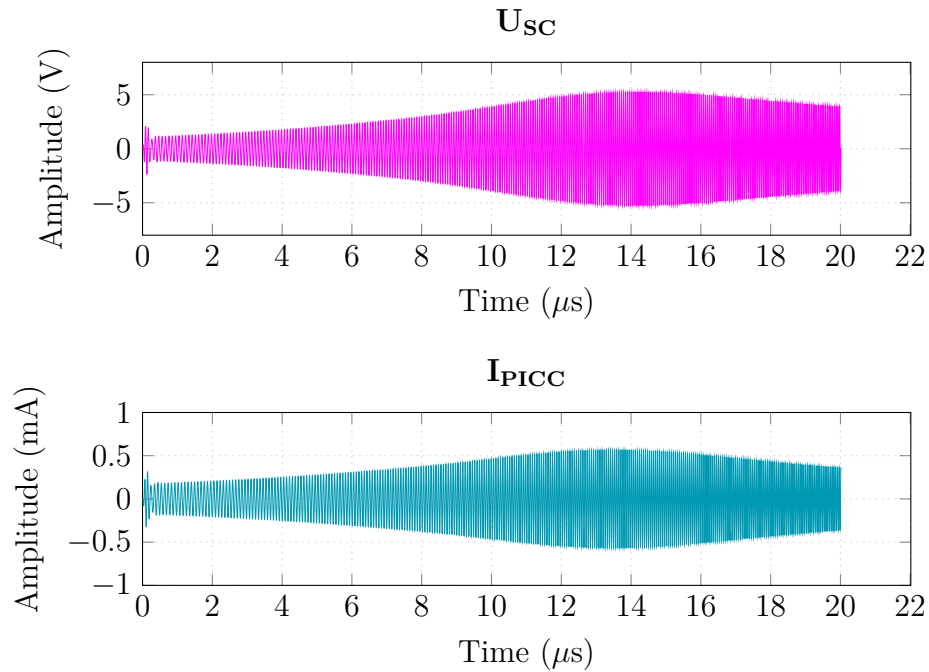


Figure 7.11: I_{PICC} is observable in the model, obtained from U_{SC} via $H_{model}(s)$

Obtaining P_{REL}

The next step is to obtain the relative active power P_{REL} as described in section 6.2. The phase angle φ obtained based on considerations in section 6.5 is depicted in fig. 7.12.

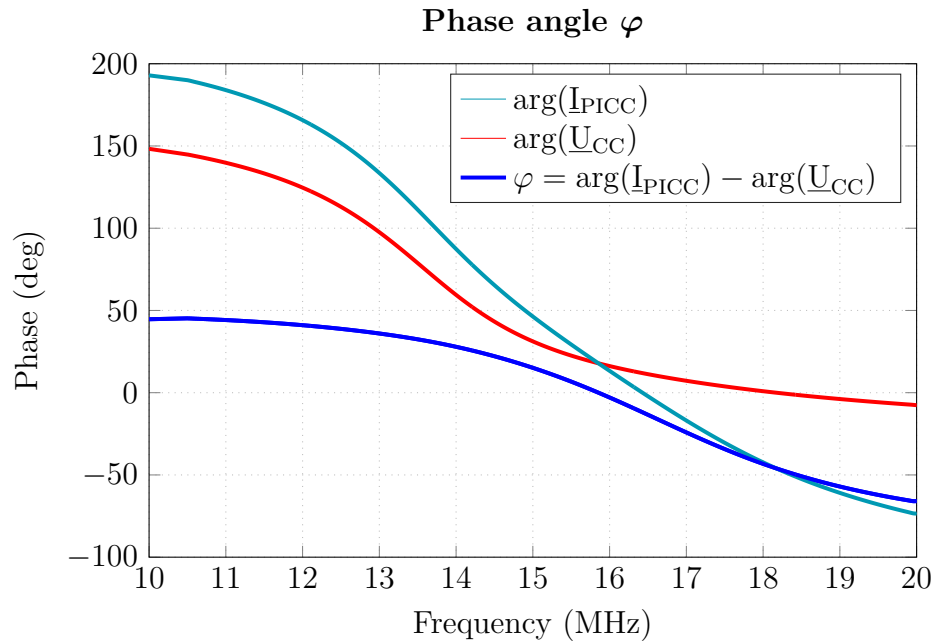


Figure 7.12: Phase angle φ is the phase difference between \underline{I}_{PICC} and \underline{U}_{CC}

Fig. 7.13 illustrates P_{REL} , determined as product of the \underline{I}_{PICC} envelope (fig. 7.11) and cosine of φ (fig. 7.12).

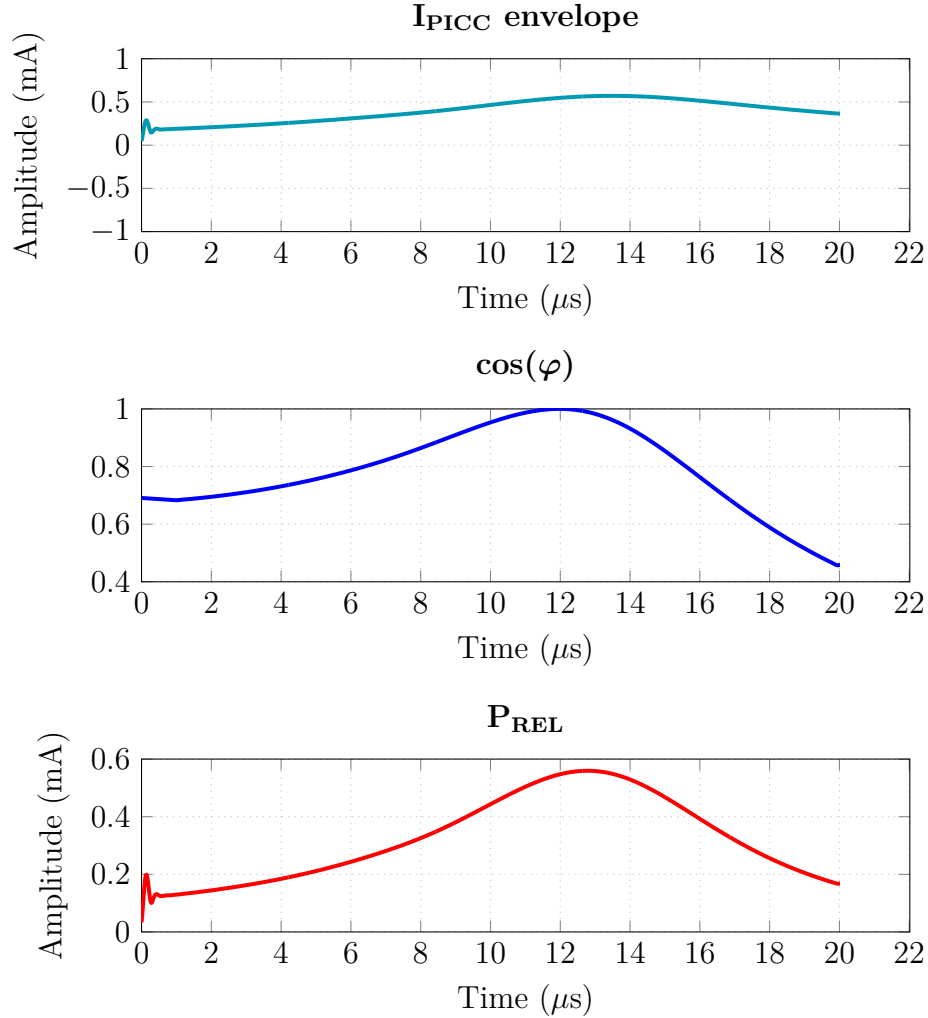


Figure 7.13: P_{REL} is determined as product of I_{PICC} envelope and $\cos(\varphi)$

Determining f_{RES}

According to section 6.6, maximum of this P_{REL} is mapped to a corresponding index in the $U_{CC,shaped}$ signal, which is subsequently cut and windowed using Hann window function, resulting in $U_{CC,shaped,cut>windowed$ signal that is ready for FFT to be performed. Resonance frequency determined this way for the simulation is shown in fig. 7.14. The spectral peak of $U_{CC,shaped,cut>windowed$ essentially represents the resonance frequency for the extended method and should in theory be equal to the resonance frequency at $P_{PICC,max}$ from table 7.1. These values are compared in table 7.3.

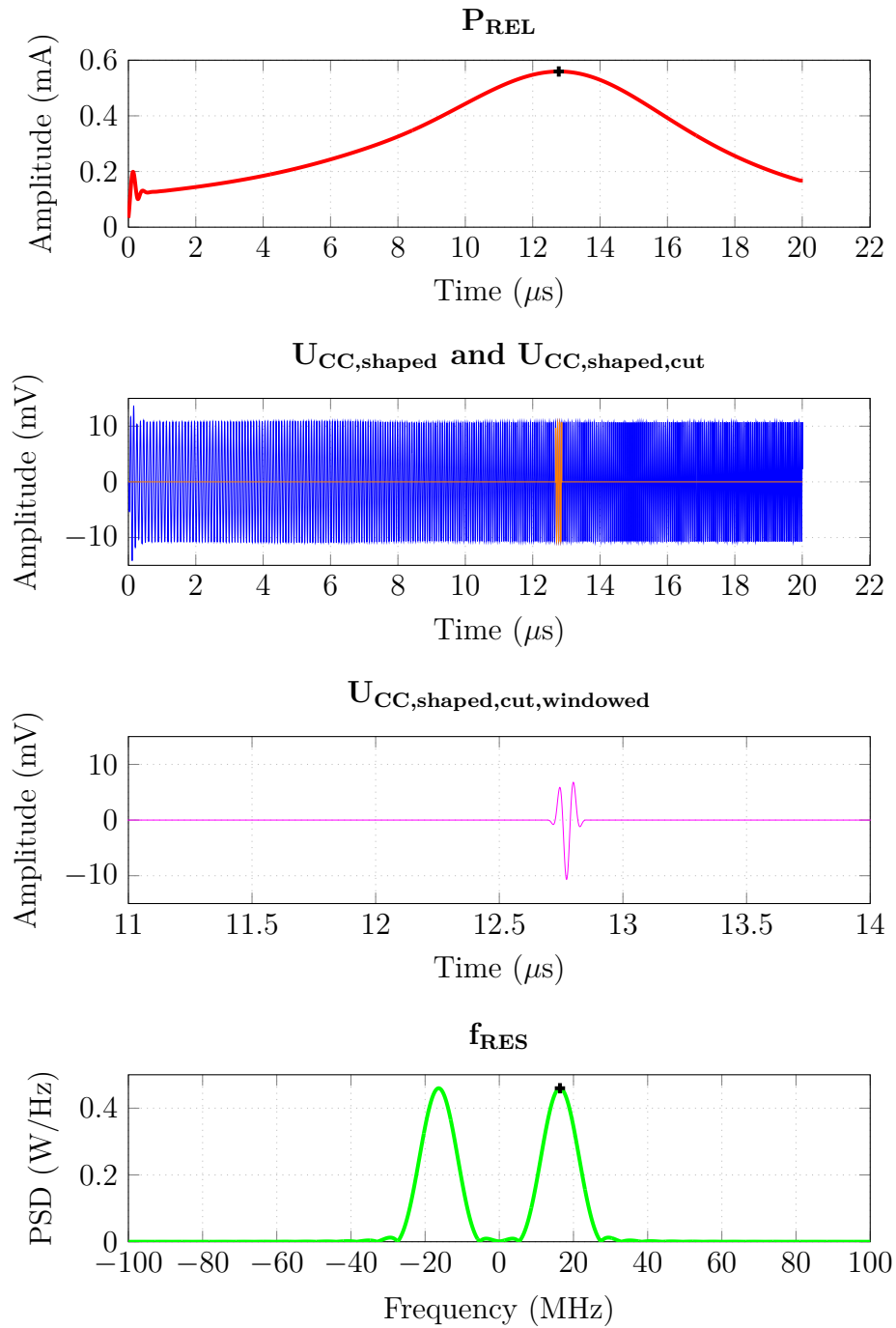


Figure 7.14: Determining the resonance frequency from P_{REL} for the simulation

It can be seen that the two values differ only by 1.187 kHz, which can be attributed to accuracy limitations of the simulation and is almost negligible. This comparison of simulation results represents the first proof of concept for the extended method. However, more information is required for total confirmation, which shall be discussed in the next section.

7.2.2 Feasibility Study

Values of C and R_{IC} from the model are varied in order to broaden the scope of the feasibility study and determine f_{RES} over a wider range of IC input characteristics, thus emulating the behavior of real ICs over input power (fig. 5.8). In this study, 15 different values of f_{RES} from the two simulations are compared: AC simulation of just the PICC and the resonance frequency at $P_{PICC,max}$ on the one hand, and resonance frequency obtained from the simulated procedure of the extended method on the other hand. The results are given in table 7.4, along with absolute and relative error.

Table 7.3: Comparison of simulated f_{RES} values

f_{RES}	(MHz)
AC simulation at $P_{PICC,max}$	16.349065
Extended method simulation	16.350252

Table 7.4: Different f_{RES} values for the two simulations: AC simulation in the PICC and simulated extended method

C (pF)	R_{IC} (Ω)	f_{RES}		Δ (kHz)	Rel. err. (%)
		$P_{\text{PICC,max}}$ (MHz)	Extended (MHz)		
30	400	16.8928	16.8065	-86	-0.51
36	500	16.4890	16.5041	15	0.09
37	600	16.6365	16.6091	-27	-0.16
32	700	18.0110	17.9941	-17	-0.09
30	800	18.7320	18.7220	-10	-0.05
36	800	17.1890	17.1831	-6	-0.03
45	800	15.4537	15.4849	31	0.20
35	900	17.5156	17.5198	4	0.02
40	1000	16.4823	16.5005	18	0.11
38	1100	16.9416	16.9604	19	0.11
30	1200	19.0507	19.0533	3	0.01
42	1400	16.2023	16.2452	43	0.26
33	1500	18.2643	18.3146	50	0.28
40	1800	16.6431	16.7015	58	0.35
35	2000	17.7975	17.8656	68	0.38

It can be seen that the absolute error mainly stays in the area between 10 kHz and 70 kHz, which is a better confidence interval than it is the case with the mere reproducibility of a single measurement performed with the VNA method. Also visible in the results is the behavior of the model with decreasing values of R_{IC} . This is expected, because for such low values of R_{IC} the condition 5.7 does not hold anymore, and the model of the extended method reaches its limits, resulting in the f_{RES} values of the two simulations to diverge from one another. Such behavior of f_{RES} is also congruent with the one from fig. 5.2. Nevertheless, the feasibility study of the extended method can be considered a success, with its results encouraging the transition from simulations to real measurements.

Chapter 8

Implementation of the Extended Method

With a confirmed proof of concept, the next step is to implement the extended method as actual measurements performed on a standardized ISO setup. This chapter describes how these measurements were carried out in reality, focusing on overcoming the obstacles formed when noise, IC nonlinearities, and measurement uncertainties are introduced into the system. The extended method was initially applied on samples consisting only of passive components that have no dependence on the input power. These results also confirmed the feasibility of the method, so that it could be proceeded with measurements of PICCs that contain commercial ICs. In addition, comparisons with the VNA method were performed and the results are discussed in this chapter, showing the strengths of the extended method. However, the method features certain limitations as well, which shall be listed in this chapter, along with some possibilities for improvement. All in all, the results show that the extended method has a significant advantage over the VNA method.

8.1 Differences from the Model

Both the concept of the extended method (chapter 6) and its simulations (chapter 7) are based on the ISO test PCD assembly model presented in this thesis (fig. 4.15). However, a model cannot represent a system in reality without making certain simplifications and approximations. Some important distinctions between model and real system that may have an influence on measurement results are listed here.

Coupling between PICC and lower sense coil: It has already been mentioned that this coupling ($k_{\text{PICC}\leftrightarrow\text{SC,down}}$) was not included in the model in order to simplify the analytically determined transfer function between U_{SC} and I_{PICC} . In reality, however, there is a small voltage induced by the PICC in the lower sense coil that has a slight, almost negligible impact on the transfer function. For the sake of completeness, $k_{\text{PICC}\leftrightarrow\text{SC,down}}$ is listed in table 7.2, where it can be seen that it is significantly lower than $k_{\text{PICC}\leftrightarrow\text{SC,up}}$ and thus neglected.

$U_{\text{CC}} \rightarrow U_{\text{CC,ind}}$ transfer function: In the concept for the extended method, the voltage that is measured with an oscilloscope probe at the calibration coil (U_{CC}) is assumed to be in-phase with voltage that is induced in the PICC (U_{PICC}). Namely, the probe is modeled in the case for U_{SC} , but for the calibration coil it is assumed that the probe has high enough impedance so that its own frequency response is negligible. If this is the case, the voltage measured with the probe is indeed in-phase with the voltage that is actually induced in the coil by the PCD ($U_{\text{CC,ind}}$). Hence, neglecting the influence of the probe at the calibration coil may have a small influence on determining the phase angle φ .

Model parameters: In addition to $k_{\text{PICC}\leftrightarrow\text{SC,down}}$ and oscilloscope probe at the calibration coil, there are other parameters that were omitted from the model. For example, none of the parasitic capacitances of antennas are considered, nor are the capacitances of BNC and other connectors. Furthermore, perfect symmetry between upper and lower sense coil in an ISO test PCD assembly can never be achieved, leading to a certain error differential voltage $U_{\text{SC,error}}$ even when no PICC is present. Lastly, the accuracy of the values in table 7.2 is limited by the accuracy of the measurement methods used to obtain these values. This especially applies to the sensitive measurement of coupling coefficients.

Chirp duration: The model uses a rather short input chirp signal ($20\ \mu\text{s}$) because it significantly reduces the time of a transient simulation. However, commercial ICs have their start-up, execution, and transmission stages in the ms range, and the input signal that changes frequency over time should be long enough so that IC can receive energy required to start-up and not perform a reset. Even though the input chirp is constant in amplitude, these ICs experience the highest magnetic field strength at resonance, meaning that a carrier frequency far from resonance would be perceived as a lower magnetic field by the IC. The IC internal voltage regulator would need to adapt to this new frequency. Because the voltage step of the regulator is usually limited, the chirp should be longer to allow smoother transitions

between higher and lower magnetic fields acting on the PICC. Input chirp signal (U_{AWG}) is therefore chosen to be 1 ms.

Tool and device limitations: The signal processing tool (MATLAB in this case) has its limitations when dealing with a large number of data points. For much longer signals (1 ms instead of $20 \mu\text{s}$) some signal processing steps such as filtering and interpolating may not be possible with arbitrarily high accuracy. Granularity of the FFT is another one of those factors. Furthermore, the devices used for measurements have their own limitations: sample frequency of the AWG and oscilloscope, vertical resolution of the oscilloscope, temperature coefficient of the RF amplifier, etc.

8.2 Performed Measurements

Having completed all preparations in terms of concept, simulation, and device instrumentation, the first measurements with the extended method were ready to begin. All measurements were performed on the ISO measurement setup (fig. 4.18) using the ISO test PCD assembly with known circuit parameters (table 7.2).



Figure 8.1: A reference PICC and a commercial IC, with a variable capacitor added in the middle of the PICC (courtesy of Infineon Technologies Austria AG)

When it comes to PICCs, instead of using laminated chip cards it is sometimes necessary to separate the two main PICC components (antenna and IC) from one another and use the same IC on a different antenna design, or vice versa. For that reason, IC manufacturers utilize so-called reference PICCs (fig. 8.2) that have a removable slot for an IC enclosed in a CDIP package. Reference

8.2 Performed Measurements

PICCs also allow the possibility of easily tuning the resonance frequency via the added tune capacitance (fig. 4.4) without changing any of the antenna or IC circuit parameters. The same reference PICC was used for all resonance frequency measurements, with its values for L_{PICC} and $R_{L_{\text{PICC}}}$ measured and listed in table 7.2. Thus, only the ICs (and passive components representing ICs) were interchanged between measurements. The term *sample* from the upcoming discussions hence in this context refers to the IC.

The same settings that were applied for all measurements are listed in table 8.1. For a typical 13.56 MHz carrier signal the AWG sampling rate is chosen to be 94.92 MHz, which is a sevenfold multiple of 13.56 MHz, in order to ensure an integer number of points per cycle. With a chirp signal, on the other hand, the number of points per cycle changes with increasing frequency. Nevertheless, the AWG sampling rate is chosen to be an integer multiple of the initial frequency in the chirp. In this case it is 10 MHz, so AWG is set at a ninefold multiple, i.e. 90 MS/s.

Table 8.1: Settings used for the extended method

Setting	Value	Unit
Frequency range	10...20	MHz
AWG sampling rate	90	MS/s
Input chirp duration	1	ms

Time is always an important factor in measurement techniques, especially if a certain level of automation is involved, where shorter lasting measurements highly increase productivity when performed on multiple samples. In case of the extended method, information about the duration of a single measurement is given in table 8.2. It can be seen that the entire measurement is complete in under 25 s time, with its longest lasting portion being the shaping of U_{CC} . This is because shaping performs the process of downloading an arbitrary waveform sequence to the AWG twice, first with the constant input signal U_{AWG} , followed after the described processing steps (chapter 6) by the shaped input $U_{\text{AWG,new}}$. Obviously, duration of the measurement depends on the duration of the chirp, and is therefore not to be taken as a fixed value. Assuming one wants to measure resonance frequency at a fixed value of H , extended method is considerably faster than the VNA method.

Table 8.2: Duration of a measurement performed with the extended method

Stage	Duration (s)
Chirp generation	1...3
Shaping of U_{CC}	13..16
Computing f_{RES}	3...4

8.2.1 Passive Components

Instead of immediately using actual ICs as samples, the extended method was tested on sample circuits consisting only of a capacitance and resistance connected in parallel. This can be considered as reality counterpart to the performed simulations, which also used only a capacitance and a resistance (C and R_{IC}) to model the IC. Inserted into the reference PICC, such parallel connection of passive components forms a linear resonant circuit that has no dependence on the input power and thus has constant resonance frequency, regardless of the induced voltage. Ten samples with variable capacitors and resistors were created and measured with both the VNA method and the extended method (fig. 8.2).

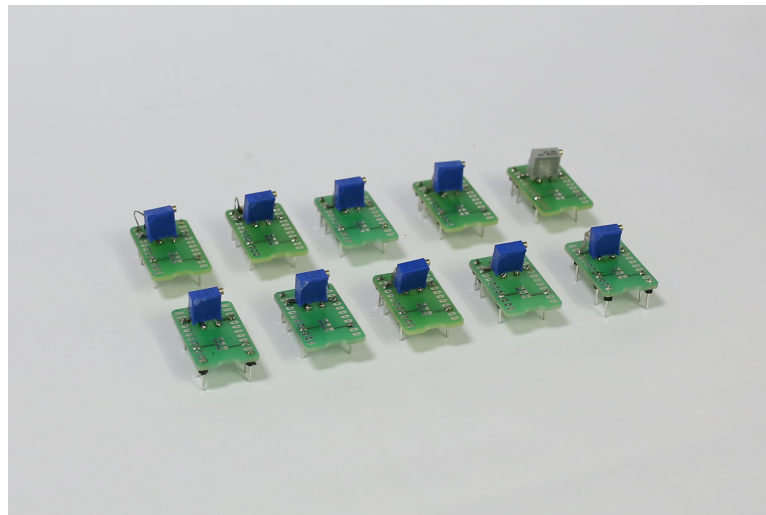


Figure 8.2: Passive components consisting of C and R_{IC} connected in parallel that were initially measured in order to test the extended method

The values of C and R_{IC} were varied so that ten different resonance frequencies between 10 MHz and 16 MHz could be achieved. Using passive components allowed better insight and analysis during development of process steps in the

8.2 Performed Measurements

implementation of the extended method. The arbitrary choice of input power allowed the focus to be on the signal processing procedure itself, instead of measuring commercial ICs and observing their behavior during measurement. All ten samples were measured with both methods and the results, along with absolute and relative error, are visualized in fig. 8.3 and listed in table 8.3.

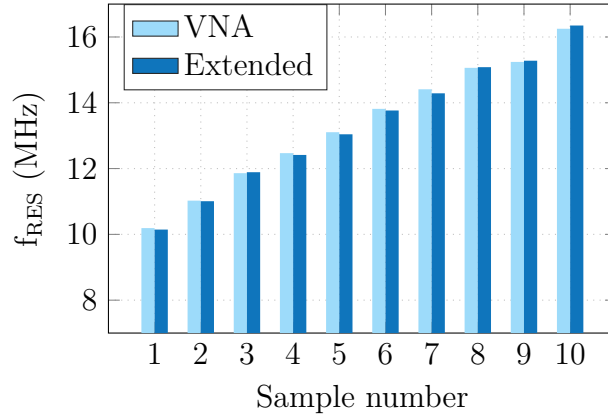


Figure 8.3: Measured f_{RES} : passive components

The extended method yielded very satisfactory results, differing from the VNA method results by maximum of 120 kHz, which is still a relative error of less than 1%. There was no noticed pattern among the errors, which can therefore be attributed to the factors that are already described in this chapter.

Table 8.3: Measured f_{RES} values: passive components

Sample	f_{RES}		Δ (kHz)	Rel. err. (%)
	VNA (MHz)	Extended (MHz)		
1	10.190	10.146	-44	-0.436
2	11.025	11.008	-17	-0.157
3	11.860	11.889	29	0.246
4	12.469	12.414	-55	-0.438
5	13.105	13.042	-63	-0.481
6	13.815	13.765	-50	-0.359
7	14.410	14.288	-122	-0.850
8	15.062	15.082	20	0.135
9	15.242	15.279	37	0.240
10	16.250	16.349	99	0.606

Feasibility of the extended method was verified based on results of the passive components measurements, so the next step was to perform measurements on actual ICs that are used in proximity coupling systems.

8.2.2 Commercial ICs

It has already been explained that the complexity of commercial IC prevents linearity to be assumed as is the case with simple C and R_{IC} parallel circuits. Furthermore, the input characteristics of ICs depend on the power that is fed into the system, i.e. on the voltage induced in the PICC (fig. 5.8). As mentioned in chapter 5, the resonance frequency is usually defined at the start-up point, a power level where the IC is supplied with enough power to turn on.

Unloaded State

However, there is a power level well below the start-up point, at which the IC is not active and can be considered as merely a collection of complex circuits, with approximately constant input characteristics with respect to input power. This is referred to as the so-called *unloaded* state of an IC, which is associated with very low magnetic field strengths. This also means that the IC has different resonance frequency for the unloaded state, because input characteristics are vastly different then they are at the start-up point. Measuring this unloaded resonance frequency might be required in some cases. The values of C are usually lower in the unloaded state, and those of R_{IC} are much higher, resulting in both resonance frequency and quality factor to be higher than at the start-up point. Therefore, f_{RES} of ICs in the unloaded state are much easier to measure with the VNA method, because at such low power levels the input characteristics are not as sensitive to input power. A particular power level at which f_{RES} should be measured must still be defined. For the VNA method, the power of the frequency sweep should be set at -30 dBm, and the PICC should be at exactly 2 cm distance from the measuring coil of the VNA.

Instead of immediately measuring f_{RES} at start-up, it was interesting to see if the extended method would be able to measure the unloaded f_{RES} , as the unloaded state can be considered somewhere in between passive components and ICs above the start-up point that display nonlinear behavior and variable input characteristics. For that reason, 18 different IC samples (such as the one inserted into the PICC slot in fig. 8.1) were measured in the unloaded state with both measurement methods. Of course, there is no definition of unloaded state power level for the extended method, so it had to be defined arbitrarily. The chosen level of U_{CC} (after shaping) was 40 mV, which corresponds to $H_{RMS}=0.044$ A/m, according to eq. 4.3.3. Results of unloaded state measurements are depicted in

fig. 8.4 and listed in table 8.4.

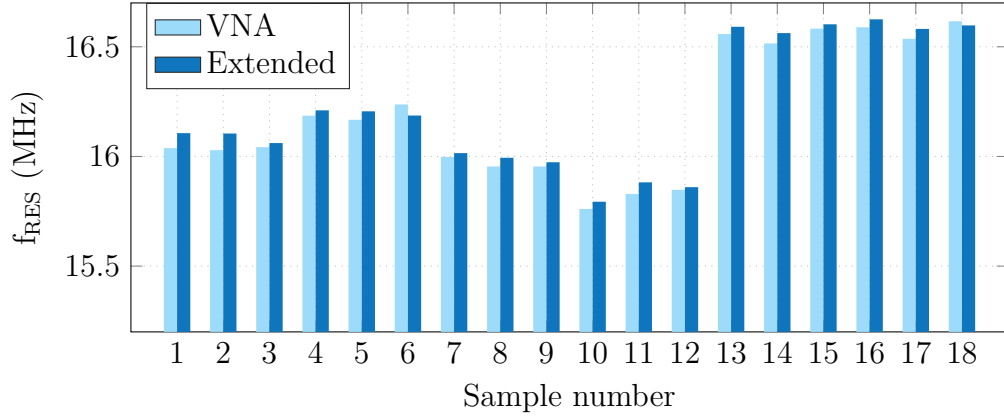


Figure 8.4: Measured f_{RES} : samples in unloaded state

Table 8.4: Measured f_{RES} values: samples in unloaded state

Sample	f_{RES}		Δ (kHz)	Rel. err. (%)
	VNA (MHz)	Extended (MHz)		
1	16.038	16.106	68	0.427
2	16.029	16.105	76	0.473
3	16.042	16.061	19	0.116
4	16.186	16.210	24	0.150
5	16.167	16.206	39	0.239
6	16.237	16.186	-51	-0.312
7	15.998	16.015	17	0.109
8	15.954	15.994	40	0.250
9	15.954	15.974	19	0.122
10	15.760	15.794	33	0.210
11	15.829	15.882	53	0.335
12	15.848	15.860	12	0.076
13	16.558	16.591	33	0.199
14	16.515	16.562	47	0.286
15	16.583	16.603	20	0.119
16	16.589	16.625	36	0.218
17	16.537	16.582	45	0.272
18	16.616	16.598	-19	-0.114

Unloaded measurements gave even better results than passive components did, the highest absolute error being 76 kHz and relative error not exceeding 0.5%. The relative error is of course partly lower due to somewhat higher values of resonance frequency in the unloaded (around 16 MHz). The notion that 16 out of 18 samples showed a positive offset may indicate that the arbitrary choice of $U_{CC}=40$ mV may not had been the best one. There was however not much possibility to choose lower than 40 mV, because noise and vertical resolution of the oscilloscope were limiting factors, for example, at 20 mV, preventing the extended method to produce any results. Nevertheless, the error at 40 mV was still low enough so that no further measurements were required for the unloaded state.

Start-up and Fixed Values of H

Determining the start-up point on the VNA has already been said to be somewhat subjective because it relies on qualitative interpretations of the $\Re\{Z_{VNA}\}$ curve (chapter 5). As for the extended method, it finds itself in the following predicament: *Even though the extended method is able to set a constant U_{CC} at any desired value (and therefore a constant H) over the entire range of frequencies contained in the chirp, the level of H that corresponds to the start-up point still needs to be known before it can be set.* This is probably the largest disadvantage of the extended method. On the other hand, definition of f_{RES} at the start-up point was established through a convention, more due to commercial and marketing reasons than it is due to physical ones. The ICs have different f_{RES} values for different values of H , where f_{RES} of the start-up point is simply *one of such values*. For example, if through another convention it happened to be decided that f_{RES} should always be measured at 1 A/m or 1.5 A/m (both values featuring prominently among standards), the extended method would instantly render the VNA method obsolete.

However, in order to achieve a tangible comparison of the two methods, there has to be a way to measure ICs at the start-up point using the extended method. An ultimate solution would be to automatically detect the start-up point and set the corresponding level of H for each measured sample. As such powerful solution was not found over the course of this thesis, one had to revert to more inelegant approaches in order to compare the two methods. This was done by observing the PICC with an oscilloscope while the VNA method was performed, and subsequently setting the extended method's power level based on the behavior of the observed voltage from the VNA method. That way, the methods were able to be compared, although it is not how f_{RES} is intended to be measured with the extended method.

Beside comparing the two methods at start-up point, two further levels of H were measured with the extended method in order to investigate how much f_{RES}

8.2 Performed Measurements

changes with the field strength, and possibly hint at a change in the currently established convention for defining f_{RES} of commercial ICs. To summarize, the same 18 samples from the unloaded state measurements were measured at three different levels of magnetic field strength H , which can in turn be converted to three different levels of U_{CC} (eq. 4.3.3).

Start-up point: H that corresponds to the start-up point observed on the VNA, has a variable value depending on the sample (lower than 1 A/m)

H=1 A/m: Corresponds to $U_{\text{CC}} \approx 0.9 \text{ V}$

H=1.5 A/m: Corresponds to $U_{\text{CC}} \approx 1.35 \text{ V}$

The results are visualized in fig. 8.5 and listed in table 8.5. The absolute and relative error were only calculated for the start-up point, as it made no particular sense to compare the VNA method with the higher levels of H when it was already expected of f_{RES} to change considerably.

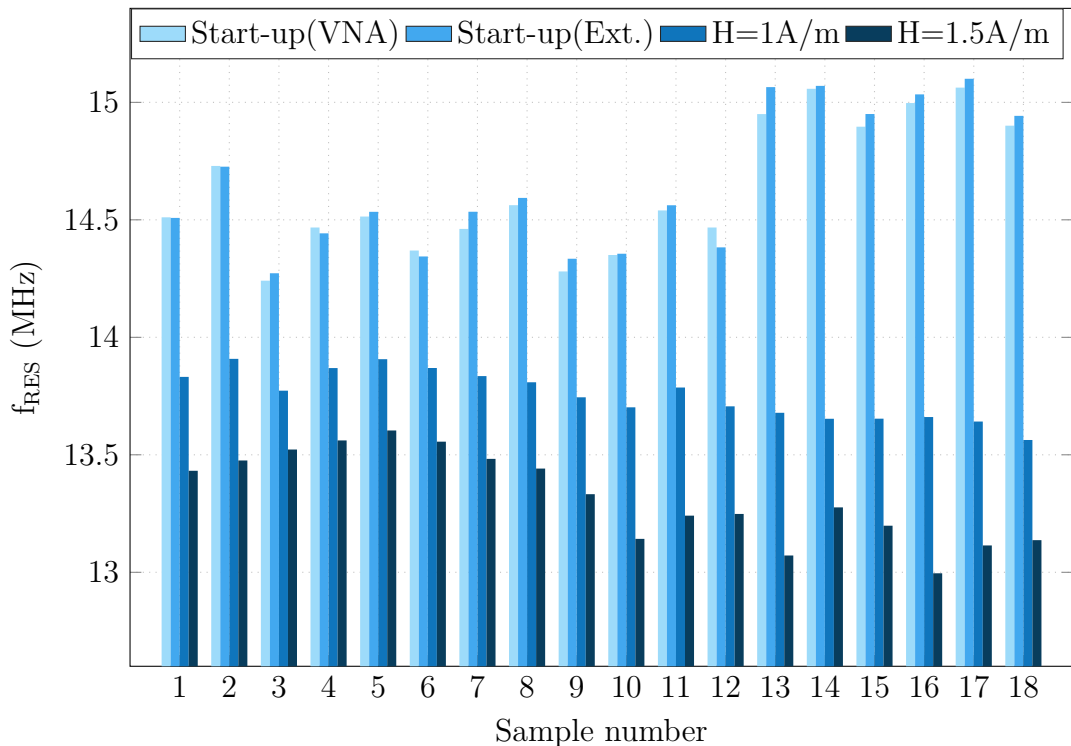


Figure 8.5: Measured f_{RES} : samples at start-up, $H=1 \text{ A/m}$, and $H=1.5 \text{ A/m}$

The manually searched values of H at start-up seemed to be rather properly determined, because comparing f_{RES} values between two methods showed that the

8.2 Performed Measurements

highest absolute error amounted to 115 kHz and that relative error did not exceed 0.8%. This leads to the conclusion that the extended method could definitely replace the VNA in terms of precision, provided of course that the solution for finding the start-up point would be found.

On the other hand, the results of $H=1$ A/m and $H=1.5$ A/m measurements cannot be compared to the VNA method, but rather serve as an example of how much f_{RES} can change when measured at higher field strengths. The fact that it decreases with increasing field is congruent with fig. 5.8: C increases with input power, so that for higher values of C the resonance frequency decreases, because C and f_{RES} are inversely proportional to one another (Thomson eq.).

Table 8.5: Measured f_{RES} values: samples at start-up, $H=1$ A/m, and $H=1.5$ A/m

Sample	f_{RES}		Δ (kHz)	Rel. err. (%)	f_{RES}	
	Start-up				$H=1$ A/m	$H=1.5$ A/m
	VNA (MHz)	Extended (MHz)			Extended (MHz)	Extended (MHz)
1	14.511	14.508	-2	-0.017	13.832	13.432
2	14.729	14.726	-3	-0.021	13.908	13.476
3	14.241	14.273	32	0.222	13.773	13.523
4	14.467	14.443	-25	-0.172	13.869	13.561
5	14.514	14.534	20	0.138	13.907	13.604
6	14.369	14.344	-25	-0.175	13.869	13.556
7	14.461	14.534	73	0.505	13.835	13.483
8	14.562	14.593	31	0.212	13.809	13.441
9	14.280	14.334	54	0.378	13.745	13.332
10	14.350	14.356	5	0.038	13.702	13.142
11	14.540	14.562	22	0.152	13.786	13.241
12	14.467	14.383	-85	-0.584	13.706	13.248
13	14.950	15.065	115	0.768	13.679	13.072
14	15.058	15.070	12	0.082	13.653	13.276
15	14.896	14.950	54	0.362	13.654	13.198
16	14.997	15.034	37	0.246	13.661	12.996
17	15.063	15.100	38	0.250	13.642	13.114
18	14.901	14.943	42	0.281	13.563	13.137

As far as commercial ICs are concerned, the extended method can be also considered as successful, except for the issue of finding the H of the start-up point easily. It remains to be seen how this issue shall be resolved in the future,

either with a brand new convention of defining f_{RES} (for example at a fixed H), or with an efficient way to determine and set the magnetic field strength exactly at the start-up point.

8.3 Measurement Reproducibility

When developing a new measurement method, it is always important to determine the level of reproducibility of a single measurement. This means answering the question of how close results are to one another when the same measurement conditions are repeated multiple times on the same sample. Such results would describe the level of *precision* of the extended method. For that reason, one IC sample was measured using the extended method at the three levels of H : start-up, $H=1$ A/m, and $H=1.5$ A/m, and each measurement was repeated in 1000 runs. A statistical analysis was subsequently performed in order to determine the reproducibility of the extended method.

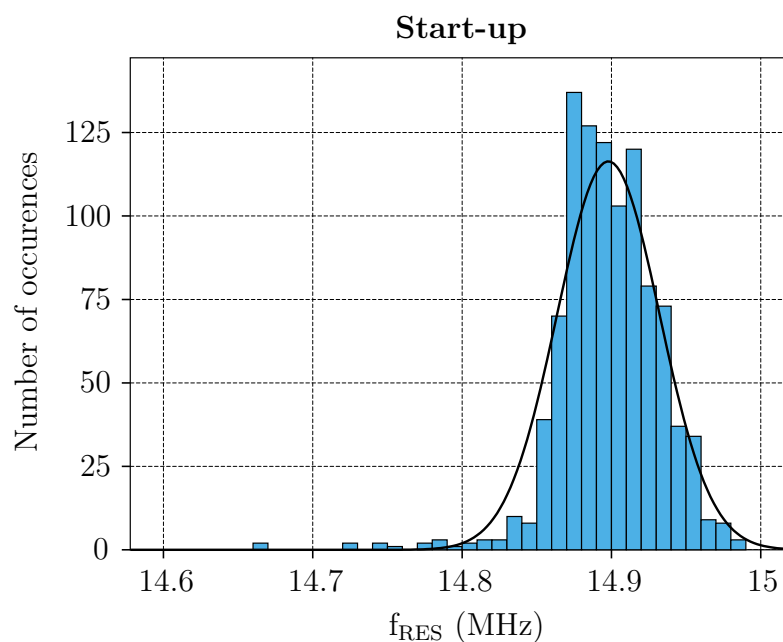


Figure 8.6: Histogram of f_{RES} after 1000 measurement runs: start-up

Histogram of f_{RES} at the start-up point is depicted in fig. 8.6 and the corresponding descriptive statistics are presented in table 8.6. It can be seen that standard deviation amounts to approximately 34 kHz, which is more than acceptable. For comparison, human error when qualitatively determining f_{RES} at the start-up point on the VNA can often go over 500 kHz.

8.3 Measurement Reproducibility

Table 8.6: Descriptive statistics of f_{RES} after 1000 measurement runs: start-up

N	Min (MHz)	Max (MHz)	Mean (MHz)	Std. Error (kHz)	Std. Dev. (kHz)	Variance (kHz)
1000	14.664	14.983	14.898	1.079	34.135	1.165

For the case of $H=1$ A/m, results of the statistical analysis are shown in fig. 8.7 and table 8.7, respectively.

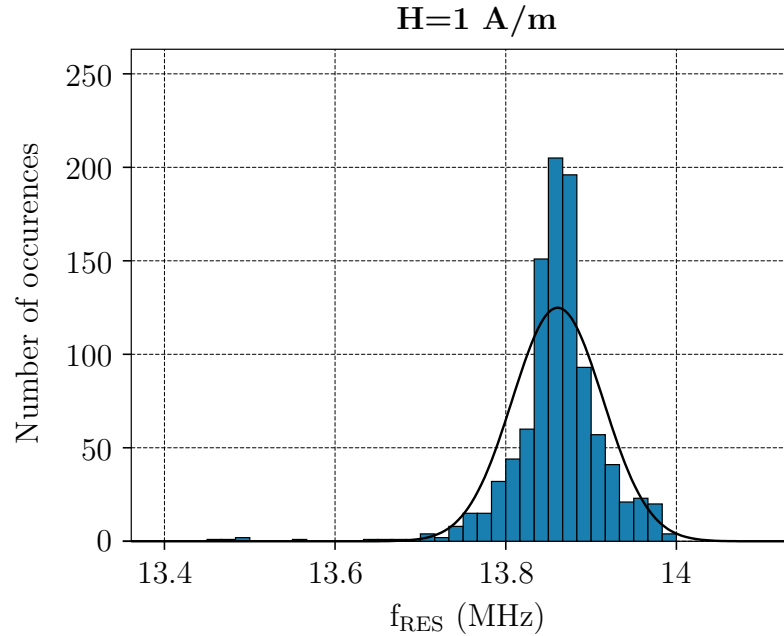


Figure 8.7: Histogram of f_{RES} after 1000 measurement runs: $H=1$ A/m

Here, the standard deviation is somewhat higher (around 53 kHz), yet still low enough for the extended method to be considered as satisfactory in terms of precision.

Table 8.7: Descriptive statistics of f_{RES} after 1000 measurement runs: $H=1$ A/m

N	Min (MHz)	Max (MHz)	Mean (MHz)	Std. Error (kHz)	Std. Dev. (kHz)	Variance (kHz)
1000	13.458	13.994	13.861	1.683	53.216	2.832

8.3 Measurement Reproducibility

At $H=1.5$ A/m, the standard deviation was the highest, at approximately 94 kHz. One could assume that this trend of decreasing precision continues with higher field strengths. Without confirmation, however, no final statement should be given about reproducibility of the measurement with respect to H .

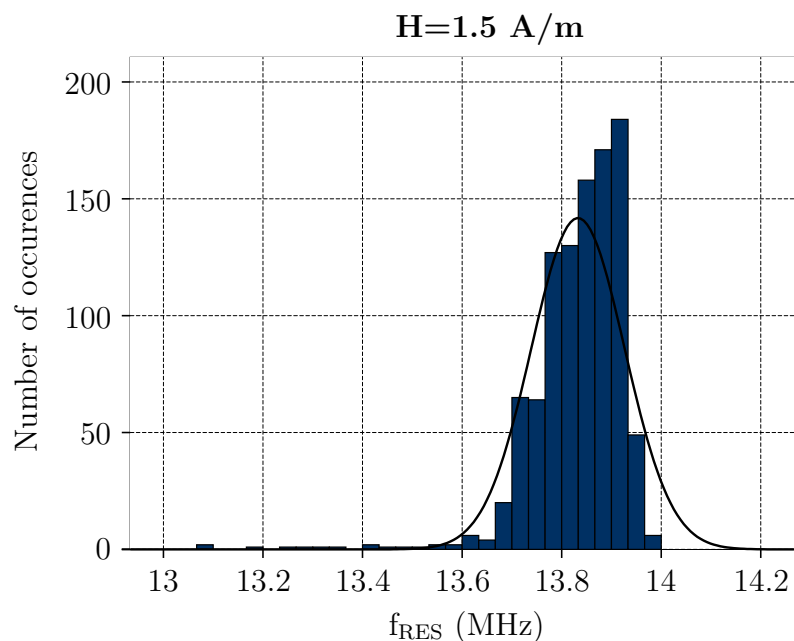


Figure 8.8: Histogram of f_{RES} after 1000 measurement runs: $H=1.5$ A/m

Judging by results of the statistical analysis, the determined values for standard deviation and other important parameters indicate that the extended method offers a good level of measurement reproducibility. Seeing how that typical measurements performed using the VNA method are rounded at the first decimal (i.e. in hundreds of kHz), extended method is shown to be advantageous in terms of precision.

Table 8.8: Descriptive statistics of f_{RES} after 1000 measurement runs:
 $H=1.5$ A/m

N	Min (MHz)	Max (MHz)	Mean (MHz)	Std. Error (kHz)	Std. Dev. (kHz)	Variance (kHz)
1000	13.071	13.976	13.838	2.966	93.791	8.797

8.4 Measurement Accuracy

The statement about precision of the extended method expresses only the relation between multiple results under the same circumstances, and does not give any insight about how results differ from the *true* value of the measured quantity, f_{RES} in this case. Closeness of a measurement to the true value is defined by the measurement *accuracy*, which shall be discussed in this section.

In order to ascertain the accuracy of a measurement, a known reference value would have to exist. In this case, unfortunately, there is no such value for resonance frequency, because the only way to determine f_{RES} is by measurement. Up to this point, it could only be done using the VNA method, which is already known to be inaccurate (because of the different definition of f_{RES}) and sometimes even imprecise (because of qualitative interpretations of $\Re\{Z_{\text{VNA}}\}$ curves). One also cannot rely on theoretical definitions of f_{RES} (chapter 5) because they involve a high degree of abstraction, especially when commercial ICs are concerned.

The only appropriate solution would be to construct a reference sample with an exactly predetermined resonance frequency and apply the extended method in order to determine its accuracy. However, the extended method also incorporates a known systematic error by defining f_{RES} at $P_{\text{PICC,max}}$ instead of $P_{\text{IC,max}}$. The predetermined f_{RES} of the reference sample would have to correspond to the same definition of f_{RES} that extended method uses ($P_{\text{PICC,max}}$) so that there would be no systematic errors involved and only accuracy of the method's implementation could be compared. As such reference sample does not exist and is probably not possible to create, there is unfortunately no statement that could be given about the accuracy of the extended method.

Chapter 9

Conclusion

This chapter gives some concluding thoughts about the extended measurement method, the development steps that preceded its implementation, as well as some future prospects. The advantages and disadvantages of the method are summarized here, along with their impact on the currently used VNA method. It can be concluded with optimism that measuring resonance frequency of chip cards lies on the edge of a new frontier.

9.1 Summary

This thesis opened with an introduction into the world of RFID systems (chapter 2), describing its wide spectrum of systems and components. Narrowing the focus onto proximity coupling systems, chapter 3 elaborated on the physical principles behind the operation of proximity coupling systems, introducing important concepts of inductive coupling and resonance. From there, chapter 4 showed how these concepts are utilized in actual RFID systems, focusing on proximity coupling contactless chip cards. System components were presented using equivalent circuit models, including the important transformed impedance Z_T . Data communication principles among proximity coupling systems were briefly mentioned, with focus on load modulation and its influence on Z_T . Chapter 4 also introduced the ISO test PCD assembly and its measurement setup, both playing essential roles in development and verification of proximity coupling systems.

The second part of the thesis focused on the resonance frequency and its measurement methods, starting with different definitions of resonance frequency and the currently established VNA measurement method (chapter 5). In order to mitigate the VNA method's disadvantages and simultaneously make f_{RES} measurements possible on standardized setups, an extended measurement method

was proposed in chapter 6. It included a new definition of resonance frequency and a series of signal processing steps that was required for determining this new f_{RES} . Information about the maximum of an active power quantity (P_{REL}) in the PICC allowed a conclusion to be drawn about resonance frequency, as long as there was constant voltage induced in the PICC over multiple frequencies (done by shaping of U_{CC}). The concept for the extended method was then applied on a model of the system using simulations that managed to prove the feasibility of the method (chapter 7). Finally, the extended method was implemented as actual measurement on real samples and compared with the VNA method (chapter 8), yielding very promising results. However, some difficulties also accompanied the measurements, where the issue of finding the start-up point power level of commercial ICs was singled out as the greatest challenge of the extended method.

9.2 Advantages over VNA Method

Compared to the VNA method, the extended method can be considered as superior due to reasons listed here.

Better definition for f_{RES} : After analyzing the different definitions for f_{RES} between the two methods, especially in cases when the definitions diverge from one another (condition 5.7 barely fulfilled), the f_{RES} definition of the extended method ($P_{\text{PICC,max}}$) is shown to be more accurate to the chosen ideal definition ($P_{\text{IC,max}}$) than it is the case with the VNA method definition ($\Re\{Z_{\text{T}}\}_{\text{max}}$)

Objective: For a chosen fixed level of H , the extended method removes the possibility of human error from the measurement, because it comes down to a simple push of a button, and does not involve any qualitative interpretations like the ones required for the VNA method. Therefore, the extended method is only limited by reproducibility and accuracy that exclude the human factor.

Correlation between f_{RES} and H : Because the extended method measurement is integrated into the ISO test PCD assembly, there is a correlation between resonance frequency and magnetic field strength, allowing f_{RES} to be measured at an exactly set level of H

Part of ISO measurement setup: Again, due to the ISO test PCD assembly, the extended method can be used on standardized setups used for development and verification of proximity coupling systems. It can be easily included in larger test-benches that involve other measurements, without

any need for the sample to be removed from the setup for measuring f_{RES} , which is not the case with the VNA method.

Can be automated: Some standardized setups include special devices that enable multiple IC samples to be used with the same reference PICC, that can be switched automatically during measurements. This would also introduce a level of automation for f_{RES} measurements, without the need to measure all samples individually, as is the case with the VNA method.

9.3 Outlook

It seems that the only issue with the VNA method that the extended method did not manage to resolve is the one about automatically determining the power level of the start-up point. Unfortunately, this is probably the most important aspect of measuring resonance frequency for commercial IC manufacturers. Solving this issue goes beyond the scope of designing a new measurement method, it has more to do with the definition of resonance frequency itself. Now when a method exist that is basically part of the ISO measurement setup, it might be a time to reassess the currently established definition about the start-up point and maybe define f_{RES} at a fixed level of magnetic field strength, such as 1 A/m or 1.5 A/m.

Another approach would be to find a way to correlate the start-up point to the level of H without resorting to manual techniques like the ones described in chapter 8. It is possible that this could be achieved by performing a H sweep while measuring resonance frequency, and see how resonance frequency behaves when measured over a range of H instead of at one particular H level. This would mean that P_{REL} would be determined not only in one dimension (over frequency), but in two (over frequency and over H), resulting in a 3D version of the P_{REL} plot from fig. 7.14. Such H sweep was not performed in this thesis due to automation difficulties concerning calibration of AWG with respect to H. This is, however, definitely intended to be performed in the future. Hopefully, the resulting 3D curve of P_{REL} could provide the much needed information about the start-up point. In a way, this would also be a form of qualitative interpretation, but with one important difference: the extended method measurement would be automated, and f_{RES} would be extracted from the *results*, whereas with VNA it is done *during* measurement and therefore depends on the human factor.

Ultimately, it can be concluded that the extended method is has more than enough advantages to dethrone the currently established VNA method. As soon as the issue concerning the start-up point is resolved, the author sees no obstacle that would prevent the extended method from becoming the new standard for measuring resonance frequency of contactless chip cards.

References

- [1] K. Finkenzeller, *RFID Handbook: Fundamentals and Applications in Contactless Smart Cards and Identification*. Wiley, 2nd ed., 2003.
- [2] ISO/IEC, “ISO/IEC 14443, Proximity cards,” Tech. Rep. Part 1: Physical characteristics, Committee identification: ISO/IEC JTC1/SC17/WG8, 2010-09-01. Identification cards: Contactless integrated circuit(s) cards - Proximity cards.
- [3] S. Hackl, “Noise Transmission Modeling of Microcontroller Based Contactless Chip Card Systems.” Master’s thesis, 2006.
- [4] J. Bird, *Electrical Circuit Theory and Technology*. Newnes, 4th ed., 2010.
- [5] S. Rampetzreiter, “Very High Bit Rate Communication Channel Modeling on Inductively Coupled, Passive RFID Systems.” Master’s thesis, 2009.
- [6] J. Hölzl, “Extended Card Modulation - Test Methods.” Master’s thesis, 2011.
- [7] ISO/IEC, “ISO/IEC 10373, Identification cards - Test methods,” Tech. Rep. Part 6: Proximity cards, Committee identification: ISO/IEC JTC1/SC17/WG8, 2010-12-15. Identification cards: Contactless integrated circuit(s) cards - Proximity cards.
- [8] W. Lin, B. Geck, and H. Eul, “The Resonance Frequency Measurement Method of PICCs and the Environmental Influence,”
- [9] W. Lin, B. Geck, H. Eul, C. Lanschuetzer, and P. Raggam, “A Novel Method for Determining the Resonance Frequency of PICCs,” 2008.
- [10] F. Kilic, “Convergence of Standardized RFID Measurements.” Master’s thesis, 2011.
- [11] A. V. O. R. W. Schafer, *Discrete-Time Signal Processing*. Pearson Education, 2014.

REFERENCES

- [12] Austrian Institute of Technology, “Test PCD Assembly,” tech. rep., 2009.
- [13] M. Gebhart, J. Bruckbauer, and M. Gossar, “Chip Impedance Characterization for Contactless Proximity Personal Cards,” 2010.
- [14] ISO/IEC, “ISO/IEC 14443, Proximity cards,” Tech. Rep. Part 2: Radio frequency power and signal interface, Committee identification: ISO/IEC JTC1/SC17/WG8, 2010-09-01. Identification cards: Contactless integrated circuit(s) cards - Proximity cards.
- [15] G. Doblinger, *MATLAB-Programmierung in der digitalen Signalverarbeitung*. Schlembach, 2001.
- [16] O. A. Alkishriwo, A. Akan, and L. F. Chaparro, “Intrinsic Mode Chirp Decomposition of Non-stationary Signals,” 2014.

EIDESSTATTLICHE ERKLÄRUNG

Hiermit erkläre ich, dass die vorliegende Arbeit gemäß dem Code of Conduct - Regeln zur Sicherung guter wissenschaftlicher Praxis (in der aktuellen Fassung des jeweiligen Mitteilungsblattes der TU Wien), insbesondere ohne unzulässige Hilfe Dritter und ohne Benutzung anderer als der angegebenen Hilfsmittel, angefertigt wurde. Die aus anderen Quellen direkt oder indirekt übernommenen Daten und Konzepte sind unter Angabe der Quelle gekennzeichnet.

Die Arbeit wurde bisher weder im In- noch im Ausland in gleicher oder in ähnlicher Form in anderen Prüfungsverfahren vorgelegt.

Mladen Pesic

Wien, am

.....

(Unterschrift)